

# Advanced measurement procedures and data processing for grating-based X-ray phase-contrast computed tomography

Mathias Marschner-Reh

Vollständiger Abdruck der von der TUM School of Natural Sciences der Technischen  
Universität München zur Erlangung eines  
Doktors der Naturwissenschaften (Dr. rer. nat.)  
genehmigten Dissertation.

Vorsitz: Prof. Dr. David Egger

Prüfende der Dissertation:

1. Prof. Dr. Franz Pfeiffer
2. Prof. Dr. Julia Herzen

Die Dissertation wurde am 22.10.2024 bei der Technischen Universität München eingereicht  
und durch die TUM School of Natural Sciences am 31.01.2025 angenommen.



# Abstract

X-ray phase-contrast and dark-field tomography are promising biomedical imaging techniques. Compared to conventional computed tomography (CT), which relies on X-ray absorption, these methods offer enhanced contrast in materials with low atomic numbers, such as biological soft tissue. Talbot-Lau interferometry, or grating interferometry, is a technique that enables the measurement of phase-contrast and dark-field signals even with conventional X-ray sources. This method employs three gratings with micrometer-sized structures to sample intensity curves that contain phase-contrast and dark-field information. The three-dimensional composition of the examined object can be reconstructed from the calculated projections at various viewing angles.

Recent studies have highlighted the potential of these methods for high-sensitivity imaging in biomedical research. However, the measurement times and radiation doses are still too high for clinical or industrial applications and need to be reduced. This work addresses these challenges and develops potential solutions in the form of novel measurement methods and algorithms.

One outcome of this thesis is the adaptation of helical CT, widely used in clinical and industrial imaging, for application in grating interferometry. The previously necessary movement of the gratings is replaced by a spiral motion of the object during the measurement, that is tailored to the measurement setup. This allows the phase-stepping curve, required for obtaining phase-contrast and dark-field signals, to be sampled without moving the gratings, enabling faster measurements and the measurement of larger objects. In conjunction with a data processing algorithm specifically developed for this measurement technique, the experimental feasibility of helical phase-contrast CT was demonstrated.

The remaining parts of this thesis address the challenge that the conventional measurement and analysis method, while providing a very accurate signal at long exposure times, is not suitable for short exposure times due to its statistical behavior. As a result, a lower dose limit for X-ray phase-contrast CT is often assumed.

In light of this, an alternative measurement and analysis method for phase-contrast imaging and an analogous method for dark-field imaging, that was developed in the context of this work, were investigated with regard to their properties at short exposure times. Simulations and experiments demonstrated that these methods can deliver quantitatively correct results and, in contrast to the conventional method, enable meaningful reconstructions even with very short exposure times.

To fully exploit the advantages of the method in terms of short exposure times and fast measurements without grating movement, the experimental setup must meet cer-

tain requirements. As this is often not the case, a special data processing algorithm was combined with iterative reconstruction algorithms to enable successful image reconstruction even in these cases, which also allows for a more flexible design of the measurement procedure.

The results of this thesis demonstrate that significant improvements in terms of measurement times and radiation dose are possible through alternative measurement and analysis methods. The results contribute to the development of a measurement device optimized for fast measurement times and form a basis for the further development of reconstruction methods in X-ray phase-contrast and dark-field tomography.

# Zusammenfassung

Röntgenphasenkontrast- und Röntgendunkelfeldtomographie sind vielversprechende biomedizinische Bildgebungsverfahren. Diese Verfahren bieten im Vergleich zu konventionellem, auf der Absorption von Röntgenstrahlung basierendem Computertomographie (CT), erhöhten Kontrast in Material mit niedrigen Kernladungszahlen, aus dem u.a. biologisches Weichgewebe besteht. Eine Methode, den Phasenkontrast- und Dunkelfeldkontrast auch mit konventionellen Röntgenquellen zu messen, ist die Talbot-Lau- oder Gitterinterferometrie. Dabei werden drei Gitter mit Strukturen im Mikrometerbereich verwendet, um Intensitätskurven abzutasten, die die Phasenkontrast- und Dunkelfeldinformationen enthalten. Aus den daraus berechneten Projektionen der verschiedenen Blickwinkel kann die dreidimensionale Zusammensetzung des untersuchten Objekts rekonstruiert werden.

Jüngste Studien zeigen das Potential dieser Methoden für hochsensitive Bildgebung in der biomedizinischen Forschung. Für die Nutzung im klinischen oder industriellen Kontext sind die Messzeiten und die deponierte Strahlendosis allerdings noch deutlich zu hoch und müssen reduziert werden. In der vorliegenden Arbeit wurden diese Herausforderungen adressiert und potentielle Lösungen in der Form von neuartigen Messmethoden und Algorithmen entwickelt.

Ein Ergebnis dieser Arbeit ist die Weiterentwicklung der in der klinischen und industriellen Bildgebung weit verbreiteten spiralen CT für den Einsatz in der Gitterinterferometrie. Dabei wurde die bisher notwendige Bewegung der Gitter durch eine mit dem Messaufbau abgestimmte spirale Bewegung des Objekts während der Messung ersetzt. Dadurch kann die für die Gewinnung der Phasenkontrast- und Dunkelfeldsignale notwendige Phasenkurve abgetastet werden, ohne die Gitter bewegen zu müssen, was schnellere Messungen und gleichzeitig die Messung größerer Objekte ermöglicht. In Verbindung mit einer eigens für diese Messmethode entwickelten Auswertemethodik konnte die experimentelle Umsetzbarkeit der spiralen Phasenkontrast-CT gezeigt werden.

Die weiteren Teile dieser Arbeit widmen sich der Herausforderung, dass die konventionelle Mess- und Analysemethode zwar ein sehr genaues Signal bei langen Belichtungszeiten liefert, aber aufgrund ihres statistischen Verhaltens nicht für kurze Belichtungszeiten geeignet ist und deshalb ein unteres Dosislimit für Röntgenphasenkontrast-CT angenommen wird.

Vor diesem Hintergrund wurde eine alternative Mess- und Analysemethode für die Phasenkontrastbildgebung und eine dazu analoge, im Rahmen dieser Arbeit entwickelte Methode für die Dunkelfeldbildgebung in Hinblick auf ihre Eigenschaften bei kurzen

Belichtungszeiten untersucht. Dabei wurde in Simulationen und experimentell nachgewiesen, dass diese Methoden quantitativ korrekte Ergebnisse liefern können und es – im Gegensatz zu der konventionellen Methode – selbst bei sehr kurzen Belichtungszeiten noch möglich ist, aussagekräftige Rekonstruktionen zu erzielen.

Um alle Vorteile der Methode in Bezug auf kurze Belichtungszeiten und schnelle Messungen ohne Gitterbewegung nutzen zu können, muss der Messaufbau bestimmte Voraussetzungen erfüllen. Da dies regelmäßig nicht der Fall ist, wurde eine spezielle Auswertemethodik mit iterativen Rekonstruktionsalgorithmen kombiniert, um auch in diesen Fällen eine erfolgreiche Bildrekonstruktion zu ermöglichen, was auch eine flexiblere Gestaltung der Messprozedur ermöglicht.

Die Ergebnisse dieser Arbeit zeigen auf, dass durch alternative Mess- und Analysemethoden signifikante Verbesserungen in Bezug auf Messzeiten und deponierte Strahlendosis möglich sind. Die Ergebnisse können in die Entwicklung eines auf schnelle Messzeiten optimierten Messgeräts einfließen und bilden eine Basis für die Weiterentwicklung der Rekonstruktionsmethoden in der Röntgenphasenkontrast- und Röntgendunkelfeldtomographie.

# Contents

<b>1</b>	<b>Introduction</b>	<b>1</b>
<b>2</b>	<b>Theoretical Background</b>	<b>5</b>
2.1	Interactions of X-rays with matter . . . . .	5
2.1.1	Complex refractive index . . . . .	6
2.1.2	Attenuation and the Lambert-Beer law . . . . .	8
2.1.3	Phase shift and Snell's law . . . . .	9
2.2	Grating-based imaging . . . . .	10
2.2.1	The Talbot effect . . . . .	10
2.2.2	Grating interferometry . . . . .	13
2.2.3	Phase stepping . . . . .	14
2.2.4	Talbot-Lau interferometry . . . . .	19
2.3	Statistical properties in grating interferometry . . . . .	21
2.3.1	Attenuation contrast signal . . . . .	22
2.3.2	Phase-contrast signal . . . . .	23
2.3.3	Dark-field signal . . . . .	27
2.4	Tomographic imaging . . . . .	29
2.4.1	Filtered backprojection . . . . .	29
2.4.2	Statistical iterative reconstruction . . . . .	33
<b>3</b>	<b>Experimental Setup &amp; Data Processing</b>	<b>37</b>
3.1	Phase-contrast computed tomography setup . . . . .	37
3.2	Data processing for phase-contrast computed tomography . . . . .	40
3.2.1	Pre-Processing . . . . .	40
3.2.2	Signal Extraction . . . . .	40
3.2.3	Post-Processing . . . . .	45
<b>4</b>	<b>Helical X-ray phase-contrast computed tomography without phase-stepping</b>	<b>49</b>
4.1	Introduction . . . . .	49
4.2	Methods . . . . .	51
4.2.1	Grating alignment in a fringe scanning setup . . . . .	51
4.2.2	Helical fringe-scanning phase-contrast computed tomography . . . . .	52
4.2.3	Experimental setup and sample . . . . .	55
4.3	Results . . . . .	55
4.4	Discussion . . . . .	59

<b>5</b>	<b>Two-shot phase contrast imaging</b>	<b>63</b>
5.1	Introduction . . . . .	63
5.2	Two-shot phase retrieval . . . . .	64
5.2.1	Reverse projection method . . . . .	64
5.2.2	Statistical properties . . . . .	68
5.2.3	Limitations and adaptations . . . . .	69
5.3	Experimental results . . . . .	72
5.3.1	Samples and measurements . . . . .	72
5.3.2	Quantitative accuracy . . . . .	73
5.3.3	Statistical properties . . . . .	76
5.3.4	Comparison to phase stepping . . . . .	81
5.3.5	Tomography using projection weights . . . . .	84
5.4	Discussion . . . . .	88
5.5	Conclusion . . . . .	90
<b>6</b>	<b>Two-shot X-ray dark-field imaging</b>	<b>91</b>
6.1	Introduction . . . . .	91
6.2	Two-shot dark-field imaging . . . . .	91
6.3	Experimental results . . . . .	94
6.3.1	Radiography of a scattering sample . . . . .	94
6.3.2	Radiography of a strongly absorbing, non-scattering sample . . . . .	96
6.3.3	Tomographic two-shot dark-field imaging . . . . .	99
6.3.4	Dose-optimized tomography using projection weights . . . . .	102
6.4	Conclusion . . . . .	105
<b>7</b>	<b>Summary &amp; Outlook</b>	<b>107</b>
	<b>Bibliography</b>	<b>109</b>
	<b>List of publications and scientific presentations</b>	<b>127</b>
	<b>Acknowledgments</b>	<b>133</b>

# CHAPTER 1

## Introduction

Since the discovery of X-rays by Wilhelm Conrad Röntgen in 1895 (Röntgen, 1896), X-ray imaging has undergone rapid development. Over the course of the last decades, it has become an integral part of clinical diagnostics and industrial non-destructive testing applications. It has been especially the case since the digitization of X-ray detectors, which improved the achievable image quality significantly. This innovation also enabled the development of a new imaging technique that reveals the three-dimensional internal structure of objects: X-ray computed tomography.

One of the major limitations of X-ray computed tomography (CT) in the clinical context and of X-ray imaging in general is limited soft-tissue contrast. One way to address this shortcoming is to employ phase-sensitive imaging methods, which access the real part of the refractive index of the measured object (Bonse and Hart, 1965; David et al., 2002). The refractive index decrement leads to a phase shift of X-rays when passing through an object. The cross-section of this interaction is orders of magnitude higher in comparison to the cross-section of the attenuation interaction (Momose, 2005). Thus, when this information can be accessed for imaging, increased contrast is reached.

While several phase-sensitive imaging techniques exist, only some yield favorable preconditions for a laboratory implementation (Momose, 2003; Weitkamp et al., 2005; Momose, 2005; Pfeiffer et al., 2006b,c; Olivo and Speller, 2007; Pfeiffer et al., 2007a, 2008b). One promising technique for tomographic imaging with laboratory sources is called X-ray grating interferometry (Momose, 2003; Pfeiffer et al., 2006b). In this approach, X-ray gratings are used to encode phase information in sinusoidal intensity variations of a series of multiple image frames. The phase information can be retrieved by retrospective analysis of these so-called phase-stepping curves. One advantage of this method lies in the fact that it can be extended – in the same way as attenuation-based X-ray imaging has been – to three-dimensional imaging, i.e., phase-contrast computed tomography (PCCT). Additionally, a third imaging modality, the so-called dark-field image can be calculated from the recorded images (Pfeiffer et al., 2005, 2008a). The dark-field signal contains the small-angle scattering information and thus enables the detection of features below the resolution limit of the imaging system (Yashiro et al., 2010; Lynch et al., 2011).

Several studies employing grating interferometry have been published, which highlight this new method's potential diagnostic benefits compared to attenuation-based X-ray imaging (Bravin et al., 2013; Pfeiffer et al., 2013; Birnbacher et al., 2021). Moreover, the first radiographic and tomographic studies on living animals were conducted (Bech et al., 2013; Velroyen et al., 2015; Hellbach et al., 2015; Gromann et al., 2017; Scherer et al., 2017). Additionally, this method has received increasing interest from manufacturers of medical imaging products (Roessl et al., 2014; Koehler et al., 2015). Lately, first in-vivo studies showing the diagnostic potential of dark-field radiography in humans were published (Willer et al., 2021; Gassert et al., 2021, 2022a; Gassert and Pfeiffer, 2022; Gassert et al., 2022b; Frank et al., 2022; Urban et al., 2022; Zimmermann et al., 2022) and a commercial medical CT scanner was outfitted with gratings to enable darkfield CT (Viermetz et al., 2022). There are also potential applications of X-ray (Jensen et al., 2010b; Revol et al., 2011a; Malecki et al., 2014) and neutron dark-field imaging (Pfeiffer et al., 2006a; Strobl et al., 2008; Hilger et al., 2010; Grünzweig et al., 2008b,a, 2013) in the field of material science.

There are however remaining difficulties which prohibit the use of PCCT in clinical and online industrial settings at this point. Among these, the reduction of scan time and a lower exposure to ionizing radiation are especially important. These challenges are effects of the established measurement and signal analysis procedures.

The measurement procedure that is currently used in X-ray phase-contrast imaging is the so-called phase-stepping procedure. As the name implies, one of the X-ray gratings is moved, or stepped, during the acquisition process. This is a time-consuming mechanical movement which limits measurement speed and ultimately the reduction of scan times.

The second challenge pertains to the signal analysis part of the phase-stepping procedure. It was discovered that there is a minimum exposure time, i.e., dose level, necessary per projection for extraction of a meaningful phase-contrast and dark-field signal (Raupach and Flohr, 2011). At low dose-levels, a phenomenon called statistical phase-wrapping occurs, which inhibits substantial dose-reduction efforts.

This work aims to address these two challenges by developing and investigating a new measurement as well as new signal analysis procedures. It contributes to the development of processing and reconstruction challenges in phase-contrast and dark-field computed tomography and is not only a basis for high sensitivity phase-contrast computed tomography for preclinical research (Birnbacher et al., 2016) but also for bringing X-ray dark-field and phase-contrast computed tomography closer to clinical application (Teuffenbach et al., 2017; Viermetz et al., 2022).

The thesis is split into seven chapters. After a short introduction in chapter 1, the

theoretical foundations of X-ray imaging, phase-contrast imaging and computed tomography are described in chapter 2. The experimental setup and the data processing algorithms are laid out in chapter 3.

The first of the aforementioned challenges is discussed in chapter 4, where a new measurement procedure is presented. An approach developed for two-dimensional phase-contrast imaging is extended to the tomographic case. It is based on the fact that the phase-stepping movement of the gratings can be replaced by a particular movement of the sample. Thus, the problematic phase-stepping procedure is no longer needed, yielding more favourable preconditions for a clinical application.

The second major challenge, the phenomenon of statistical phase-wrapping, is discussed in chapters 5 and 6, focusing on the phase-contrast and the dark-field signal, respectively.

In the first part of chapter 5, we demonstrate the detrimental effects of statistical phase-wrapping in low-dose scans with the phase-stepping procedure. Then, we discuss an alternative measurement and signal analysis procedure, which is not susceptible to statistical phase wrapping, and show the first laboratory-based tomographic scan using this method. In addition, we introduce an adapted iterative reconstruction method that can be used to mitigate shortcomings of the method and of the experimental setup.

Similar to chapter 5, chapter 6 describes a way to dose-effectively record tomographic dark-field scans. First, we demonstrate the inability of the conventional phase-stepping algorithm to accurately retrieve the dark-field signal if photon counts are low. Then, we develop a novel acquisition and data analysis scheme for dark-field imaging, which handles better low photon counts. We experimentally demonstrate that this approach is well suited for tomographic imaging and show reconstructed scans from a laboratory setup.

In chapter 7 we summarize the major results of this thesis and highlight possible future research topics.



# CHAPTER 2

## Theoretical Background

In this chapter, the theoretical foundations of X-ray phase-contrast and dark-field imaging are discussed. The first part addresses the interactions of X-rays with matter and the resulting attenuation and phase-shift of the X-rays. The second part explains the principles of grating-based imaging. In the third and final part, the theoretical underpinnings of tomographic imaging are reviewed shortly. This chapter is based on Kak and Slaney (2001), Buzug (2008), Als-Nielsen and McMorrow (2011) and Willmott (2011).

### 2.1 Interactions of X-rays with matter

X-rays are widely used for imaging purposes due to the fact that they are able to penetrate matter. Thus, they allow a look inside objects that is not possible e.g. with visible light. X-rays used for imaging are electromagnetic waves with wavelengths of ca.  $\lambda = 5 \text{ pm}$  to  $5 \text{ nm}$ . These roughly correspond to energies of  $E = 200 \text{ eV}$  to  $200 \text{ keV}$ .

While passing through matter, X-rays interact with the atoms, in particular its electrons. The dominant interaction processes, at least in the diagnostic imaging range below  $200 \text{ keV}$ , include photoelectric absorption, elastic and inelastic scattering. Its effects are described in the total scattering cross section

$$\sigma_{\text{tot}}(E, Z) = \sigma_{\text{ph}}(E, Z) + \sigma_{\text{incoh}}(E, Z) + \sigma_{\text{coh}}(E, Z), \quad (2.1)$$

where  $\sigma_{\text{ph}}$ ,  $\sigma_{\text{coh}}$ ,  $\sigma_{\text{incoh}}$  describe the cross sections of photoelectric absorption, coherent and incoherent interactions,  $Z$  is the atomic number and  $E$  denotes the photon energy.

In photoelectric absorption, the X-rays interact with a bound electron of the atom, typically from the K or L shell. During this process, there is a complete energy transfer from the X-ray photon to the electron and the electron is ejected from the atom. The cross section of photoelectric absorption roughly scales with

$$\sigma_{\text{ph}}(E, Z) \propto \frac{Z^4}{E^3}. \quad (2.2)$$

X-rays can also be scattered when passing through matter. In inelastic scattering processes the energy and the direction of the photon changes with the interaction.

This scattering process, which is also called Compton scattering, is usually described in particle formalism: the photon hits a loosely bound electron and a part of its energy is transferred to the electron. The scattering cross section for Compton scattering scales with the atomic number

$$\sigma_{\text{incoh}}(E, Z) \propto Z\sigma_{\text{kn}}(E), \quad (2.3)$$

where  $\sigma_{\text{kn}}$  is Klein-Nishina cross section (Klein and Nishina, 1929), which is only weakly proportional to the X-ray energy

$$\sigma_{\text{kn}}(E) \propto E^{-0.2}. \quad (2.4)$$

Elastic scattering means that the photon energy remains unchanged. This process can be illustrated by the photon accelerating an electron, which in turn emits another photon with the same energy but in a different direction.

Fig. 2.1 displays the cross sections of photoelectric absorption, elastic and inelastic scattering for water and calcium for varying energies. In diagnostic imaging with energy ranges between 20 keV to 200 keV, the effect of elastic scattering to the total scattering cross section can be neglected. However, these elastic scattering processes are the main interaction processes that are used for phase-contrast imaging. Imaging methods that are based on absorption contrast rely on the inelastic processes of photoelectric absorption and Compton scattering.

At low X-ray energies photoelectric absorption is the dominant absorption process. Compton scattering is the main interaction process at higher X-ray energies. The cross over point between the two cross sections is dependent on the atomic number. That entails that phase-contrast and absorption contrast is complementary at low energies due to the different dependencies on the atomic number  $Z$  of the two interaction processes.

At higher energies,  $\sigma_{\text{coh}}$  and  $\sigma_{\text{incoh}}$  depend linearly on the atomic number. Therefore, phase-contrast and absorption contrast are not complementary at higher energies.

### 2.1.1 Complex refractive index

The complex index of refraction is commonly used to describe the quantitative effects of these interaction processes. The real part of the refractive index is called the refractive index decrement  $\delta$ . For X-rays it is very small ( $\delta \ll 1$ ). Thus, the complex index of

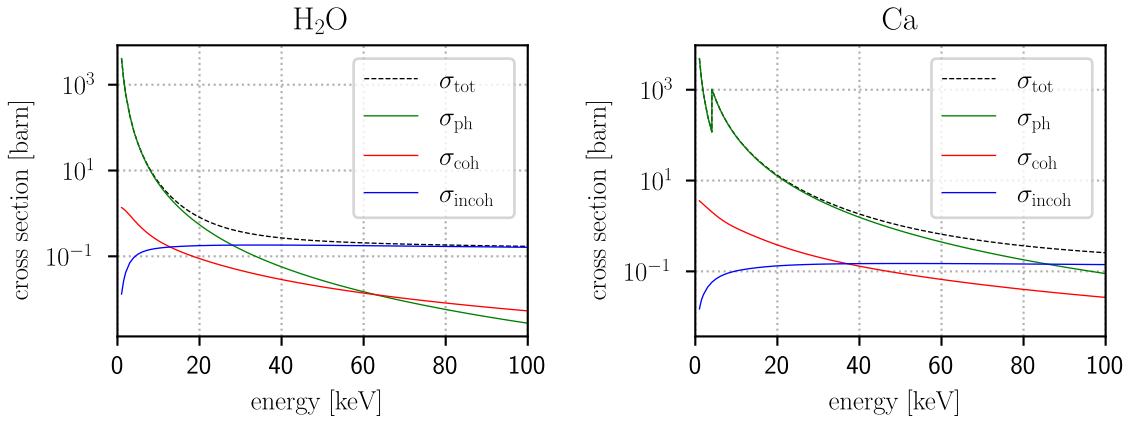


**Fig. 2.1 | Cross section of the different interaction processes.** The cross section of the interaction processes photoelectric absorption, elastic and inelastic scattering depend on the energy and the material. Data obtained from XOP (Berger et al., 2010).

refraction is typically written as

$$n = \underbrace{1 - \delta}_{\text{elastic}} + \underbrace{i\beta}_{\text{inelastic}}, \quad (2.5)$$

where  $\beta$  is the imaginary part of the refractive index. It describes the effects of the inelastic interactions. Elastic interactions between the X-rays and the medium are summarized in the real part of the refractive index  $\delta$ .

An electromagnetic plane wave  $\Psi_v$  propagating in z-direction in vacuum, i.e.,  $n = 1$ , can be expressed by

$$\Psi_v(\vec{r}, t) = \Psi_0 e^{i(\vec{k}\vec{r} - \omega t)} = \Psi_0 e^{i(kz - \omega t)}, \quad (2.6)$$

with the wave-amplitude  $\Psi_0$ , the angular frequency  $\omega$ , the wave-vector  $\vec{k} = (0, 0, k = \frac{2\pi}{\lambda})$ , and the wavelength  $\lambda$ . When passing through a medium with complex refractive index  $n$ , the wavefront is modified. Then, the complex wave number  $k$  becomes  $kn$  as is shown in Fig. 2.2.

The modified wave can now be expressed by

$$\Psi_m(z, t) = \Psi_0 e^{i(nkz - \omega t)} = \Psi_0 e^{-i\omega t} e^{(1-\delta)ikz} e^{-\beta kz} = \Psi_v(z, t) \cdot \underbrace{e^{-i\delta kz}}_{\text{phase-shift}} \cdot \underbrace{e^{-\beta kz}}_{\text{attenuation}}, \quad (2.7)$$

where  $e^{-\beta kz}$  describes the attenuation and  $e^{-i\delta kz}$  describes the phase shift of the incident wave. Consequently, the phase and amplitude of the electromagnetic wave are altered after traversing a medium.

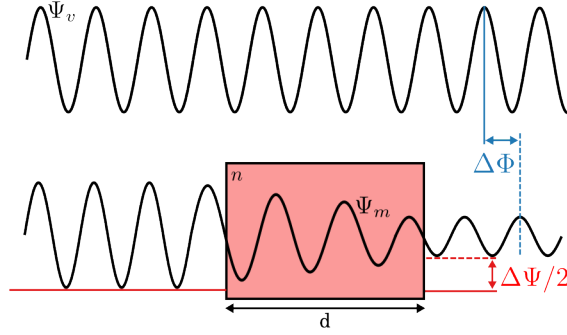


**Fig. 2.2 | X-rays passing through matter.** Schematic showing X-rays, depicted as plane electromagnetic waves, passing through an attenuating and phase-shifting object with a complex index of refraction  $n$ . The amplitude is decreased by  $\Delta\Psi/2$  and the phase is shifted by  $\Delta\Phi$  compared to the unperturbed wave.

### 2.1.2 Attenuation and the Lambert-Beer law

The attenuation of an electromagnetic wave describes the decrease of its intensity  $I$ . The intensity is calculated as the square modulus of the wave-function

$$I(r, t) = |\Psi(z, t)|^2. \quad (2.8)$$

The transmission  $T$  is given by the ratio of intensities before and after traversing a medium with thickness  $d$

$$T(d) = \frac{I_m(d)}{I_v(0)} = \frac{|\Psi_m(d, t)|^2}{|\Psi_v(0, t)|^2} = e^{-2k\beta d}, \quad (2.9)$$

where  $I_v(0)$  and  $I_m(d)$  are the intensities before and after the medium, respectively.

The linear attenuation coefficient  $\mu$  is defined as  $\mu = 2k\beta$ , leading to the Lambert-Beer equation

$$T(d) = \frac{I_m(d)}{I_v(0)} = e^{-\mu d}, \quad (2.10)$$

which is commonly used to describe the attenuation properties of a medium.

For heterogeneous objects and polychromatic X-rays, the Lambert-Beer law is

$$I(z) = \int_{E_{\min}}^{E_{\max}} I_0(E) e^{-\int_0^z \mu(E, Z, z') dz'} dE. \quad (2.11)$$

The total attenuation coefficient for compound materials is a weighted sum of the

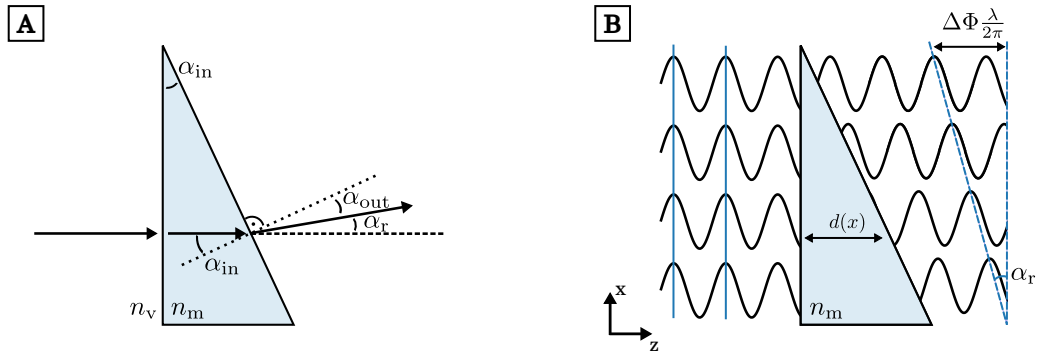


**Fig. 2.3 | Refraction and phase-shift.** There is refraction at the boundary between medium and vacuum if the angle of incidence is different from 0. Snell's law can be used to calculate the angle of refraction (A). Subfigure (B) depicts a plane wave passing through a phase-shifting object with varying thickness in  $x$ -direction, which is perpendicular to the wave. The phase-shifted wave can be viewed as a plane wave with modified propagation direction by an angle  $\alpha_x$ .

constituent elements' attenuation coefficients  $\mu_i$

$$\mu(E) = \sum_i^N w_i \mu_i(E), \quad (2.12)$$

where  $w_i$  is the mass fraction of element  $i$ .

### 2.1.3 Phase shift and Snell's law

A wavefront also experiences a phase shift compared to vacuum when passing through an object. This phase shift is according to Eq. 2.7 equal to

$$\Delta\Phi := \delta k d. \quad (2.13)$$

The phase shift of the electromagnetic wave is strongly related to its refraction. Refraction occurs when X-rays pass through the boundary between two media with different refractive indices. Snell's law states that the angle of incidence  $\alpha_{in}$  and the exit angle  $\alpha_{out}$  are related by

$$n_m \sin(\alpha_{in}) = n_v \sin(\alpha_{out}). \quad (2.14)$$

This effect is schematically depicted in Fig. 2.3A, where a plane wave travels through a phase prism without attenuation ( $\beta = 0$ ). The wave is not refracted at the first boundary since the angle of incidence is 0. The wave is refracted, however, at the second boundary by an angle  $\alpha_r = \alpha_{in} - \alpha_{out}$ .

Another way to look at this effect is to consider the incoming X-rays as a superposition of monochromatic plane waves that are in phase (cf. Fig. 2.3B). As they travel

through the phase prism, they undergo a phase shift that is dependent on the optical path length of the prism that they traverse  $d(x)$ ,

$$\Delta\Phi(x) = k\delta d(x). \quad (2.15)$$

After having traveled through the medium, the phase-shifted wavefront is tilted compared to the incident wavefront. In particular, the peaks of the outgoing waves are aligned on a line that is tilted by an angle  $\alpha_r$  with respect to incident wavefront. Thus, this outgoing wavefront travels in the new, tilted direction. The refraction angle  $\alpha_r$  and the phase shift can be related using geometrical arguments and the small-angle approximation

$$\alpha_r \approx \tan(\alpha_r) = \frac{1}{k} \frac{\partial\Phi(x, y)}{\partial x}. \quad (2.16)$$

The refractive index decrement  $\delta$  ranges from  $10^{-7}$  to  $10^{-5}$  for X-ray energies typically used for imaging (20 – 100 keV). The refraction angles at typical laboratory or medical imaging setups are in the range of nano-radians, which are not easily detectable without using special phase-sensitive methods.

When non-homogeneous three-dimensional objects are imaged, the equations for the transmission and phase shift have to be changed to include the integral along the propagation direction  $z$ . The transmission and phase shift are then given as

$$T(x, y) = e^{-2k \int \mu(x, y, z) dz}, \quad (2.17)$$

and

$$\Delta\Phi(x, y) = k \int \delta(x, y, z) dz, \quad (2.18)$$

respectively. The refraction angle is given in the three-dimensional case by

$$\alpha_x(x, y) = \frac{1}{k} \frac{\partial\Phi(x, y)}{\partial x} = \frac{\partial}{\partial x} \int \delta(x, y, z) dz. \quad (2.19)$$

## 2.2 Grating-based imaging

### 2.2.1 The Talbot effect

The Talbot effect is the essential effect that is exploited in grating-based phase-contrast and dark-field imaging. The self-imaging phenomenon of periodic structures arises from Fresnel diffraction in the near field (Paganin, 2006). It was discovered by Henry Fox Talbot when he placed a grating in visible light and observed an image of the grating in regular distances downstream (H.F. Talbot Esq. F.R.S., 1836). These

distances are called Talbot distances and are given by

$$d_T = \frac{\lambda}{1 - \sqrt{1 - \frac{\lambda^2}{p^2}}} \stackrel{\lambda \ll p}{\approx} \frac{2p^2}{\lambda}. \quad (2.20)$$

The last equality holds true for X-rays, where the wavelength  $\lambda$  is below 1 nm, which is much smaller than the micron-sized grating periods  $p$ , that are typically used for phase-sensitive imaging.

The fractional Talbot effect converts phase modulation to intensity modulation downstream of a phase-shifting grating. Phase-shifting gratings are composed of non-absorbent grating bars that impose a defined phase-shift (Saleh and Teich, 2007; Guigay, 1971). The major advantage of using phase gratings instead of absorption gratings is that no flux is lost due to absorption in the grating bars.

The intensity modulations stemming from the fractional Talbot effect can best be observed at the so-called fractional Talbot distances (Winthrop and Worthington, 1965; Suleski, 1997; Weitkamp et al., 2006). They depend on the Talbot distances and the phase-shift imposed by the grating

$$d_n = \begin{cases} n \frac{p^2}{\lambda} = n d_T & \text{for absorption gratings} \\ n \frac{p^2}{8\lambda} = n \frac{d_T}{16} & \text{for } \pi\text{-shift} \\ n \frac{p^2}{2\lambda} = n \frac{d_T}{4} & \text{for } \frac{\pi}{2}\text{-shift,} \end{cases} \quad (2.21)$$

where  $n = 1, 3, 5, \dots$ .

The spatial distribution of the intensity modulations in dependence on the direction of propagation is shown in Fig. 2.4. Three examples of these commonly called Talbot carpets are displayed, highlighting the difference between absorbing and purely phase-shifting grating with phase shifts of  $\pi$  and  $\frac{\pi}{2}$ . All of those gratings have duty cycles of 0.5, meaning that exactly half of each period is covered by absorbing or phase shifting material, respectively. The first and third fractional Talbot distance are each marked by dashed lines in the figure. Note, that non-binary gratings yield different Talbot carpets (Yaroshenko et al., 2014).

The interference patterns for the two different gratings vary in both the longitudinal (i.e., in direction of propagation) and transversal direction. For  $\pi$ -shifting gratings, the periodicity in longitudinal direction is  $d_T/16$ , one fourth that of gratings imposing phase shifts of  $\pi/2$ . In transversal directions, the periodicity is  $p$  for absorption and for  $\pi/2$ -shifting gratings. For  $\pi$ -shifting gratings the transversal periodicity is  $p/2$ .

The phase shift imposed by the phase grating depends on its material and its thickness as well as on the X-ray energy. This implies that the phase shift is only ever

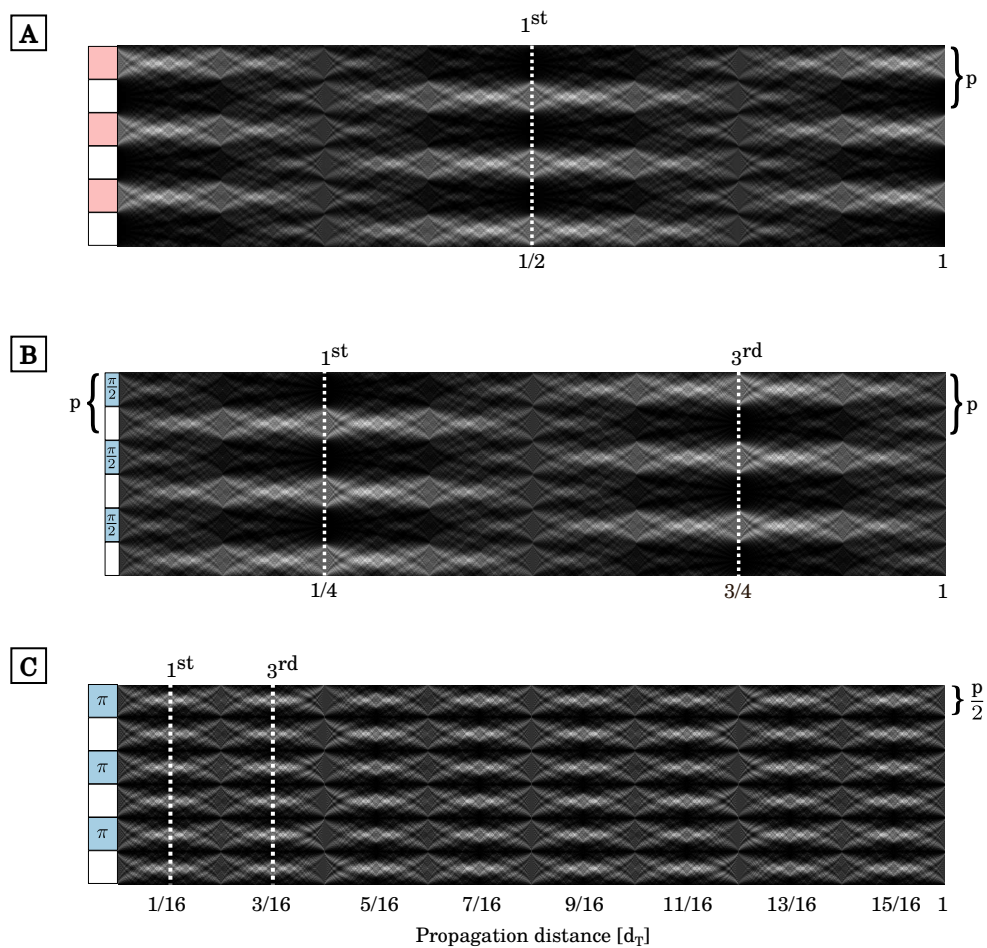


**Fig. 2.4 | Spatially dependent intensity modulations behind absorption and phase-shifting gratings.** Illustration of the simulated intensity modulations behind a phase-shifting grating when it is illuminated with coherent X-rays. The gratings are either perfectly absorbing **(A)** or purely phase-shifting with phase shifts of  $\pi/2$  **(B)** and  $\pi$  **(C)**. The resulting intensity pattern and the positions of maximum intensity variation are commonly called Talbot carpet and fractional Talbot distances, respectively. Note that the transversal periodicity is half of the original period for  $\pi$ -shifting gratings.

exactly  $\pi$  or  $\frac{\pi}{2}$  for one particular X-ray energy. With polychromatic X-ray sources, there is a superposition of Talbot carpets, which diminish the efficiency of a grating-based imaging setup.

### 2.2.2 Grating interferometry

The Talbot effect can be used to achieve phase-sensitive imaging. As shown in 2.1.3, a refracting sample causes an angular deviation  $\alpha_r$  of the propagation direction of the X-rays. In consequence, the interference pattern that results from placing a phase grating in the beam path is shifted laterally by

$$S(x, y) = \alpha_r(x, y)d = \frac{\lambda}{2\pi} \frac{\partial \Phi(x, y)}{\partial x} d, \quad (2.22)$$

where  $d$  is the distance from the phase grating. By measuring the distance that the interference pattern was shifted when the sample was introduced, the differential phase shift induced by the sample is obtained.

This approach works best if the period of the interference pattern is of similar size as the pattern's shift caused by the sample's refraction. A shift larger than a period of the interference pattern leads to phase wrapping, which means that the shift cannot be accurately determined. A refraction of only nano-radians and distances of few meters lead to the fact that the grating needs to have a period of a few microns at maximum.

The interference pattern has similar periods and needs to be recorded with a detector. However, such a high spatial resolution detector is impractical for biomedical applications mainly for two reasons. First, very long exposure times would be required to achieve sufficient photon statistics with laboratory X-ray sources, which would also violate dose constraints in clinical application. Second, detectors featuring the necessary resolution and the size of a human body are prohibitively expensive. Note that high resolution detectors can be used at synchrotron facilities, where the photon flux is orders of magnitude higher and sample sizes are much smaller due to limited beam sizes.

Thus, another solution was found to measure the position of the intensity modulation and thus the differential phase shift of the object: a second grating, which is placed directly in front of the detector (Momose et al., 2003).

This absorbing grating is used to sample or analyze the interference pattern and is thus called analyzer grating. The intensity measured in a detector pixel behind the grating depends on the mismatch between the grating bars and the interference pattern position. Typically, the grating is moved (or stepped) over a full period of the pattern in order to analyze the pattern.

The grating is placed at a fractional Talbot distance  $d_n$ . That way, the changes introduced by the sample to the intensity modulations can be observed.

The effects of a sample in the beam path on the resulting interference pattern is visualized in Fig. 2.5. X-rays traverse the sample and the phase grating, which leads to an intensity pattern downstream. This pattern can then be sampled by the analyzer grating and the intensity recorded in an X-ray detector. The three effects absorption, refraction and small-angle scattering have distinct effects on the interference pattern. While refraction only moves the interference pattern (i.e., changes its phase), absorption and scattering decrease its overall level and amplitude.

### 2.2.3 Phase stepping

Either one of the gratings is stepped over a full period of the interference pattern, i.e., one grating period. During this process several raw detector images are acquired. Thereby, the intensity  $I(x_g, x, y)$  in each detector pixel with location  $x$  and  $y$  is measured at several relative grating positions  $x_g$ . That means, that a phase-stepping curve is recorded for each pixel. Each measured phase-stepping curve is a convolution of the interference pattern with the profile of the gratings and the X-ray source (Bech, 2009). It can be expressed with a Fourier series

$$I(x_g, x, y) = \sum_{n=0}^{\infty} a_n(x, y) \sin\left(2\pi n \frac{x_g}{p_2} + \phi_n(x, y)\right), \quad (2.23)$$

where  $a_n$  and  $\Phi_n$  are the amplitude and phase coefficients while  $x$  and  $y$  are the detector coordinates.

The orders  $n > 2$  can be neglected in cases of limited coherence due to an extended source or a polychromatic spectrum (Bech, 2009), leading to

$$I(x_g, x, y) \approx a_0(x, y) + a_1(x, y) \sin\left(2\pi \frac{x_g}{p_2} + \phi_1(x, y)\right). \quad (2.24)$$

These conditions are usually fulfilled when using conventional X-ray sources.

The figure of merit of an interferometer is the visibility of the interference pattern it generates, i.e., the distance of minimum and maximum intensity. It is related to the ratio of the magnitude  $a_1$  to the mean intensity  $a_0$  in a reference scan, i.e., without sample in the beam,

$$V^r(x, y) \equiv \frac{I_{\max}(x, y) - I_{\min}(x, y)}{I_{\max}(x, y) + I_{\min}(x, y)} = \frac{a_1(x, y)}{a_0(x, y)}. \quad (2.25)$$

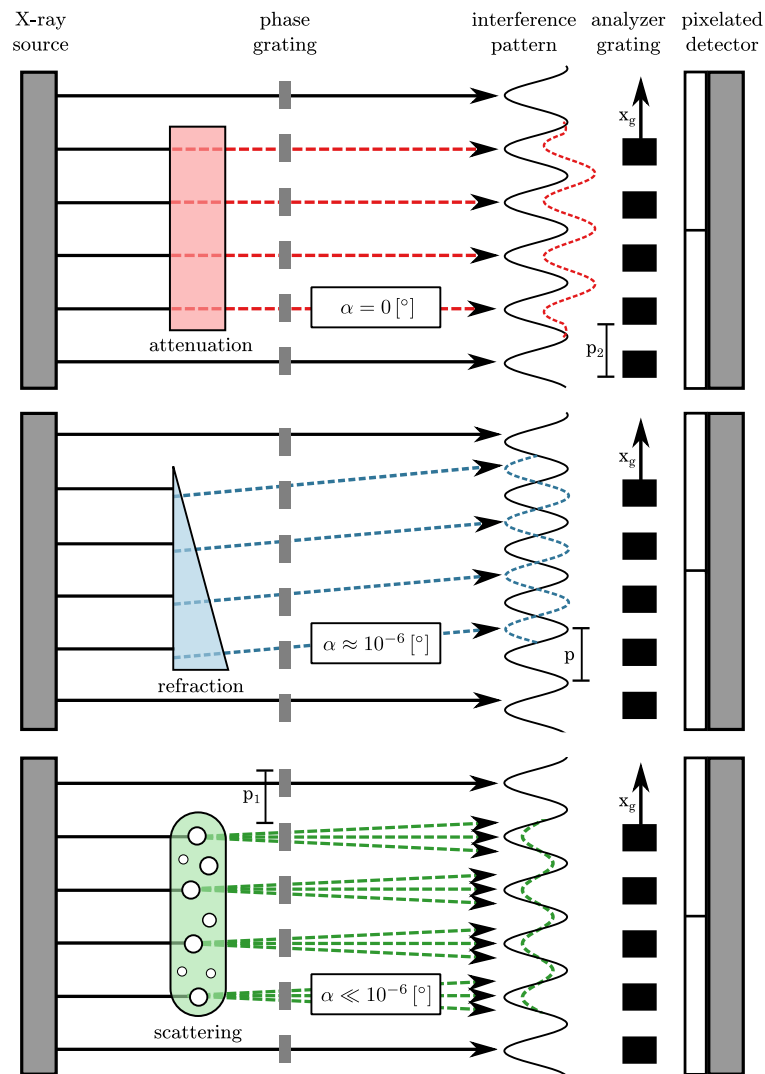


**Fig. 2.5 | Schematic of a grating interferometer.** Plane waves from a X-ray source pass through a phase grating. The Talbot effect causes intensity modulations downstream. The intensity pattern is analyzed by stepping an absorbing grating in direction perpendicular to the grating bars. The period  $p_2$  of the analyzer grating has to match the period  $p$  of the interference pattern, which depends on the phase grating's phase shift and period  $p_1$ . When a sample is introduced in the beam path, three separate effects can occur (from top to bottom): An absorbing sample will decrease the overall intensity of the interference pattern, a refracting sample leads to a shift in the intensity pattern and a scattering sample results in a decrease in the pattern's amplitude. Figure adapted from Scherer (2015).

The three parameters  $a_0$ ,  $a_1$  and  $\phi_1$  of the phase stepping curve are tied to the effects of attenuation, scattering and refraction inside a sample. They relate to the three contrast modalities attenuation, dark-field and differential phase contrast.

At least three data points have to be measured to be able to retrieve the three parameters of the phase stepping curve. The parameters can be extracted using a variety of methods including Fourier analysis and a least-squares fit with a sine function. A more detailed description of the signal extraction process is given in Chapter 3.

The parameters of the phase-stepping curve are extracted for each detector pixel separately. They are also separately extracted for the reference scan, denoted by the superscript  $r$ , and the sample scan, which is denoted by  $s$ . The reference scan is conducted without the sample in the beam path. The phase-stepping procedure and exemplary phase-stepping curves for the three contrast modalities are depicted in chapter 2.6.

**Attenuation contrast** The attenuation by the sample is related to the decrease in the stepping curve's mean intensity as depicted in Fig. 2.6(A). In particular, the attenuation is given by

$$A(x, y) = 1 - T(x, y) = 1 - \frac{a_0^s(x, y)}{a_0^r(x, y)}, \quad (2.26)$$

where  $a_0^{r,s}$  are the zero-order Fourier coefficients, and  $T(x, y)$  is the transmission of the sample. The transmission follows the Lambert-Beer equation (see Eq. 2.10). In case of real world objects the linear attenuation coefficient  $\mu$  varies throughout the object and is thus given by a line integral along the beam path, yielding

$$T(x, y) = \frac{a_0^s(x, y)}{a_0^r(x, y)} = e^{-\int \mu(x, y, z) dz}. \quad (2.27)$$

Often, the negative logarithm is applied to the attenuation contrast before being plotted

$$T'(x, y) = -\log T(x, y) = -\log \frac{a_0^s(x, y)}{a_0^r(x, y)} = \int \mu(x, y, z) dz. \quad (2.28)$$

Thereby, the value of the line integral is visualized directly in each pixel.

**Differential phase contrast** The interference pattern is not measured directly but instead analyzed via the phase-stepping procedure. The difference in relative phase is proportional to the transverse shift of the interference pattern

$$\Delta\phi(x, y) = \phi_1^s(x, y) - \phi_1^r(x, y) = 2\pi \frac{S(x, y)}{p_2}, \quad (2.29)$$

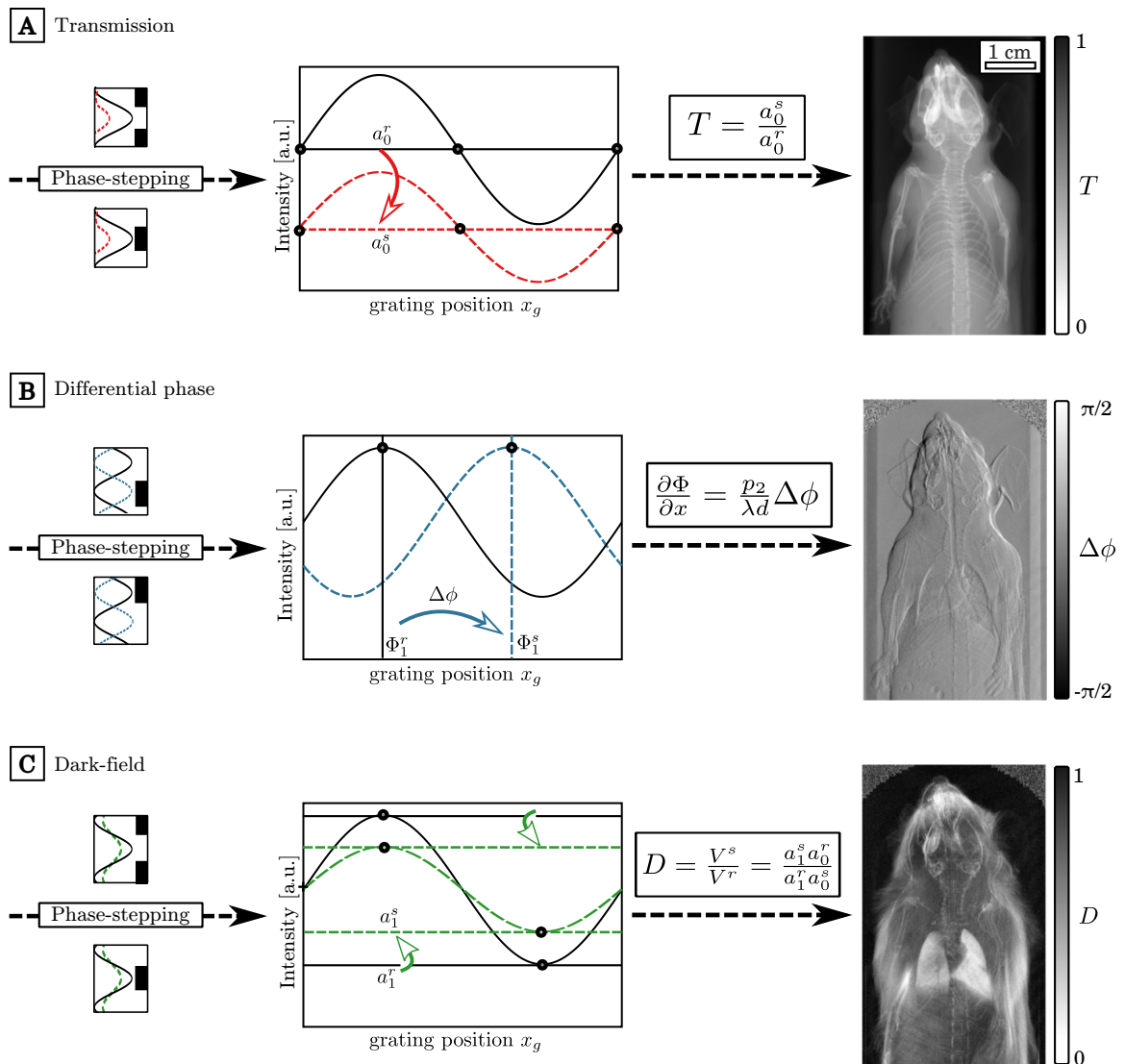


**Fig. 2.6 | Retrieval of the three image signals.** The effects of attenuation, refraction and scattering change the recorded phase-stepping curves in distinctive ways. By comparing the sample curves with the reference curves, the three contrast modalities attenuation, differential phase and dark-field contrast can be extracted. The three resulting images each show different anatomical features of the scanned mouse. In real-world samples these effects are superimposed but can be separated e.g. by Fourier analysis of the stepping curve. Figure adapted from Scherer (2015) and Bech et al. (2013).

as visualized in Fig. 2.6(B).

The differential phase-shift is proportional to the refraction angle (see Subs. 2.1.3). Consequently, the measured displacement of the stepping curve can be related to the differential phase shift of the sample using Eq. 2.22

$$\frac{\partial\Phi(x, y)}{\partial x} = \Delta\phi \frac{p_2}{d\lambda}. \quad (2.30)$$

The differential phase shift is related to the object's refractive index decrement, as shown in Eq. 2.19, resulting in

$$\frac{\partial\Phi(x, y)}{\partial x} = k \frac{\partial}{\partial x} \int \delta(x, y, z) dz = \Delta\phi(x, y) \frac{p_2}{d\lambda}. \quad (2.31)$$

From now on in this thesis the phase-shift's subscript 1 ( $\phi_1 \equiv \phi$ ) and the positional parameters  $x$  and  $y$  will mostly be omitted for clarity.

**Dark-field contrast** The third image signal that can be obtained in grating interferometry is called dark-field signal. It depends on the small angle scattering inside the sample (Pfeiffer et al., 2008b; Yashiro et al., 2010; Jensen et al., 2010a; Lynch et al., 2011; Strobl, 2014). Scattering inside the sample decreases the modulation depth of the measured intensity pattern and thereby its visibility (cf. Subs.2.2.3). An exemplary stepping curve is shown in Fig. 2.6(C). Consequently, the dark-field signal is defined as the ratio of visibility with and without sample

$$D = \frac{V^s}{V^r} = \frac{a_1^s a_0^r}{a_1^r a_0^s} = e^{-\frac{2\pi^2 d^2}{p_2^2} \int \epsilon(x, y, z) dz}, \quad (2.32)$$

where  $\epsilon(x, y, z)$  is the linear diffusion coefficient (Bech, 2009).

The dark-field signal is sensitive to structures smaller than the resolution of the imaging setup. The signal is highly dependent on the size of the structures in the sample and on the interferometer setup, in particular the relative positions of the sample and the analyzer grating (Prade et al., 2015).

Recently, there have been investigations into intra-pixel phase-contrast effects that lead to a dark-field signal which does not arise from small angle scattering and may limit reproducibility across setups (Koenig et al., 2016).

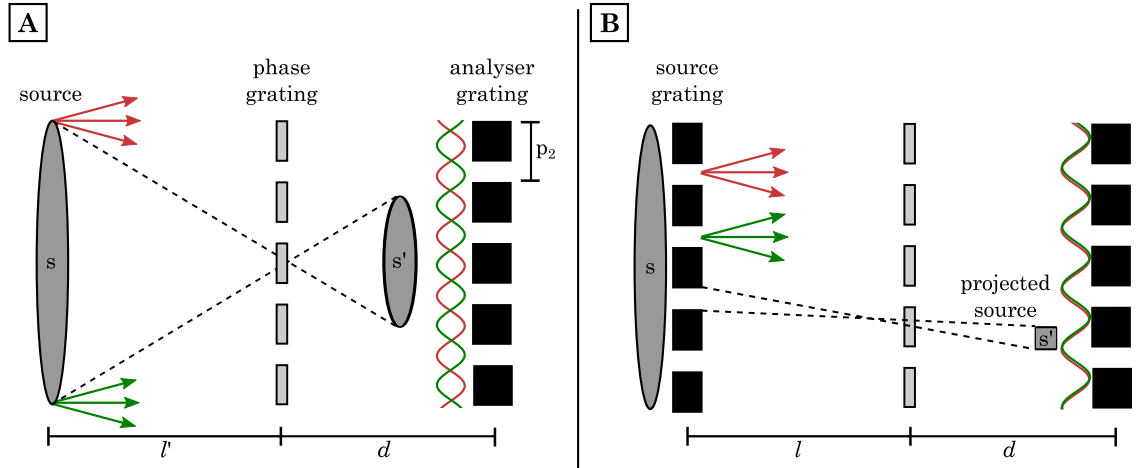


**Fig. 2.7 | Extended sources and the Lau effect.** (A) Extended sources lead to blurring of the interference pattern, since the contributions from the upper and lower end of the source overlap. If the projected source size  $s' = s \frac{d}{l}$  is larger than the period of the interference pattern  $p_2$ , the overlap is so large that the interference pattern is not visible any more. (B) By introducing an absorbing source grating directly behind the source, the projected source size is effectively reduced as each slit acts as a coherent source. If the period of the source grating is chosen correctly, the contributions from all slits contribute constructively to the image-formation process. Figure adapted from Scherer (2015).

## 2.2.4 Talbot-Lau interferometry

### Laboratory X-ray sources

Laboratory X-ray sources feature comparatively large focal spot sizes. This is especially the case for rotating anode tubes, which give high output power. They are therefore preferred for medical and industrial applications, where fast scans are crucial.

Generally, one can imagine the larger source as a sum of separate line sources with distances  $\epsilon$  (Bech, 2009). These line sources create interference patterns that are shifted by  $\epsilon \frac{d}{l}$  with respect to each other. The interference patterns will constructively overlap if  $\epsilon \frac{d}{l} \ll p_2$  and cancel each other out if  $\epsilon \frac{d}{l} = p_2$ , as shown in Fig. 2.7(A). It follows that the source size needs to be smaller than

$$s < \frac{p_2 l}{2d} \quad (2.33)$$

for phase-sensitive imaging (Paganin, 2006; Pfeiffer et al., 2006b). Thus, source sizes roughly equal to the period of the analyzer grating are needed, which are in the order of micrometers.

For larger source sizes, a third grating,  $G_0$ , needs to be used, which is placed directly behind the source. This absorbing grating creates an array of line sources, each one

of which fulfills Eq. (2.33) (Pfeiffer et al., 2006b). The period of this so-called source grating should be

$$p_0 = p_2 \frac{l}{d}, \quad (2.34)$$

so that the interference patterns of the individual line sources overlap constructively as illustrated in Fig. 2.7(B).

This so-called Lau effect enables phase-sensitive imaging with incoherent sources, such as high-power rotating anode X-ray tubes. An interferometer in this three-grating configuration is called Talbot-Lau interferometer.

### Polychromatic sources

In general, X-ray grating interferometry is compatible with polychromatic X-ray sources. However, one has to consider that the phase-grating's phase shift as well as the fractional Talbot distances vary with the X-ray energy. Thus, with a polychromatic spectrum, the phase shift is only exactly e.g.  $\pi$  or  $\pi/2$  for one energy, the so-called design energy (Chabior, 2011) and the position and shape of the interference pattern varies with the X-ray energy. In total, the intensity patterns of each energy overlap and result in a blurred intensity pattern compared to the monochromatic case. In the imaging setup, this will be observed as a reduced overall visibility.

The mean visibility of a polychromatic Talbot-Lau interferometer can be approximated by the integral of the visibilities over all energies, weighted by the energy spectrum. In a  $\pi/2$ -shifting setup, the self-images are shifted in phase by  $\pi$  for certain energies. The shifted pattern can be seen when comparing the first and third fractional Talbot distance in Fig. 2.4(B). These shifted patterns can partly cancel each other out, which lowers the overall visibility. This effect has been termed "negative visibility". It is most predominant in highly sensitive setups as they feature large inter-grating distances and a large fractional Talbot order. Setups with  $\pi$ -shifting gratings give superior visibilities as in this case there are only positive visibilities (Hipp et al., 2014).

One way to mitigate the effect of summing over negative visibilities is to filter the beam to suppress the energies that contribute negative visibilities. Another solution could be the use of energy-resolving detectors (Mechlem et al., 2020).

It is important to consider that only the spectrum that is seen by the detector matters in these calculations. It is influenced by the X-ray tube's anode material and voltage, filtering, both deliberate as well as by the gratings' substrates and materials, the sample and the detector's energy dependent quantum efficiency. All these factors have to be considered when designing an optimized Talbot-Lau interferometer, as its visibility is an important factor regarding image noise and therefore measurement time and radiation dose.

### Cone-beam geometry

Cone-beam geometries are prevalent in X-ray imaging setups that use conventional X-ray sources since the X-ray beam coming from the source is divergent and geometrical magnification has to be considered. In particular, the interference pattern as well as the sample projection are magnified by the factor of

$$M = \frac{d + l}{l}, \quad (2.35)$$

with  $d$  and  $l$  being the inter-grating distances in Fig. 2.7. This magnification effect has the benefit of allowing larger fields of view with compact setup lengths. It also needs to be considered when designing and optimizing a Talbot-Lau interferometer. In particular, the period of the analyzer grating  $p_2^M$  needs to be adapted to the magnified interference pattern, following

$$p_2^M \stackrel{!}{=} M p_t \quad (2.36)$$

Additionally, the fractional Talbot distances (cf. Eq. (2.21)) are changed due to the magnification by

$$d_n^M = M d_n, \quad (2.37)$$

due to the Fresnel scaling theorem (Paganin, 2006).

As discussed in the previous section, the necessary period of the source grating depends on the period of the analyzer grating. Consequently, the period of the source grating needs to be adapted in the magnified case by

$$p_0^M \stackrel{!}{=} p_2^M \frac{l}{d}. \quad (2.38)$$

For large cone angles, shadowing of the outer parts of the gratings – in direction perpendicular to the grating bars – leads to decreased flux and efficiency of the interferometer (Thüring et al., 2011). This problem can be mitigated by the use of bent gratings (Revol et al., 2011b; Sun et al., 2015; Viermetz et al., 2022).

## 2.3 Statistical properties in grating interferometry

The precision of measurement of the X-ray flux in a detector pixel is limited by photon-counting statistics. Thus, the precision of the attenuation, phase-contrast and dark-field measurements is also limited by statistics.

Additional sources of error include positioning jitter, alignment instabilities or flux

fluctuations. The key difference between the mechanical and statistical errors is their dependence on the exposure time. While the uncertainty due to counting statistics falls with increasing exposure time, the mechanical errors are constant or even increase (Revol et al., 2011a; Birnbacher et al., 2016). Thus, mechanical instabilities do not pose a fundamental theoretical limit on exposure time reduction. Nevertheless, a solution for algorithmically mitigating setup instabilities is presented in Section 3.2.2.

As the focus of this work is to offer solutions for shortening measurement times, the influence of photon statistics will now be investigated in detail. The following is valid for photon counting detectors, which were used exclusively in this thesis. Additional corrections have to be applied for non photon counting, i.e., integrating detectors.

The measured intensity in each pixel for a single step of the phase-stepping curve follows Poisson statistics. The probability to detect  $m$  photons is given by

$$P(m, M) = \frac{M^m}{m!} e^{-M}, \quad (2.39)$$

where  $M$  is the expectation value for the number of photons. Exemplary distributions for varying values of the average number of photons  $M$  are shown in Fig. 2.8. For expectation values higher than ten, the Poisson distribution can be approximated well by a Gaussian distribution.

These independent measurements form a phase-stepping scan that results in a phase stepping curve for each pixel. The three image signals are calculated from these phase-stepping curves. Thus, the statistical uncertainty or image noise in the individual stepping images influences the three final images.

### 2.3.1 Attenuation contrast signal

To extract the attenuation signal, the first Fourier coefficient is evaluated. Thus, all stepping images are summed to generate the final attenuation image. Consequently, the statistics in attenuation contrast are identical to conventional radiography if detector readout noise is negligible and the sampling of the stepping curve is equidistant.

One has to consider that the analyzer grating filters out a significant portion of the photons that hit the sample. With a commonly used duty cycle of 0.5, at least half of the photons do not contribute to the final attenuation image. Therefore, the image noise is higher by at least a factor of  $\sqrt{2}$  compared to conventional radiography.

Explicitly, the standard deviation of the attenuation contrast signal is given by

$$\sigma_{a_0} = \sqrt{\frac{a_0}{N}}, \quad (2.40)$$

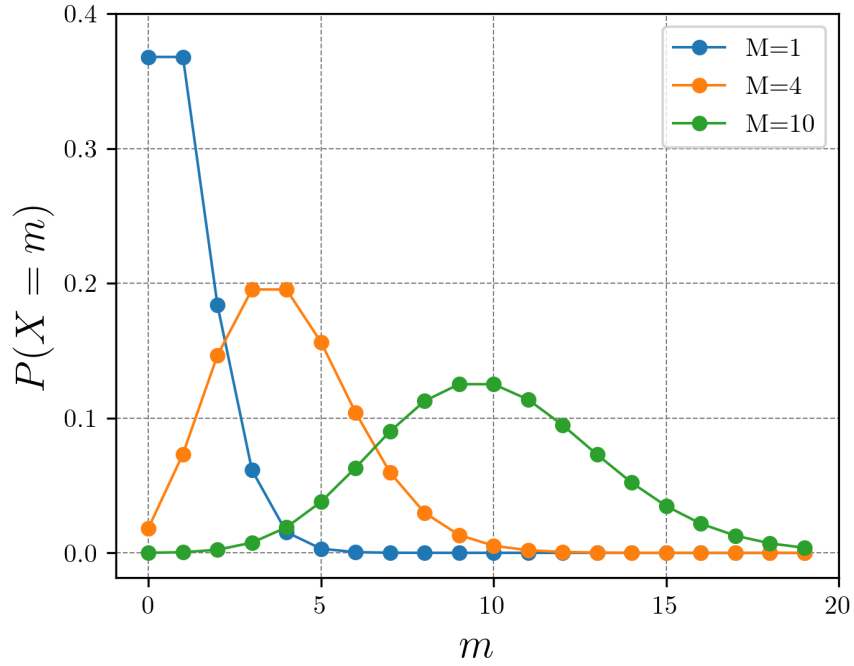


**Fig. 2.8 | Poisson distribution.** Poissonian probability mass functions for exemplary values of the expected number of occurrences (e.g. photon counts). At expected values of around ten, the function starts to resemble a Gaussian probability density function.

where  $N$  is the number of steps. The normalized standard deviation  $\tilde{\sigma}$  signifies the noise level in the images and is calculated as

$$\tilde{\sigma} = \frac{\sigma_{a_0}}{a_0} = \frac{1}{\sqrt{N a_0}} = \frac{1}{\sqrt{I_{\text{tot}}}}, \quad (2.41)$$

with  $I_{\text{tot}}$  being the total number of photons over all phase steps.

In grating-based imaging, reference images are subtracted from or used to divide the measured projections. The reference images can be acquired with high precision since the acquisition does not contribute to the overall exposure of the sample. Therefore, the influence of the reference images on the noise of the final projections is negligible.

### 2.3.2 Phase-contrast signal

To understand the statistical properties of the phase-contrast signal, it is helpful to look at the complex Fourier coefficients of the phase-stepping curve

$$c_k = \frac{1}{N} \sum_{n=0}^{N-1} I_n e^{\frac{2\pi i}{N} n k}, \quad (2.42)$$

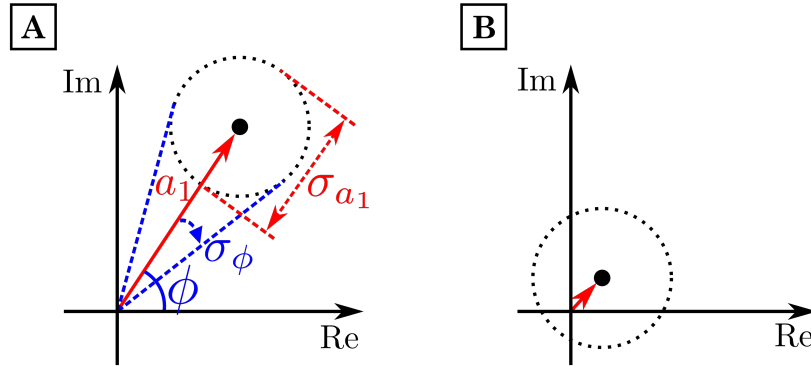


**Fig. 2.9 | Complex Fourier coefficient  $c_1$ .** Schematic showing the distribution of the reconstructed complex Fourier coefficient  $c_1$  in the complex plane. The uncertainty of the reconstruction at a higher noise level is indicated by the dotted circle around  $c_1$ . In (A), the signal-to-noise ratio is high, leading to correctly reconstructed phase-contrast and darkfield signals. In panel (B), however, the signal-to-noise ratio is very low. Thus, the phase-contrast signal is distributed almost evenly and the darkfield signal strongly depends on the noise level. Figure adapted from Chabior (2011).

where  $I_n$  is the measured intensity (cf. Eq. (2.23)). The coefficient  $c_1$  is calculated using the Fourier transform on the phase stepping curve. Assuming Gaussian-distributed noise in the raw data, the noise in the real and imaginary parts of  $c_1$  is also Gaussian-distributed.

Fig. 2.9(A) shows the first complex Fourier coefficient in the presence of noise in the raw data. The noise level in the real and imaginary part is indicated by the dotted circle. This noise level leads to uncertainty in the determination of both the phase and the magnitude of the Fourier coefficient.

The phase contrast signal  $\phi_1^{s/r}$  is calculated by

$$\phi_1 = \arctan \left( \frac{\text{Im}(c_1)}{\text{Re}(c_1)} \right). \quad (2.43)$$

This calculation however is non-linear. In Fig. 2.9(B), the situation for lower signal-to-noise ratios (SNR) is depicted. Note, that the circle around the expected value, which represents the noise level  $\sigma_{c_1}$ , extends to all four quadrants of the complex plane. Therefore, the measured phase can assume any value from  $-\pi$  to  $\pi$ . In other words, the presence of phase wrapping changes the statistical behavior of the phase-contrast signal. The measured values are distributed according to a wrapped normal distribution, as shown in Fig. 2.10.

The effect of statistical phase wrapping manifests mainly when the SNR is low, i.e., for high noise level and/or low visibility. Therefore, the cases of high and low SNR are

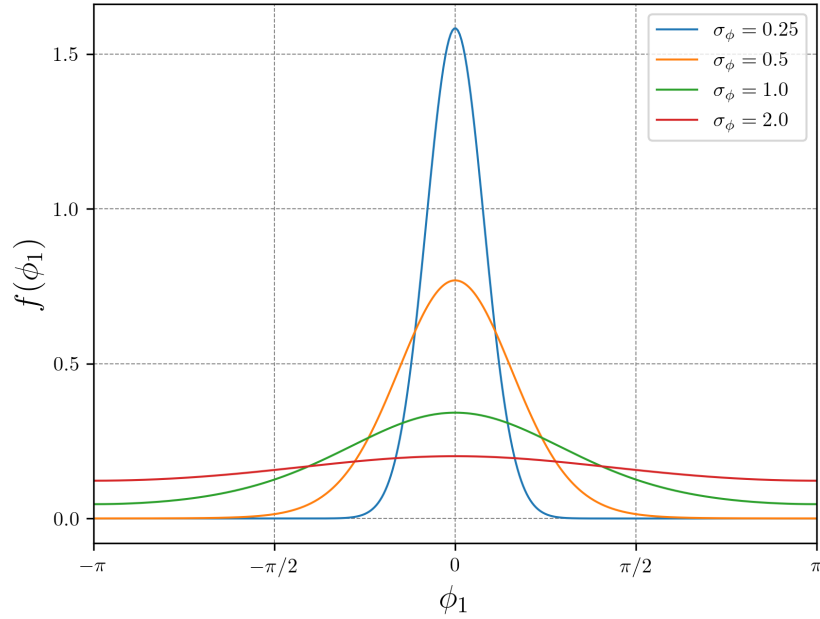


**Fig. 2.10 | Wrapped normal distribution** The measured phase of the phase-stepping curve follows a wrapped normal distribution. In the high-SNR case, the distribution can be approximated by a Gaussian distribution. For lower SNR, the distribution has non-negligible values at the borders, which leads to statistical phase wrapping and a collapse of signal transmission.

considered separately.

## High SNR

In the case of high SNR, i.e., a large number of photons and sufficient visibility, the standard deviation of the retrieved phase in the differential phase-contrast (DPC) projections is proportional to the standard deviation of the measured photon counts in the phase stepping images  $\tilde{\sigma}$ . This standard deviation is itself proportional to the inverse square root of the number of photon counts, assuming the noise is created only by Poisson statistics using a photon-counting detector. Explicitly, the standard deviation in the DPC projections is given by (Chen et al., 2011; Revol et al., 2010)

$$\sigma_\phi = \frac{\sqrt{2}}{V} \tilde{\sigma} = \frac{\sqrt{2}}{V} \frac{1}{\sqrt{Na_0}}. \quad (2.44)$$

Note that this equation assumes that there is no scattering and absorption in the sample, i.e.  $D = 1$  and  $T = 1$ . For samples that exhibit dark-field or absorption

signal, the standard deviation is calculated by

$$\sigma_\phi = \frac{\sqrt{2}}{V} \tilde{\sigma} \frac{1}{\sqrt{TD}}, \quad (2.45)$$

when measuring  $V$  and  $\tilde{\sigma}$  in a sample-free region of the projection.

Absorption in the sample leads to fewer photons hitting the detector which increases the image noise in all three signals: absorption, differential phase and dark-field. Similarly, scattering in the sample leads to a decrease in visibility which in turn increases the noise in the differential-phase and the dark-field signal. In contrast, phase-shifting samples do not lead to an increase in image noise in any of the three signals if the phase stepping is equidistant.

### Low SNR

In the case of low photon counts per pixel, the statistical properties change. Since the measured differential phase is non-ambiguous only in the interval  $I_\phi = ]-\pi, \pi[$ , problems arise when the standard deviation is high and the distribution function of the differential phase  $\phi$  (Fig. 2.10) has non-negligible values at the boundaries of this interval (Chabior, 2011). Then, Gaussian error propagation is no longer valid and some pixels can be affected by statistical phase wrapping (Raupach and Flohr, 2011). This means that the phase wraps around the limits of the interval  $I_\phi$  and a wrong value is measured.

With decreasing number of photons or decreasing visibility, more and more pixels are affected by statistical phase wrapping. This leads to a disproportionate increase of  $\sigma_\phi$ , the standard deviation in the differential phase-contrast projections. In the limit  $\tilde{\sigma} \rightarrow \infty$ , it converges towards  $\sigma_\phi = \pi/\sqrt{3} \approx 1.81$ , which is the standard deviation of the uniform distribution over the interval  $I_\phi$ .

This limit represents the complete collapse of signal transmission for all pixels, which means that the retrieved phase shift contains no useful information anymore.

In conclusion, statistical phase wrapping entails that the phase retrieval does not provide reliable results in affected pixels which corresponds to a collapse of information transmission. Therefore, a lower limit for the number of photons, i.e. the applied radiation dose, exists for successful phase retrieval when using a phase stepping procedure. An alternative method that enables phase retrieval in the low-SNR regime will be presented in Chapter 5.

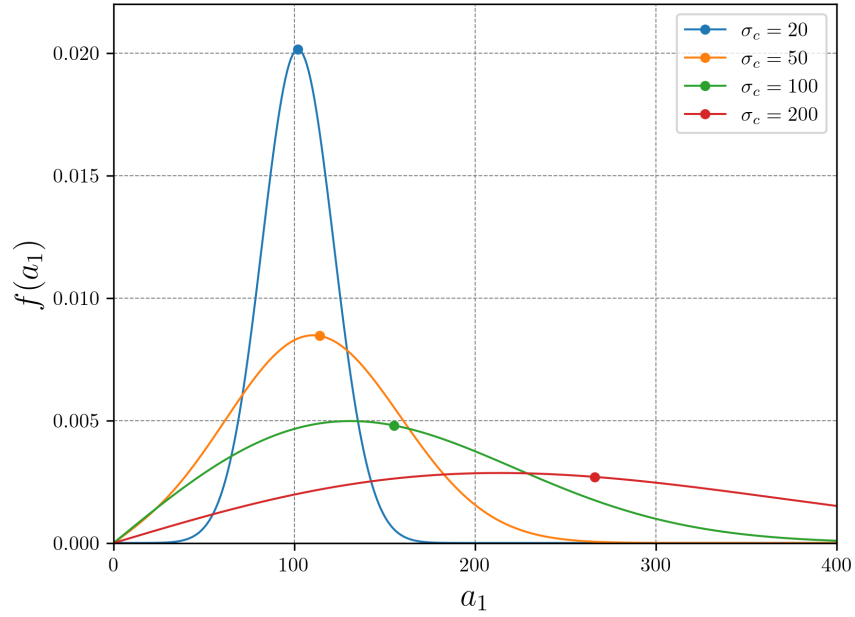


**Fig. 2.11 | Rician distribution.** The measured amplitude of the phase-stepping curve follows a Rician distribution. In the high-SNR case, the distribution can be approximated by a Gaussian distribution. For lower SNR, the distribution becomes skewed towards higher values. Consequently, the distributions' mean values, which are marked by a dot on the curve, rise with growing noise levels.

### 2.3.3 Dark-field signal

The process of calculating the dark-field signal also contains a non-linear step, as it was the case for the phase-contrast signal. In particular, the amplitude of the phase-stepping curve  $a_1$  is calculated from the modulus of the first complex Fourier coefficient  $c_1$  by

$$a_1 = 2|c_1| = 2\sqrt{\text{Re}^2(c_1) + \text{Im}^2(c_1)}. \quad (2.46)$$

The magnitude of a complex number, whose real and imaginary part are Gaussian distributed, follows a Rician distribution (Rice, 1944, 1945; Lindsey, 1964; Sijbers et al., 1999). The Rician distribution for exemplary values of the standard deviation is plotted in Fig. 2.11.

#### High SNR

For low standard deviations compared to the expected value, i.e. in the case of high SNR, the Rician distribution can be approximated by a Gaussian distribution. There,

the standard deviation of the amplitude is (Chabior, 2011)

$$\sigma_{a_1} = \sqrt{2}a_0\tilde{\sigma}. \quad (2.47)$$

Its relative standard deviation is given by

$$\frac{\sigma_{a_1}}{E(a_1)} = \tilde{\sigma} \frac{\sqrt{2}}{V}, \quad (2.48)$$

since the expectation value is  $E(a_1) = a_1$ .

More importantly, the relative standard deviation of the visibility is

$$\frac{\sigma_V}{E(V)} = \tilde{\sigma} \sqrt{\frac{2}{V^2} + 1} \quad (2.49)$$

and its expectation value is

$$E(V) = V. \quad (2.50)$$

As expected, the reconstruction error is proportional to the normalized standard deviation  $\tilde{\sigma}$  and is lower for higher visibility. A detailed derivation of these equations can be found in Chabior (2011).

Usually, the flat-field or reference image visibility and the noise level in a sample free area of the projection are used to estimate the standard deviation or the reconstruction error. In this case, the attenuation and darkfield signal in the sample will increase the reconstruction error by a factor of  $1/\sqrt{T}$  and  $1/\sqrt{TD}$ , respectively.

### Low SNR

In the low-SNR case, the Rician distribution becomes skewed and its expectation value shifts towards higher values, as illustrated in Fig. 2.11. Thus, the estimated visibilities are overestimated, depending on the noise level in the projections. In the low-SNR limit, the Rician distribution is approximated by a Rayleigh distribution (Chabior, 2011). In this case, the expectation value of the measured visibility is  $E(V) = \tilde{\sigma}\sqrt{\pi}$ .

Note that this expectation value is independent of the true visibility  $V$ , which is the quantity that we want to measure, and is instead only a function of the noise level. This effect can also be seen in Fig. 2.9(B), where the magnitude of the complex Fourier coefficient depends mostly on the amount of noise.

The low-SNR and high-SNR cases are extreme cases. In real-world scans, the noise properties lie somewhere between these two extremes. In that case, the estimated visibility is biased (Ji et al., 2017). Going towards lower photon numbers, both the noise and the estimation bias is increasing. There are methods for dark-field bias

correction (De Marco, 2021), which can come at the cost of increased noise.

An alternative solution that allows bias-free reconstruction of the dark-field signal at low SNR will be presented in Chapter 6.

## 2.4 Tomographic imaging

Computed tomography allows to determine the interior structure of an object. Multiple images, called projections, are recorded from different viewing angles around the object and then reconstructed to a three-dimensional volume. It is also applicable to projections obtained with a Talbot-Lau interferometer.

The most commonly used reconstruction method is called filtered backprojection (FBP). It has the benefit of being very fast and easily implemented.

There also are (statistical) iterative reconstruction methods, that offer greater control over the whole reconstruction process and can boost image quality by taking into account prior knowledge and statistical properties of the system. The disadvantage of these methods is their complexity, the tedious choice of suitable prior knowledge and their increased computational cost. However, substantial progress in computational hardware, especially in the area of general purpose graphical processing units, have made their application computationally feasible.

### 2.4.1 Filtered backprojection

A two-dimensional function  $f(x, y)$  can be transformed to its angular projections by the Radon transform. The Radon transform is defined by the line integral

$$P_{\theta}(t) = \int_{(\theta,t)\text{line}} f(x, y) ds , \quad (2.51)$$

where  $\theta$  is the view angle and the line is parameterized as  $t = x \cos(\theta) + y \sin(\theta)$ . This can be rewritten as

$$P_{\theta}(t) = \int_{-\infty}^{\infty} \int_{-\infty}^{\infty} f(x, y) \delta(x \cos \theta + y \sin \theta - t) dx dy , \quad (2.52)$$

using a delta distribution.

The Fourier slice theorem states that the one-dimensional Fourier transform of a projection  $P_{\theta}(t)$  is equal to the tilted slice of the two-dimensional Fourier transform of  $f(x, y)$ , with the slice being tilted at an angle  $\theta$  through the origin (cf. Fig. 2.12).

The two-dimensional Fourier transform of  $f(x, y)$  is given by

$$F(u, v) = \int_{-\infty}^{\infty} \int_{-\infty}^{\infty} f(x, y) e^{-i2\pi(ux+vy)} dx dy . \quad (2.53)$$

The Fourier transform of  $P_{\theta}(t)$  at an angle  $\theta$  is given by

$$S_{\theta}(\omega) = \int_{-\infty}^{\infty} P_{\theta}(t) e^{-i2\pi\omega t} dt , \quad (2.54)$$

where  $(\omega, \theta)$  is the representation of  $(u, v) = (\omega \cos \theta, \omega \sin \theta)$  after transformation to polar coordinates.

The Fourier slice theorem relates the projection  $P_{\theta}(t)$  and object function  $f(x, y)$  by

$$S_{\theta}(\omega) = \int_{-\infty}^{\infty} P_{\theta}(t) e^{-i2\pi\omega t} dt \quad (2.55)$$

$$= \int_{-\infty}^{\infty} [f(t, s) ds] e^{-i2\pi\omega t} dt \quad (2.56)$$

$$= \int_{-\infty}^{\infty} \int_{-\infty}^{\infty} f(x, y) e^{-i2\pi\omega(x \cos \theta + y \sin \theta)} dx dy \quad (2.57)$$

$$= F(u = \omega \cos \theta, v = \omega \sin \theta) \quad (2.58)$$

Thus, we can determine the object function's Fourier transform  $F(u, v)$  on radial lines by taking projections  $P_{\theta}(t)$  of the object at multiple angles  $\theta$  and calculating their Fourier transforms. The object function  $f(x, y)$  can be described by its spectrum  $F(u, v)$  and the inverse two-dimensional Fourier transform can be used to yield the object function

$$f(x, y) = \iint F(u, v) e^{i2\pi(ux+vy)} du dv . \quad (2.59)$$

This inverse Fourier transform is now rewritten in spatial and frequency domain polar coordinates using the substitution  $u = w \cos \theta$  and  $v = w \sin \theta$ , thus  $du dv = \omega d\omega d\theta$ , resulting in

$$f(x, y) = \int_0^{2\pi} \int_0^{\infty} F(\omega, \theta) e^{i2\pi\omega(x \cos \theta + y \sin \theta)} \omega d\omega d\theta . \quad (2.60)$$

Using the property  $F(\omega, \theta + 180^\circ) = F(-\omega, \theta)$  we get

$$f(x, y) = \int_0^{\pi} \left[ \int_{-\infty}^{\infty} F(\omega, \theta) |\omega| e^{i2\pi\omega t} d\omega \right] d\theta , \quad (2.61)$$

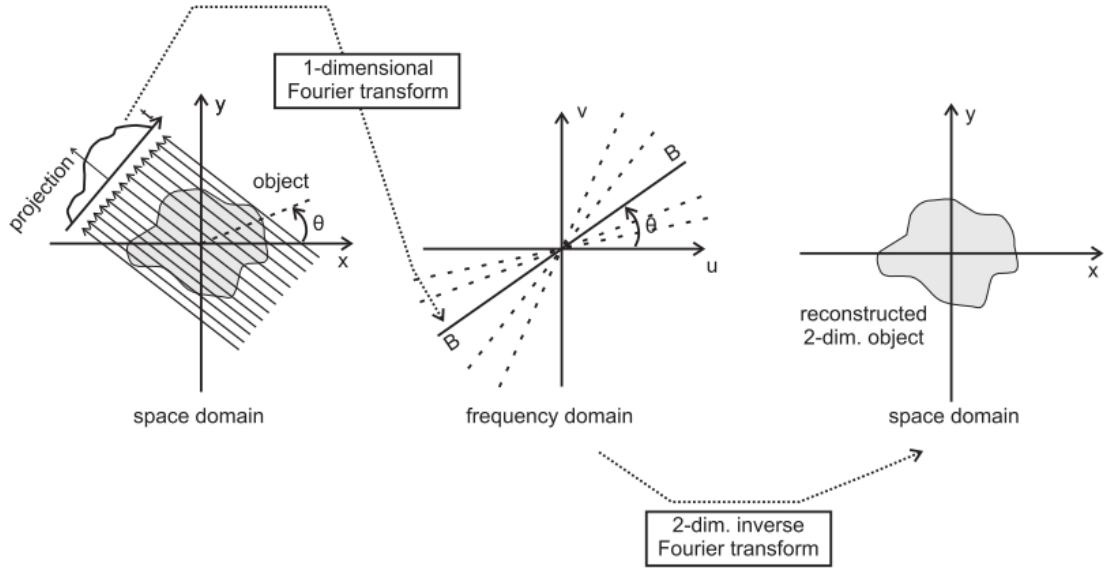


**Fig. 2.12 | Fourier slice theorem and tomographic reconstruction.** The projections data (values of the line integrals through an object at a certain angle  $\theta$ ) is related to a slice in the frequency domain by a one-dimensional Fourier transform. The object can be reconstructed in real space through a two-dimensional Fourier transform of these slices. Figure adapted from Chapter 3.2 of Kak and Slaney (2001).

where  $t = x \cos \theta + y \sin \theta$ . Using the Fourier slice theorem, i.e.

$$f(x, y) = \int_0^\pi \left[ \int_{-\infty}^\infty |\omega| S_\theta(\omega) e^{i2\pi\omega t} d\omega \right] d\theta, \quad (2.62)$$

the double integration can be split up into two parts.

The inner part is an inverse Fourier transform after an application of frequency-dependent weights

$$G(t) = \int_{-\infty}^\infty |\omega| S_\theta(\omega) e^{i2\pi\omega t} d\omega. \quad (2.63)$$

Second, the outer part

$$f(x, y) = \int_0^\pi G(x \cos \theta + y \sin \theta) d\theta, \quad (2.64)$$

which is called backprojection.

In practice, neither  $f$  nor  $S_\theta$  are continuous functions. The integrals then are replaced by discrete sums and the calculations are implemented on a computer using the FFT (Fast Fourier Transform) algorithm.

It follows that  $F(u, v)$  is only known at fixed points along a finite number of radial lines in the frequency space. To represent the values on a Cartesian grid in the reconstruction, interpolation between the coordinate systems is needed, as depicted in

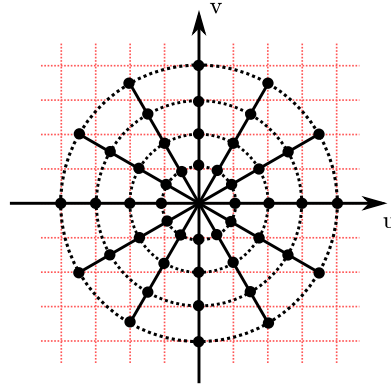


**Fig. 2.13 | Interpolation in Fourier space.** The object function in Fourier space  $F(u, v)$  is only known at fixed points along a finite number of radial lines in frequency space. In order to reconstruct the object in real space, these points have to be interpolated to points on a square grid.

Fig. 2.13.

Evidently, the sampling density in Fourier space is inversely proportional to the frequency, i.e., low frequencies are sampled more densely. In the filtering part of the filtered backprojection, the high frequencies are weighted by the term  $|\omega|$  to account for that fact. This band-limited linear filter is called *ramp filter* or *Ram-Lak filter*, named after V. Ramachandran and S. Lakshminarayanan.

Other filter functions are common, mostly to achieve noise reduction in attenuation CT by limiting the high-frequency contributions.

Differential phase-contrast tomographic scans can also be reconstructed with the filtered backprojection algorithm in conjunction with a different filter (Pfeiffer et al., 2007b). Looking at the Fourier transform of the derivative of a function  $f(x)$ ,

$$\mathcal{FT}\left(\frac{df(x)}{dx}\right) = 2\pi i\omega F(\omega), \quad (2.65)$$

it can be seen that the ramp filter can be modified for differential data to simultaneously perform the integration. Using the so-called Hilbert filter

$$H(\omega) = \frac{|\omega|}{2\pi i\omega}, \quad (2.66)$$

the projections are integrated in Fourier space (Faris and Byer, 1988).

In attenuation CT, the noise power spectrum has its highest values around the cut-off frequencies, i.e. high frequency noise. In DPC-CT most of the noise power lies in the low frequencies. Filtering the high frequencies may therefore not be desirable there (Marschner, 2013). There are also attempts to use prior integration with regularization

or a radically different filter design (Burger et al., 2014).

The reconstruction of differential (phase) data is straightforward using the Hilbert filter. However, the differential nature of the projection data leads to some detrimental effects with regard to the trade-off between image noise and spatial resolution. In particular, a decrease of resolution does not lead to a decreased image noise (and thereby lower radiation dose) in the same way as in attenuation CT (Chen et al., 2011; Raupach and Flohr, 2011; Koehler et al., 2011b; Weber et al., 2011). Thus, phase-contrast CT is especially superior in higher resolution settings. Nevertheless, the superior contrast of the refractive index compared to its attenuation coefficient could outweigh this fact in many potential industrial and clinical applications.

Dark-field projections can be reconstructed analogously to attenuation projections, where instead of the linear attenuation coefficient, the linear diffusion coefficient  $\epsilon(x, y, z)$  is reconstructed (Bech, 2009; Wang et al., 2009; Bech et al., 2010).

Fan-beam and cone-beam geometries are prevalent in compact laboratory and clinical CT setups. The three-dimensional reconstruction needs to consider the geometry by including additional weights (Feldkamp et al., 1984; Fu et al., 2014). As these weights are identical for all contrast modalities, they are not explicitly discussed here.

For large fan angles and thick samples, the dependence of the phase-contrast and darkfield signals on the distance from the sample to the detector has to be taken into account in the reconstruction (Qi and Chen, 2008; Chabior et al., 2012; van Stevendaal et al., 2013). These correction can be neglected with the setup used in this work.

## 2.4.2 Statistical iterative reconstruction

While filtered backprojection offers a fast and straightforward reconstruction method, statistical iterative reconstruction (SIR) techniques provide a more flexible and potentially higher-quality approach (Fessler, 2000). SIR methods leverage statistical models of the imaging process and incorporate prior knowledge about the object being imaged, leading to improved reconstructions, particularly in scenarios with limited data or high noise levels. The trade-off for these advantages is increased computational complexity. However, advancements in computing power, particularly with GPUs, have made SIR increasingly practical. These model-based iterative reconstruction techniques are commonly used in medical imaging to offer increased image quality at lower dose levels (Noël et al., 2013a).

The image reconstructing a tomographic dataset from the measured projections can be written as a system of linear equations

$$A\mathbf{f} = \mathbf{p} , \tag{2.67}$$

where  $\mathbf{p}$  describes the measured projections,  $A$  the system matrix and  $f$  the reconstructed volume. For the tomographic reconstruction, the inverse problem

$$f = A^{-1}p \quad (2.68)$$

has to be solved.

To solve this problem, a cost function is formulated which is then minimized. The cost function can be formulated as a penalized log-likelihood function

$$L = \left\| \mathbf{A}\mathbf{f} - \mathbf{p} \right\|_{\mathbf{w}}^2. \quad (2.69)$$

Simply minimizing this cost function leads to many physically implausible solutions, as this problem is ill-conditioned. Meaning, many solutions fit the originally measured images. Therefore, a so-called regularization function has to be added

$$L = \left\| \mathbf{A}\mathbf{f} - \mathbf{p} \right\|_{\mathbf{w}}^2 + \lambda R(T). \quad (2.70)$$

The regularization functions used in this work include the quadratic regularization and the Huber regularization.

The quadratic regularization function is

$$R_Q(\mathbf{f}) = \sum_i \sum_{j \in \mathcal{N}_i} m_{ij} (f_i - f_j)^2, \quad (2.71)$$

with  $\mathcal{N}_i$  being the neighborhood of pixel  $i$ ,  $m_{ij}$  the weight factor for adjacent or diagonal neighbors. Physically implausible images are penalized using this regularization function, leading to more meaningful minimization solutions.

The Huber regularization (Huber et al., 1981) penalizes differences between neighboring pixels either linearly or quadratically, depending on a threshold  $\gamma$ :

$$R_{\text{Huber}}(\mathbf{f}, \gamma) = \sum_i \sum_{j \in \mathcal{N}_i} m_{ij} \begin{cases} \frac{(f_i - f_j)^2}{2\gamma^2} & \text{for } |f_i - f_j| \leq \gamma \\ \frac{|f_i - f_j| - \gamma/2}{\gamma} & \text{for } |f_i - f_j| > \gamma, \end{cases} \quad (2.72)$$

thereby preserving edges in the resulting image better than the quadratic regularization (Zhang et al., 2013).

Statistical iterative reconstruction (SIR) has been successfully applied to grating-based phase-contrast CT measurements and has been shown to deliver increased image quality at greater flexibility (Koehler et al., 2011a; Xu et al., 2012; Hahn et al., 2015; Birnbacher et al., 2018).

The choice of statistical model is an important aspect of SIR. Employing a Poisson model instead of the Gaussian model can lead to more accurate results at very low photon counts. This is the case as approximations made in the Gaussian model lead to a biased reconstruction (Mechlem, 2015).

Other important components of the SIR include the method of discretization, the forward model, the statistical model and the minimization algorithm.

Details about these parts of SIR are discussed in detail in various literature (Fessler, 2000; Hahn, 2014; Hahn et al., 2015; Mechlem, 2015).



# CHAPTER 3

## Experimental Setup & Data Processing

In this chapter the experimental setup used to generate the data for the subsequent chapters is described in detail. Further, the single processing steps are outlined, starting from the raw images that are recorded in the detector and culminating in the reconstructed tomograms.

This study includes the investigation of human specimens; hence was conducted in accordance with the Declaration of Helsinki and was approved by the local ethics committee (Ethikkommission of the Ludwig-Maximilian-University, Munich). All participants gave written informed consent before inclusion after adequate explanation of the study protocol.

### 3.1 Phase-contrast computed tomography setup

The experimental setup used in this work was designed to deliver highly sensitive phase-contrast tomographic measurements of biological soft-tissue samples. It was optimized to produce high image quality for the systematic assessment of potential applications of phase-contrast CT in biomedical applications. More details on the design, optimization and performance of the setup can be found elsewhere (Willner, 2011; Hipp, 2013; Birnbacher et al., 2016; Willner, 2016).

The Talbot-Lau interferometer consists of three binary line-gratings, which were fabricated on silicon wafers using the LIGA process (Mohr et al., 2012). The grating periods are  $5.4\ \mu\text{m}$ . The grating lines are filled with gold to a height of 60 to  $70\ \mu\text{m}$  for the source and analyzer gratings  $G_0$  and  $G_2$ , whereas the filling height of the phase grating  $G_1$  is  $5.2\ \mu\text{m}$ . The filling height of the phase grating corresponds to a phase shift of  $\pi$  for a X-ray energy of 27 keV, which is thus called the design energy of the setup. The duty cycle, which describes the ratio of filled areas to substrate areas is 0.6.

The distance between the gratings  $G_0$  and  $G_1$  as well as between  $G_1$  and  $G_2$  is 85.7 cm. Thus, the grating configuration is called symmetric. The inter-grating distance was optimized to give a high visibility and sensitivity. The sample is mounted

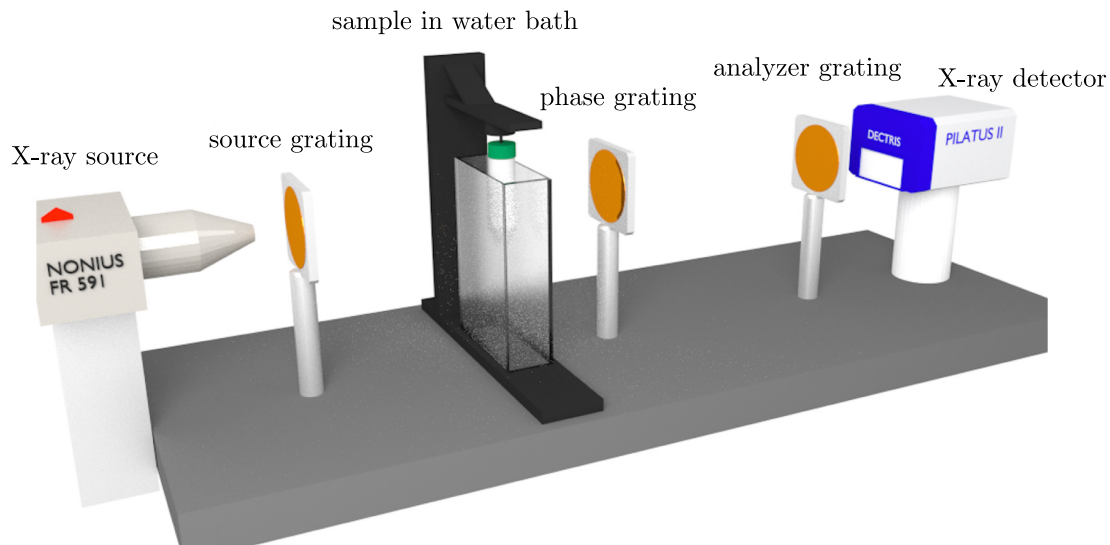


**Fig. 3.1 | Sketch of the laboratory phase-contrast CT setup.** The setup includes – from left to right – an X-ray source and the source grating, the sample in a water bath, the phase and analyzer gratings and the X-ray detector. Figure adapted from Willner (2016).

closely in front of the phase grating. Unless stated otherwise, the biomedical samples are measured in formalin-filled Falcon tubes, which were itself submerged in a water bath to avoid phase-wrapping artifacts (Zanette et al., 2011; Willner et al., 2014).

The X-rays are generated by an rotating anode X-ray tube of the type Enraf Nonius FR 591, which is operated at 40 kVp and 70 mA. The target material is molybdenum. Further, a single photon counting X-ray detector of the type PILATUS II, fabricated by Dectris Ltd., Switzerland is employed. In contrast to flat-panel or CCD-based detectors, it features no read-out noise or dark-current and is thus especially suited for statistical measurements involving low photon counts. Additionally, its box-like point spread function enables measuring the high spatial frequencies in the image which is especially important for differential phase-contrast measurement (Bech et al., 2008).

The detector is equipped with a silicon sensor of 1 mm thickness to achieve sufficient absorption and thus quantum efficiency of the high-energy end of the X-ray spectrum. The pixel pitch is  $172\ \mu\text{m} \times 172\ \mu\text{m}$ , which leads to an effective pixel size at the sample position of around  $100\ \mu\text{m} \times 100\ \mu\text{m}$  due to the geometric magnification of the imaging setup. The detector features 487 pixels in horizontal and 195 pixels in vertical direction.

Figs. 3.1 and 3.2 present a sketch and a photograph of the experimental setup, respectively.

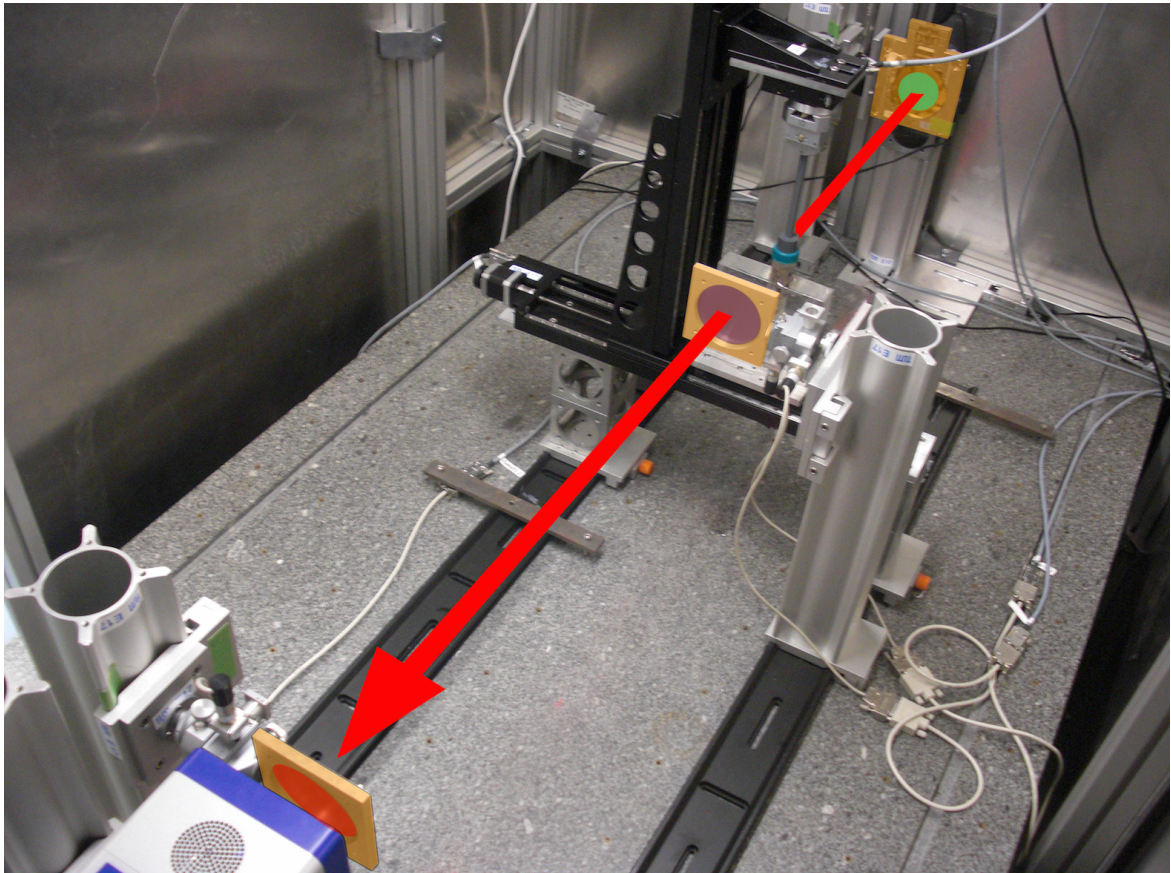


**Fig. 3.2 | Photograph of the laboratory Talbot-Laut interferometer setup.** The setup consists of three gratings that are highlighted in color. The beam path is highlighted by a red arrow. Right in front of the second grating, the sample holder is visible. The sample is located in the cylindrical tube, which is submerged in a water bath. The X-ray tube source is located in the next hatch, outside of this image. On the bottom left, the X-ray detector is visible. The setup is mounted on top of an optical table for additional stability. Figure adapted from Willner (2016).

## 3.2 Data processing for phase-contrast computed tomography

This section describes the various steps in processing the measured data to yield artifact-free attenuation, differential phase and dark-field projections. In tomographic scans, these are then used to reconstruct the three-dimensional image volume of the sample. Most of the processing steps are only addressed briefly here, as they have already been covered in great detail in various literature (Velroyen, 2015; Hahn, 2014; Marschner, 2013; De Marco, 2015; Tapfer et al., 2013; Marschner et al., 2016b).

### 3.2.1 Pre-Processing

Some image operations have to be performed before effective signal extraction can take place. This includes the detection of dead, hot or corrupt pixels and their subsequent correction. The correction is typically achieved by filtering operations, e.g. with a median filter. These corrupt pixels originate from defect detector elements and would without correction lead to severe artifacts in the final images.

In some cases, image resolution can be increased by image deconvolution. This operation reverses to some degree the blurring effects of a finite source size and detector point spread function (PSF). In grating-based phase-contrast imaging, the deconvolution is best applied before the signal extraction procedure (De Marco, 2015). Generally, image deconvolution can offer increased resolution at the cost of an increase in image noise and some computational effort. This thesis focuses on procedures and algorithms for noise reduction and shortening of measurement times and not as much on improving image resolution. Therefore, deconvolution was not applied in the presented studies, although its application would be possible.

### 3.2.2 Signal Extraction

After the pre-processing procedures the three image signals attenuation, differential phase and dark-field are to be extracted from the measured intensities. There are several methods available to perform the extraction which have specific benefits and disadvantages.

**Fourier analysis** The fastest, albeit most inflexible method of processing the acquired phase-stepping curves is by performing a Fourier analysis for each pixel. There are very efficiently implemented algorithms (*FFT: Fast Fourier Transform*) available. Further, the method simultaneously yields the higher order contributions that can play

a role when using highly coherent sources (Bech, 2009). However, only equally spaced and fully sampled stepping curves lead to accurate results. Fully sampled in this case means that an integer number of grating periods was sampled.

**Least-Squares processing** The phase-stepping curve can also be analyzed using a standard least-squares fit. The properties and results of this method are similar to Fourier analysis.

**Weighted least-squares processing** A more sophisticated processing method uses a weighted least squares (WLS) fit (Hahn, 2014; Press et al., 2007). It has several advantages, although it is computationally more expensive. First, the probability distribution of each measurement point is taken into account. This leads to more accurate results, especially in the case of low photon counts where the probability of points measured at the minimum and maximum position of the curve can differ significantly. Second, the algorithm additionally returns the statistical information of the fitted results. This information describes the confidence in each pixel of the projections. It can be used as weighting in a statistical iterative reconstruction scheme, which can lead to improved reconstruction results (Hahn, 2014). Third, the WLS algorithm is able to accurately process stepping curves that were not sampled completely and/or equidistantly.

In this method the stepping curve

$$I(x_g) = a_0 + a_1 \cos\left(2\pi \frac{x_g}{p_t} - \phi_1\right) \quad (3.1)$$

is expressed in its linear form

$$I(x) = A_0 + A_1 \cos(x) + B_1 \sin(x), \quad (3.2)$$

where  $2\pi \frac{x_g}{p_t}$  was substituted by  $x$ . The new fit parameters  $A_0$ ,  $A_1$  and  $B_1$  denote the mean of the curve and the amplitude at  $x = 0$  and  $x = 0.25$ , respectively. An exemplary stepping curve is visualized in Fig. 3.3. The original fit parameters that are needed to calculate the three images can be obtained by

$$a_0 = A_0, \quad \phi_1 = \arctan\left(\frac{B_1}{A_1}\right) \quad \text{and} \quad a_1 = \sqrt{A_1^2 + B_1^2}. \quad (3.3)$$

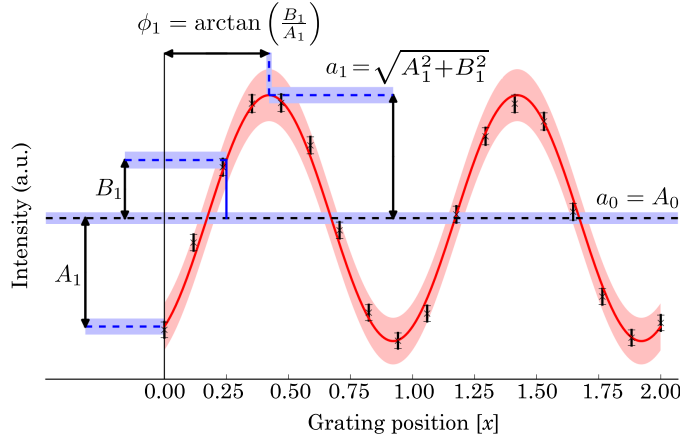


**Fig. 3.3 | Weighted least-squares processing.** A phase stepping curve showing the uncertainties of the measured intensities as well as the fit results and their uncertainty intervals. Figure adapted from Hahn (2014).

This linearized equation can be expressed in general form

$$\hat{I}(x) = \sum_{m=1}^3 \beta_m X_m(x), \quad (3.4)$$

where  $\boldsymbol{\beta} = (A_0, A_1, B_1)^T$  and  $\mathbf{X}(x) = (1, \cos(x), \sin(x))^T$  contain the estimated parameters and the vector of basis functions. A weighted least-squares cost function

$$S = \sum_{i=0}^{N-1} \frac{1}{\sigma_i^2} \left[ I(x_i) - \sum_{m=1}^3 \beta_m X_m(x_i) \right]^2 \quad (3.5)$$

is derived from this model, which is then solved for each pixel. Here,  $N$  denotes the total number of phase steps that were recorded and  $\sigma_i$  describes the uncertainty of the measured intensity  $I(x_i)$  at position  $x_i$ . The main contribution of uncertainty or noise of the intensity is counting statistics, which can be modeled by a Poisson distribution (Revol et al., 2010; Koehler et al., 2011b). Thus, the uncertainty is estimated as

$$\sigma_i = \alpha \sqrt{I}, \quad (3.6)$$

where  $\alpha$  is a constant depending on the detector calibration. In case of photon-counting detectors, where measured intensities directly represent photon counts,  $\alpha = 1$ .

This weighted least squares problem is solved by computing the gradient of Eq. (3.5) with respect to each of the estimation parameters and set it to zero. A detailed derivation thereof is given in Hahn (2014), Section 3.2.

The final output are the fit parameters and their standard deviation  $\sigma$  for each of

the three signals for each pixel. The standard deviations are indicated qualitatively by the colored areas in Fig. 3.3.

**Iterative processing algorithm** *The method presented here was published in "Helical X-ray phase-contrast computed tomography without phase stepping" (Marschner et al., 2016b).*

In certain cases, usage of one of the previously introduced processing algorithms can lead to unsatisfactory results. These cases include a faulty or imprecise phase-stepping procedure, which entails that the stepping curve is sampled at inaccurate or even unknown positions. Then, the conventional algorithms are unable to return the correct values of the three image signals. In particular, the retrieved values depend on the differential phase contrast signal in the reference scan, which introduces a systematic error in the measurements (Marschner, 2013; De Marco, 2015; De Marco et al., 2018). This periodic error in the retrieved projections leads to artifacts in the reconstructed tomograms. Other cases where the conventional algorithms return wrong values include fluctuations in the X-ray tube power or in the interferometer visibility during a stepping procedure. Both of these effects lead to fluctuations in the measured intensities, which disturb the signal extraction process.

To compensate for these effects, an iterative processing algorithm for phase-stepping data is used (Wang and Han, 2004). This algorithm treats the unknown stepping positions as latent or hidden variables and approximates them alternatingly with the image signals. Therefore, it is able to correct for systematic fluctuations in the stepping positions, which leads to improved image results (Velroyen, 2015; De Marco, 2015; Marschner et al., 2016b).

Again, the intensity curve is described by its linearized form

$$I(x_i, k) = A_0 + \alpha_i A_1(k) \cos(x_i) + \beta_i B_1(k) \sin(x_i), \quad (3.7)$$

where  $k$  denotes the pixel index,  $x_i$  the stepping positions and  $i$  the index of the stepping positions. The parameters  $\alpha_i$  and  $\beta_i$  are linked to the the stepping positions by

$$x_i = \arctan \frac{\alpha_i}{\beta_i}. \quad (3.8)$$

A log-likelihood function can be defined as

$$-\log \mathcal{L} = \sum_k \frac{1}{\sigma(k)^2} \left[ \sum_i \left( I(x_i, k) - (A_0(k) + \alpha_i A_1(k) \cos(x_i) + \beta_i B_1(k) \sin(x_i)) \right)^2 \right], \quad (3.9)$$

where  $\sigma(k)$  weights the pixels assuming Gaussian noise.

The iterative algorithm consists of two alternating steps. First, using a reasonable starting value for the stepping positions  $x_i$  e.g. equidistant stepping over one period, the parameters  $A_0$ ,  $A_1$  and  $B_1$  are evaluated for each pixel independently using least-squares fitting. Second, with the parameters calculated in the first step, the optimal value for  $x_i$  is calculated for each stepping image separately by again solving a linear system of equations using least-squares fitting. These two steps are then repeated until the change in stepping positions between consecutive iterations is below a threshold and thus convergence is assumed.

Note that the parameters  $A_0$ ,  $A_1$  and  $B_1$  depend on the pixel number and not on the stepping position while  $\alpha_i$  and  $\beta_i$  only depend on the stepping position. Thus, the deviation from the ideal stepping positions that is recovered by the algorithm is constant over the whole projection. Consequently, only globally wrong stepping positions can be corrected well by the algorithm. These can occur if the grating period deviates from the expected period or the stepping motor is inaccurate.

In the case of inhomogeneous gratings or imperfect alignment the grating period is not constant over the area of the grating. These deviations from the optimal grating shape are very common and can be amplified by thermal effects. The sampling of the stepping curve varies over the field of view when such gratings are used in a phase-stepping procedure. These local effects can only be corrected partially by the algorithm in the current form.

However, one could imagine to modify the presented algorithm for better performance in such conditions. Instead of fitting the stepping positions globally, variations of the stepping positions over the field of view would be allowed. These variations could take the form of two-dimensional ramps or polynomials. Fitting these additional parameters for each projection should prove possible, since there is enough information available: the projections consist of several tens of thousand pixels. However, solving this modified model – i.e. minimizing the log-likelihood – remains subject of further work.

### 3.2.3 Post-Processing

The signal extraction yields three projections, one for each of the modalities. Most of the time, the differential phase-contrast projection is affected by artifacts that stem from setup or measurement imperfections. Most predominantly, there is a global or spatially varying offset – a so-called ramp – superimposed on the differential phase-contrast images. To mitigate for these artifacts, post-processing methods are employed. Additional processing steps are performed as preparation for the tomographic reconstruction. These include the mitigation of ring artifacts, the detection of corrupted projections and the determination of the center of rotation.

**Offset correction** First, the offset in differential-phase values that is superimposed on the differential phase-contrast projection needs to be corrected. The offset usually varies over the field of view, e.g. as a two-dimensional ramp. There are several methods to achieve successful elimination of this offset. The adaptive differential phase recovery (ADPR) is most commonly used for grating-based phase-contrast imaging (Tapfer et al., 2013). In certain cases, an extension to allow for higher order polynomials may be necessary (Velroyen, 2015). Overall, these methods reliably remove the offsets in most of the cases. Their major drawback however is the need for sample-free areas in the projections. Consequently, the object is not allowed to cover the whole field of view in any projection. This precludes the algorithm from being applied to local tomography scans. There, other methods have to be employed for offset correction. In many cases, subtracting the mean value of the projections line-by-line is sufficient.

We now propose another offset and ramp correction technique, that does not rely on sample-free areas. It is based on the assumption that features of the sample vary considerably faster than the offset/ramps. Therefore, the spatial frequencies of sample information and artifact – i.e. offset – information are significantly different. In particular, the ramp artifacts are encoded in the lowest frequencies while the sample information is contained in the medium to high frequencies. The idea now is to remove or weaken the contribution of the low-frequency components. The first step consists of transforming the projection into the frequency domain, which is achieved by applying a two-dimensional discrete Fourier transform. Then, the amplitude of the lowest frequencies' components – e.g. the first 5% of elements – is set to zero. Subsequently, an inverse Fourier transform is performed to regain the image in the spatial domain. Visual inspection of the resulting image or the difference image will help finding the optimal cut-off frequency, which can then be used for all projections of the current tomographic scan and maybe even similar scans in the future.

We applied the frequency space ramp removal (FSRR) to an exemplary projection of

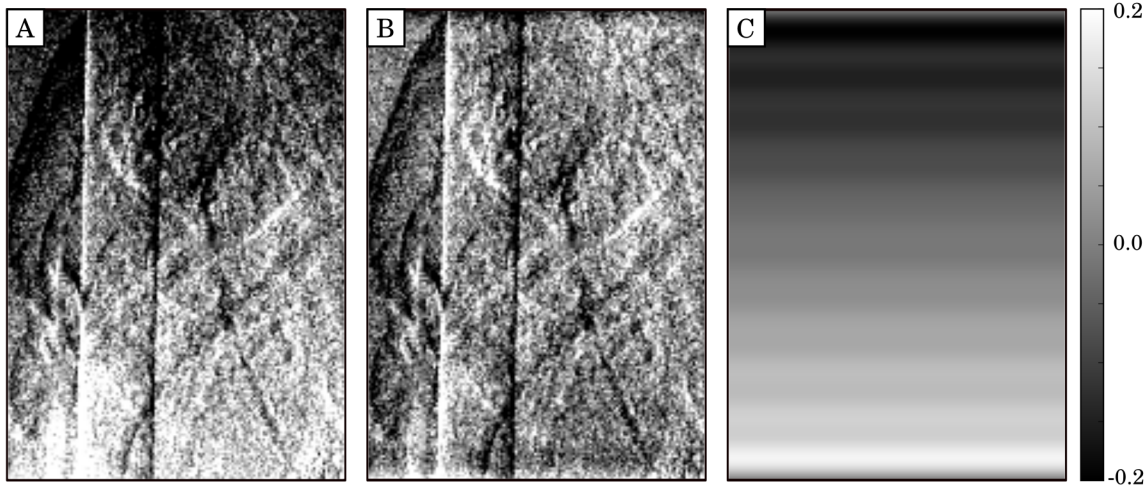


**Fig. 3.4 | Fourier transform based ramp removal.** Without corrections, the differential phase-contrast projection (width: 140px, height: 195px) contains artifacts in form of two-dimensional ramps (A). After the frequency space ramp removal, the artifacts are significantly reduced (B). Panel (C) shows the calculated correction map that was subtracted from the original projection.

a local tomography scan, which was measured with the experimental setup described above. In a local tomography scan the whole field of view is covered by the sample and ADPR is not applicable. The original projection, the result after ramp removal and the difference image are shown in Fig. 3.4. The original differential phase-contrast projection is superimposed by a ramp, i.e. the values at the top of the projection are higher than the values at the bottom. FSRR was applied with the following parameters. The amplitude of the first five positive and negative frequencies in vertical direction was set to zero. The amplitudes of the horizontal frequencies remained unchanged. If necessary, the method can also be applied to the horizontal frequencies to correct horizontal ramps. After application of the ramp removal algorithm, the projection appears much more homogeneous and the phase ramp was successfully removed. The difference image shows a ramp similar to the one in the original projection.

Note the higher order variations visible in the difference image, which are undesirable. Also, there are unwanted artifacts at the top and bottom edges of the corrected projection.

Both these effects might be mitigated by decreasing the amplitudes more smoothly, starting at the cut-off frequency. Additionally, the cut-off frequency was not systematically optimized and could still be improved to achieve better image quality. Further, the artifacts at the borders of the image could be mitigated by padding the image prior to performing the Fourier transform.

**Ring artifact mitigation** The measured raw images are inhomogeneous across pixels, which results in ring-shaped artifacts in the tomographic reconstruction. This well-known effect from attenuation-based CT also occurs in grating-based imaging, due to inhomogeneous detector response or defects in the gratings. There, it can affect all three image signals. To mitigate this effect, either the sample, the detector or the focal spot of the X-ray tube source is moved after each projection. The projections are then shifted back before reconstruction to obtain images absent of ring artifacts. The projections should be shifted by integer multiples of a pixel to avoid interpolation, which decreased the effective spatial resolution. Additionally, completely defective pixels or areas of pixels are excluded from the measurements by using the mean of the surrounding areas.

**Detection and interpolation of corrupted projections** Some differential phase-contrast projections may be irreversibly affected by artifacts. This can be the result of a failed signal extraction or an unsuccessful offset correction. Signal extraction can fail if one or more of the phase-stepping projections are corrupt due to setup instabilities – e.g. a drop in X-ray intensity.

These corrupt differential phase-contrast projections have to be detected and subsequently excluded from the tomographic reconstruction, which can be achieved by various methods.

If weighted least-squares processing was used, the mean uncertainty of the fit parameters can be used as a metric. Projections whose mean value is much higher than the norm can be considered corrupt and should be excluded.

It is also possible to use the projections themselves to automatically and reliably determine corrupt projections. In this case, the sum of the absolute values of each projection is calculated. Values much higher than the median of all mean values are considered corrupted.

Corrupted projections can either be directly excluded from the reconstruction in a SIR reconstruction by setting its weight to zero or interpolated using neighboring projections. The latter case is also applicable to conventional FBP reconstructions.

**Center of rotation determination** The center of rotation (CR) is an important parameter that is needed for tomographic reconstruction. An incorrect center of rotation leads to reconstructed images with undesirable image quality. This ranges from being slightly blurred to being severely affected by reconstruction artifacts.

There are various techniques to detect the CR from the measured projection. The method used in this work is based on cross-correlation between opposing projections.

In particular, each pair of opposing projections is compared, i.e.,  $\theta = 0^\circ$  and  $180^\circ$ ,  $\theta = 1^\circ$  and  $181^\circ$ , etc. The cross-correlation yields the relative displacement of the opposing projections, which is used to calculate the CR. The displacement of all projection pairs are averaged which gives the center of rotation. This method is only applicable to scans over 360 degrees.

In cases where the axis of rotation is not parallel to the detector columns – i.e. a tilted axis of rotation or a tilted detector – the CR varies along the height of the projection. In this case, a CR has to be calculated for each slice separately in order to avoid blurred reconstructions. This is achieved by performing the cross-correlation for each individual slice. However, noise in the images may lead to inaccurate results when only using single slices instead of whole projections. More accurate results can be obtained by modeling the axis of rotation as rigid object, i.e. the CRs for each slice have to lie on a straight line. The line is calculated by performing a linear regression on the measured CRs. The accurate CR for each slice can now be gathered by evaluating the fitted line at the corresponding height. This algorithm has proven to be very robust and is routinely used with various CT experiments, both grating-based and attenuation-based.

In practice, a global center of rotation is passed to the projector, together with a rotation angle. The rotation angle describes the tilt of the rotation axis with regard to the detector lines. The reconstruction is then performed as if the detector had been tilted during the measurement, which gives accurate results. Rotation angles of around  $0.5^\circ$  are typical for the measurements that were obtained with the described experimental setup.

## CHAPTER 4

# Helical X-ray phase-contrast computed tomography without phase-stepping

### Short summary

In this chapter an approach is presented that allows for the acquisition of phase-contrast and dark-field tomography with a continuously rotating sample or gantry. This makes very short measurement times possible, which are an important prerequisite for clinical or industrial applications of grating-based phase-contrast and dark-field imaging. The novel approach relies on a helical sample motion coupled with fringe scanning and a more advanced method of signal processing to obtain the stepping curves without grating movement. The experimental results presented in this chapter demonstrate the effectiveness of the proposed approach. The results, figures and text parts presented in this chapter have mostly been published in *Helical X-ray phase-contrast computed tomography without phase stepping* (Marschner et al., 2016b).

### 4.1 Introduction

One of current research's major goals is the translation of phase-contrast and/or dark-field computed tomography into the clinical or industrial setting.

However, both of those settings require very short measurement times, which cannot be achieved with the phase-stepping procedure as it relies on the translation of one of the gratings. This necessary translation limits the rotation speed of the sample or the gantry, which is a limiting factor in the reduction of the total acquisition time. Keep in mind that clinical absorption CT systems operate at speeds of several rotations per second. Further, the phase-stepping procedure requires a very precise translation of one of the gratings, which results in strict stability conditions of the system.

Recently, several procedures were proposed to circumvent the need of phase-stepping at each rotation step.

While interlaced phase-stepping (Zanette et al., 2012) allows a continuous rotation by combining rotation step and phase step, one of the gratings still needs to be moved.

This implies the same stability conditions as any other phase-stepping procedure. Additionally, the translation of the grating is limited with respect to speed and accuracy and therefore restricts improvements in rotation speed and image quality.

In comparison, single-shot fringe analysis is an approach that can retrieve the phase information without a stepping procedure (Wen et al., 2009; Bevins et al., 2012). It is also possible to fabricate gratings in a way that they intrinsically feature different stepping positions for different detector lines in order to obtain the phase information from only one image (Ge et al., 2014). However, the major shortcoming of these single-shot approaches is a decrease in spatial resolution, due to the fact that multiple pixels are merged to extract the phase information.

Fringe scanning has also been implemented using an electromagnetic phase-stepping procedure (Miao et al., 2013). There, the focal spot of the X-ray tube is moved via an adjustable electromagnetic field, thereby achieving relative motion between sample and fringe pattern.

The reverse projection method (Zhu et al., 2010) also enables phase retrieval without the need of a stepping procedure. This is achieved by a linear approximation of the stepping curve at its steepest point. However, this entails that the retrieved phase is only correct for small refraction angles, which effectively decreases the dynamic range of the system. To obtain both absorption and phase-contrast information, two interferograms at opposing angles have to be recorded, which requires a full scan over  $360^\circ$ . Furthermore, the dark-field signal cannot be simultaneously obtained by this method. A similar approach (Diemoz et al., 2011) utilizes a linear approximation in the reconstruction step. There, only one interferogram is needed to obtain a combined image containing information both from attenuation and refraction. However, it is not possible to obtain separate maps of the absorption and refraction of the measured object. The reverse projection method will be discussed in detail in Chapters 5 and 6.

It is also possible to record a full stepping curve without moving the gratings. Instead the imaging setup is moved (Kottler et al., 2007). In this case, the sample is moved over different detector positions instead of performing a translation of the gratings. If the reference phase is not constant over the area of the detector, the same region of the sample is recorded at different fringe phases by this scanning approach. Different fringe phases correspond to different relative positions of the gratings in a traditional phase-stepping approach. Therefore, a stepping curve can be obtained by combining these different areas as illustrated in Fig. 4.1. In summary, a phase-stepping is performed without translating the gratings. The recorded stepping curve is analogous to that obtained with the standard technique.

This fringe-scanning method has been illustrated to work for radiographic scans at

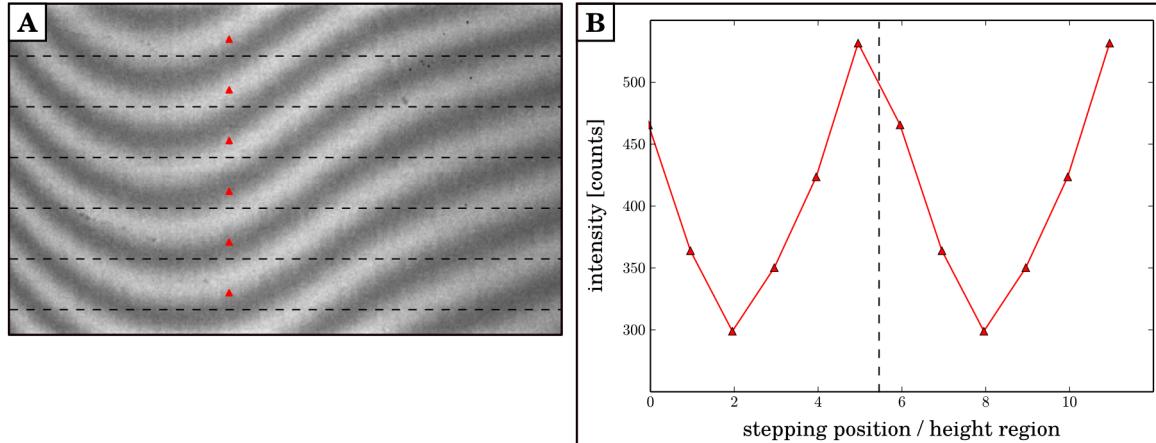


**Fig. 4.1 | Principle of Moiré fringe-scanning.** The interferogram (A) with a size of  $327 \times 195$  pixels shows Moiré fringes introduced by a deliberate mismatch of the relative positions of the phase grating and the analyzer grating. A stepping curve can be obtained by combining the height regions ( $327 \times 30$  pixels), marked by dashed lines. An exemplary stepping curve, obtained by using the pixels marked by red triangles, is shown in panel (B). Figure adapted from Marschner et al. (2016b).

synchrotron facilities as well as in a laboratory setup (Arboleda et al., 2014). Furthermore, a commercial, absorption-based mammography system was converted to a grating interferometry system (Roessler et al., 2014) using such a fringe-scanning approach. It features multiple commercially available gratings and several line detectors. Recently this approach was adapted to achieve dark-field radiography of pigs (Willer et al., 2018) and human patients (Willer et al., 2021).

In this chapter, we extend the fringe-scanning approach to the tomographic case.

## 4.2 Methods

### 4.2.1 Grating alignment in a fringe scanning setup

The grating alignment procedure differs for a phase-stepping or a fringe-scanning measurement. In a phase-stepping configuration the reference phase would ideally be constant over the whole detector area, which is achieved by perfect alignment of the gratings. In the fringe-scanning approach, the sample is recorded at different fringe phases by translating the sample. Thus, the scan approach requires the generation of a periodic fringe phase to encode the phase signal in detector positions.

To achieve a periodical fringe phase the gratings  $G_1$  and  $G_2$  are purposely misaligned. Moiré fringes appear when slightly modifying the inter-grating distance. This is the result of a period mismatch between  $G_1$  and  $G_2$  caused by the beam divergence, i.e., the changed magnification. Additionally, angular misalignment of the gratings around

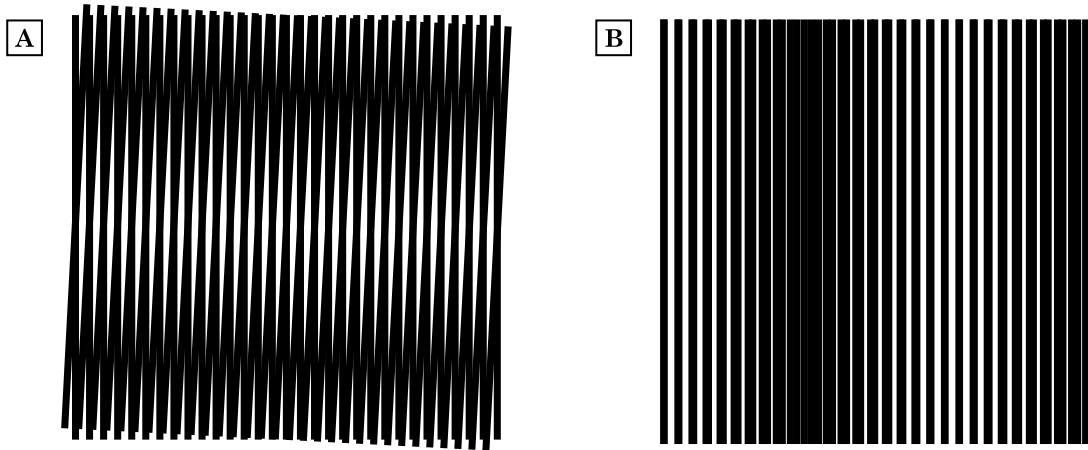


**Fig. 4.2 | Schematic showing the origin of Moiré fringes with gratings.** Two gratings with identical periods form horizontal Moiré fringes when they are slightly rotated with respect to each other, as shown in panel (A). Perfectly aligned gratings with slightly mismatched periods lead to the emergence of vertical Moiré fringes (B).

the optical axis results in horizontally oriented fringes – assuming vertically oriented grating structures. These effects are schematically depicted in Fig. 4.2.

In the experimental case, the fringes are tilted instead of being perfectly horizontal or vertical due to non-uniformity and other imperfections in the three gratings. The orientation of the fringes can be adjusted by slightly rotating one of the gratings (Momose et al., 2009; Chabior, 2011).

In general, misalignment of the gratings leads to a reduction of the interferometer visibility. However, slight misalignment around the optimum alignment position has only little effect on the visibility (Deng et al., 2020).

### 4.2.2 Helical fringe-scanning phase-contrast computed tomography

We propose to adopt a helical motion of the tomographic axis to achieve the translation of the sample for fringe-scanning. In medical CT systems a helical scanning procedure is employed to extend the field of view and reduce measurement time (Kalender, 1994). There are already theoretical, simulation and first experimental studies on helical scanning procedures for PCCT (Qi et al., 2011; Li et al., 2013; Fu et al., 2014). However, none of these methods eliminate the need for phase-stepping for each single projection and, thus, do not allow for a continuous sample rotation. With our method a continuous helical rotation of the sample or the gantry can be achieved because no stepping of the gratings is needed.

In the following we describe how a scanning-type system similar to the one described

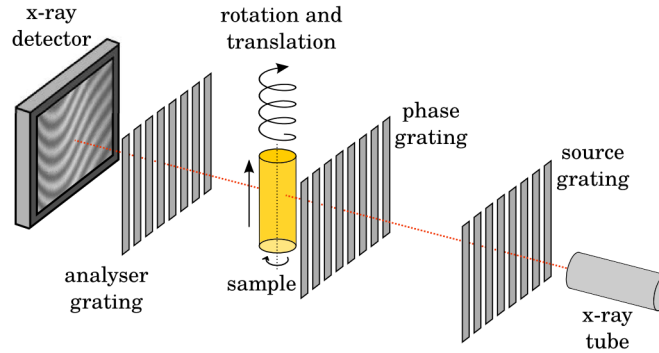


**Fig. 4.3 | Schematic of the helical fringe-scanning CT setup.** A conventional, three-grating Talbot-Lau interferometer is tuned in a way that the phase-contrast signal without sample is periodic. During the tomographic scan the sample is translated upwards, in addition to its rotation. This helical motion ensures that each part of the sample transverses every flatfield phase-shift and a complete stepping curve can be recorded. Figure adapted from Marschner et al. (2016b).

by Kottler et al. (2007) can be realized by upward motion of the tomographic axis during rotation. A sketch of the employed setup and the proposed helical motion is given in Fig. 4.3.

The measurement procedure and subsequent combination of projection areas to stepping series is illustrated in Fig. 4.4. For each angle, each part of the sample has to be in the field of view at least three times, each at a different fringe phase. This is necessary because at least three data points are needed to extract the three image signals: attenuation, differential phase and dark-field. That means that the pitch  $p$  has to be lower than  $p \leq \frac{1}{3}$ . The pitch is defined by the ratio of upward movement per rotation and the detector height. Assuming a tomographic scan over only 180 degrees, two steps can be recorded with one rotation. In this case, the pitch can be as high as  $p \leq \frac{2}{3}$ .

To be able to apply a standard processing algorithm, a full period of the stepping curve has to be sampled at equidistant positions. Therefore, the vertical movement per rotation is dependent on the period of the Moiré fringes in the interferogram.

The minimum number of helical rotations corresponds to the number of phase steps  $M$  that are 'planned' to be recorded for each projection. After  $M + 1$  rotations, the phase of the Moiré fringe has to be the same as before the first rotation. Therefore, the number of rotations  $M$  is chosen to be the same as the number of complete fringes  $k$  visible in the interferogram. The upward movement per rotation is then given by the active area of the detector divided by  $M + 1$ . The active area of the detector is the area that is covered by the  $k$  complete fringes.

Alternatively, it is also possible to use just one fringe that spans the whole detector

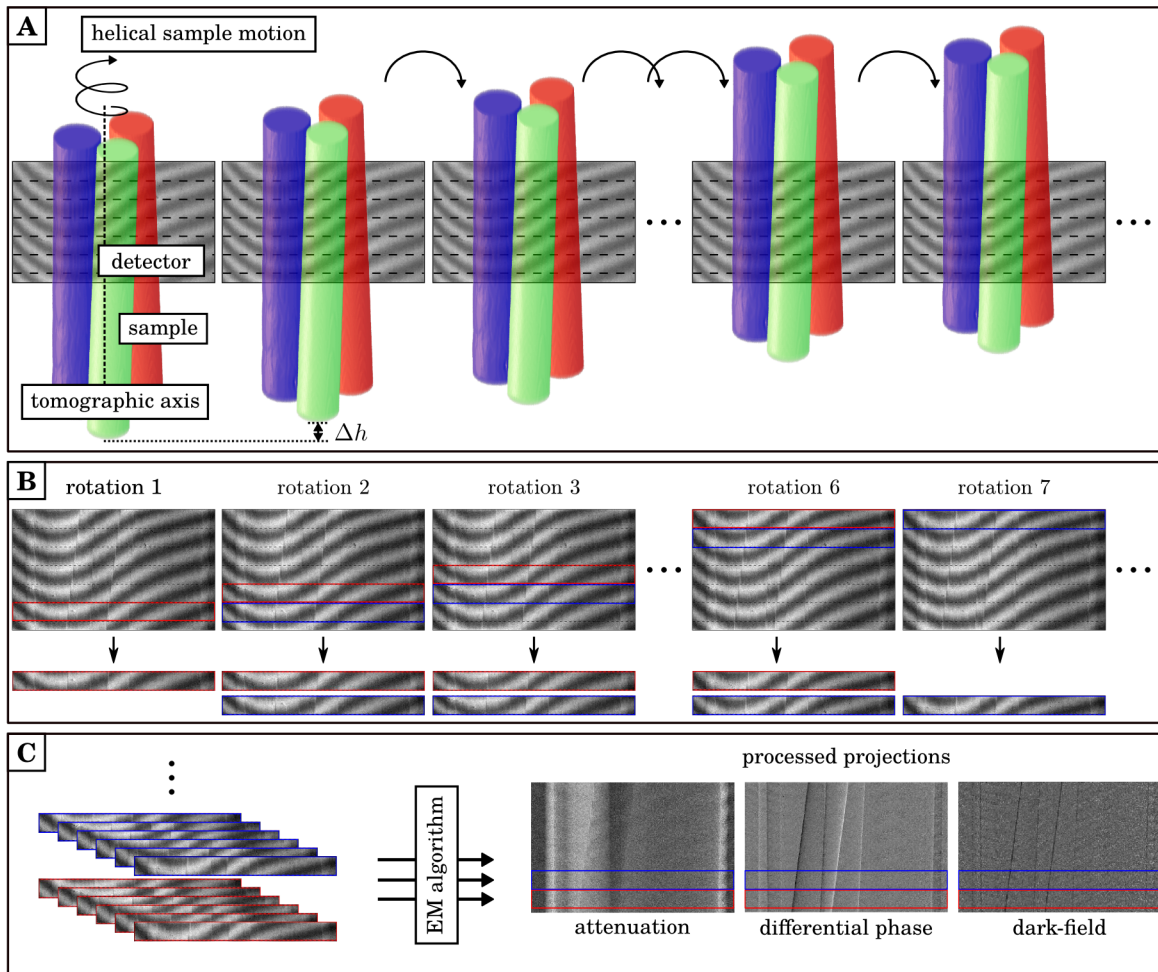


**Fig. 4.4 | Principle of helical fringe-scanning computed tomography.** The sample is continuously moved upwards during the tomographic scan. After each rotation, the sample has traversed one of the dashed areas marked in the projections and has covered a height of  $\Delta h$  (A). The regions for each part of the sample are then combined for each rotation (B). The projections of each region essentially form a phase stepping scan. The three image signals can be extracted using one of the processing algorithms. At last, the processed projections of each region can be combined to yield the complete attenuation, phase-contrast and dark-field projections (C).

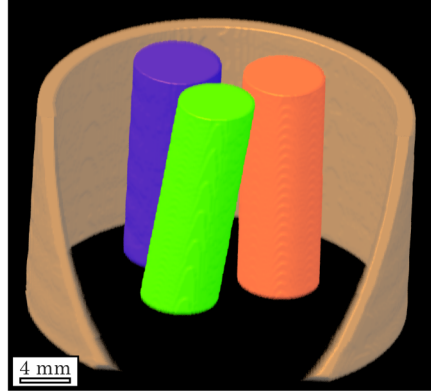


**Fig. 4.5 | Three-dimensional rendering of the phantom sample.** The measured phantom consists of three plastic rods of PMMA (red), LDPE (blue) and POM (green), each with a diameter of approximately 6 mm. The water inside and outside of the plastic tube was made transparent in this rendering.

area. Then, the number of rotations and the corresponding upward movement per rotation can be chosen freely. However, tuning the fringes this way can be difficult due to inhomogeneous grating structures. In conclusion, a scanning type system for tomography can be realized by combining the helical movement with a suitable fringe period.

### 4.2.3 Experimental setup and sample

The experimental setup is described in Section 3.1. The measured phantom consists of three plastic rods of PMMA ( $C_5H_8O_2$ ), LDPE ( $C_2H_4$ ) and POM ( $CH_2O$ ), each with a diameter of approximately 6 mm. They are measured in a tube with a diameter of 3 cm filled with water, which is itself put in a water bath to avoid phase wrapping artifacts (Zanette et al., 2011; Willner et al., 2014). A three-dimensional rendering of the sample can be seen in Fig. 4.5.

## 4.3 Results

In this chapter, we present first experimental results of CT measurements obtained with the proposed helical fringe-scanning method. A tomographic scan is carried out using the described setup and phantom. Per rotation,  $N_\theta = 600$  images with an exposure time of  $t = 1$  s each are recorded. Note, that the sample is not rotated continuously but is instead rotated before each exposure – step & shoot – due to limitations of the motor control software. The period of the Moiré fringes in vertical direction is tuned to be around 36 pixels. This is achieved by a deliberately introduced

slight misalignment of the gratings  $G_1$  and  $G_2$ . With the purpose of sampling a complete stepping curve, the vertical motion between two images is 0.05 pixels, which results in a vertical movement per rotation of  $\Delta h = 30$  px. In total,  $M = 6$  rotations are recorded for each region of the sample.

Fig. 4.4(B) illustrates the interferograms with the object in the beam for each of the 6 rotations at the same view angle. The regions of interest indicated by red boxes are combined in one stepping series. The processed attenuation, differential phase and dark-field projections are shown in Fig. 4.4(C).

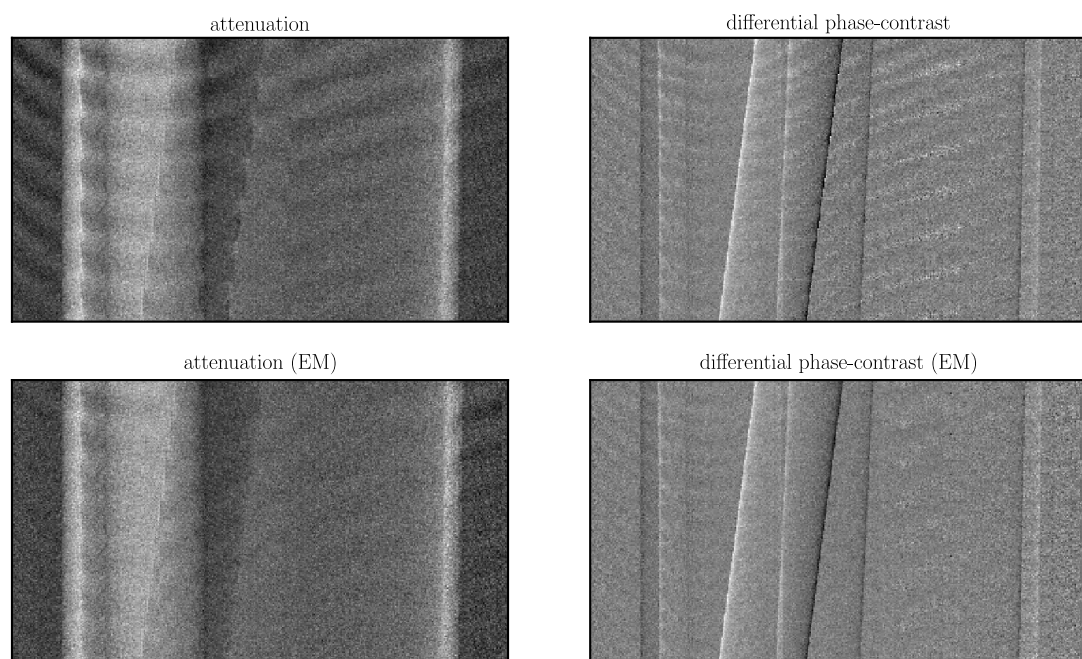
In this manner, a region of 3 mm (30 pixels with 100  $\mu\text{m}$  effective pixel size) of the sample is covered. The total exposure time for each region is  $t_{total} = MN_{\theta}t = 1$  h. For each additional rotation (10 minutes) a new region of the sample can be processed, because this region has already been in the field of view  $M - 1$  times. All together, the measurement consists of 13 rotations, which corresponds to a sample coverage of 2.4 cm. Additionally, reference images without the sample were recorded before and after the tomographic scan.

Fig. 4.4(C) shows the retrieved attenuation and differential phase projections of the measured phantom obtained as described above. The size of the retrieved projections is 365 pixels  $\times$  240 pixels, which is larger than the field of view of the detector. In principle, there is no limit on the z-coverage, that is on the vertical size of the sample. Just one additional rotation is needed when the size of the sample is increased by  $\Delta h$ . As a result, there are no constraints imposed on the vertical field of view by the gratings or the detector.

As mentioned previously, imperfect and inhomogeneous gratings lead to bent and tilted fringes over the field of view. In our experiment the fringe period is smaller in the left part than in the right part of the interferograms, with the period ranging from 35 to 40 pixels. Therefore, the sampled stepping curve is not of exactly one period in all areas. In these cases, standard processing leads to an error that is dependent on the fringe phase of each pixel in the interferogram which results in remaining fringes in the projections.

As in the traditional phase-stepping scheme, these artifacts are a result of grating instabilities that lead to wrongly sampled stepping curves. In addition, the recorded "phase steps" do not cover exactly one period resulting in incompletely sampled stepping curves. Applying conventional signal retrieval algorithms to incompletely sampled stepping curves leads to artifacts in the processed projections (De Marco, 2015). As these incompletely sampled stepping curves occur in the helical fringe-scanning method, artifacts become visible in the retrieved projections, as illustrated in Fig. 4.6.

In order to mitigate these artifacts, the expectation maximization (EM) algorithm



**Fig. 4.6 | Combined attenuation and phase-contrast projections of the helical scan.** The top row shows the attenuation and differential phase-contrast projections that were calculated using a conventional signal retrieval algorithm. Because of varying fringe periods, periodic artifacts are visible. The bottom row shows the same projections processed with the EM algorithm. It is able to significantly suppress the artifacts. The attenuation and phase-contrast images are each scaled from  $-0.87$  to  $1.36$  and  $-\pi$  to  $\pi$ , respectively.

is used to extract the three signals from the phase stepping data. This algorithm is able to correct for systematic variations in the stepping positions, as described in Section 3.2.2. It treats the unknown stepping positions as latent or hidden variables and approximates them, together with the image signals. Thus, artifacts arising from a non-equidistant sampling of the stepping curve can be avoided. Future gratings obtained with improved fabrication processes may be more homogeneous, which will make the alignment procedure less challenging and may make the usage of advanced processing algorithms obsolete.

The fringe periods and thereby also the stepping positions are not constant over the whole projection in our experiment. Therefore, we divided the projections in regions spanning the whole height of the detector and a width of 30 pixels. Using this algorithm instead of a conventional least-squares fitting of the image signals – i.e. only the first step of the EM algorithm – the fringes in the projections can be greatly reduced which increases the quality of the reconstructions significantly. Exemplary projections processed with the conventional and the novel EM-algorithm are displayed in Fig. 4.6. The remaining fringes in the projections could potentially be eliminated by employing more advanced correction methods as proposed in (De Marco et al., 2018).

Artifacts can also be a result of thermal drift of the gratings. The acquisition of the phase steps in helical fringe-scanning PCCT is separated by a full rotation and thus by a longer timespan than in a phase-stepping acquisition. For this reason, the scheme is more sensitive to thermal drifts. However, the thermal drift of our setup posed no problem for the acquisition of helical PCCT data. Further, the EM processing scheme would also be able to compensate for these effects and therefore avoid artifacts in the processed projections.

The processed projections are finally used for a tomographic reconstruction. First, the vertical displacement of the projections due to the helical motion is corrected. Then, filtered backprojection is employed to reconstruct the distribution of the linear attenuation coefficient and the refractive index decrement. A cone-beam projector is used that models the actual geometry of the experimental setup correctly. In the case of the differential phase-contrast projections, a Hilbert filter kernel (cf. Section 2.4) is applied to perform the necessary integration (Pfeiffer et al., 2007c). Fig. 4.7 displays an axial slice of the measured sample in attenuation and phase contrast. The three plastic rods are clearly visible in the tube filled with water. The image quality is comparable to conventional phase-contrast scans.

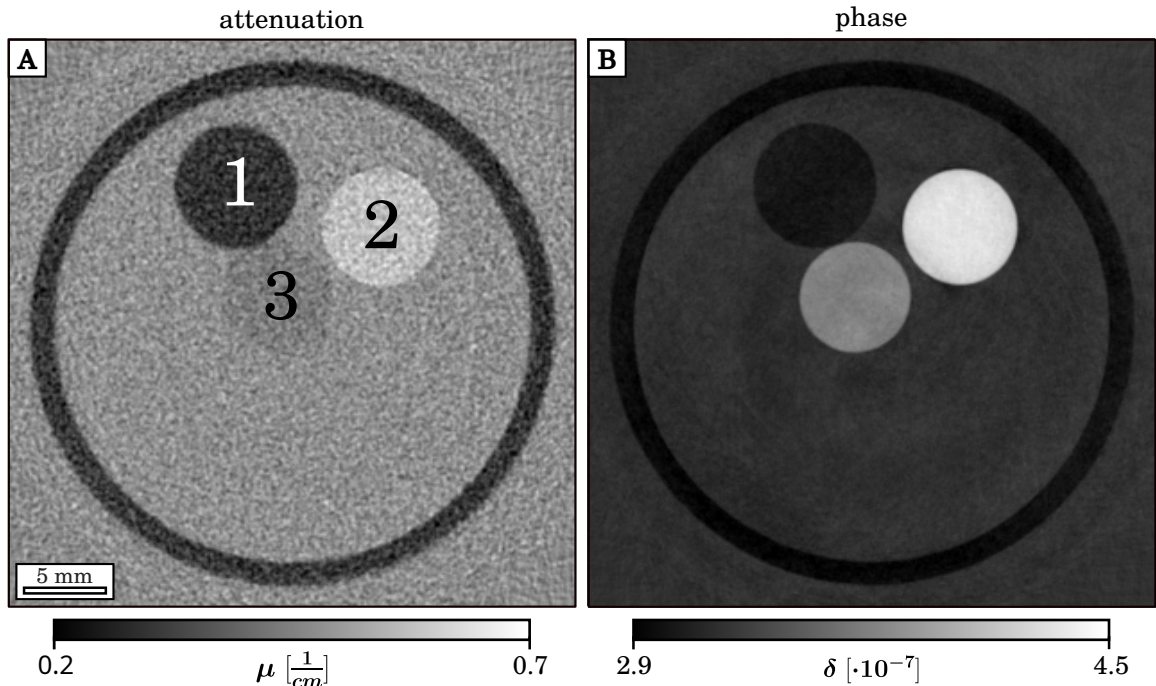


**Fig. 4.7 | Exemplary slices of the tomographic reconstruction.** The reconstructed slices show the LDPE (1), POM (2) and PMMA (3) rods inside the water-filled cylinder which are marked in the reconstruction of the linear attenuation coefficient (A). Slight artifacts are visible in the phase-contrast reconstruction (B), which stem from the remaining artifacts in the projections as shown in Fig. 4.6. The projections were retrieved using the EM algorithm and reconstructed via filtered backprojection. Figure adapted from Marschner et al. (2016b).

## 4.4 Discussion

We have shown a method that – for the first time – enables to perform a phase-contrast CT scan with stationary gratings and delivers the complete sample information without any spatial interpolation. The essence of this statement is that we are able to extract the three imaging signals for each pixel separately. In contrast, previous methods used a combination of several pixels to extract the image signals (Wen et al., 2009; Bevins et al., 2012; Ge et al., 2014) resulting in an inherent decrease in spatial resolution or the number of pixels in the final image, respectively. Nevertheless, the resolution of our novel acquisition method can be worse than a phase-stepping acquisition due to inaccuracies in the experimental implementation.

Additionally, large cone angles lead to inaccuracies in the retrieved signals and a decrease in resolution when using standard reconstruction techniques. However, large samples can also be imaged without the use of large cone angles in a scanning approach like the one demonstrated here since the FOV in vertical direction is extended beyond the area of the gratings, detector and the X-ray beam. In our case, the cone angle is less than 1 degree and can be approximated by a parallel beam. Therefore, the

resolution in z-axis direction is not affected even when non-iterative reconstruction is employed. A detailed comparison of the spatial resolution of helical and conventional PCCT may be subject of future work.

With the novel method presented here, some previous limitations of grating-based phase-contrast CT are overcome. This may lead to an easier translation of phase-contrast CT to mainstream applications possibly including clinical imaging. In particular, we have shown that grating-based phase-contrast tomography can be performed by combining a helical motion of the sample with deliberately induced Moiré fringes without the need to translate the gratings. This procedure simultaneously yields conventional attenuation, phase-contrast and dark-field data and enables a continuous rotation. This is one important requirement for clinical CT systems. In traditional phase-stepping acquisitions, the speed of the stepping motors is a limiting factor in the reduction of the acquisition time. Due to the fact that no stepping procedure is necessary, the acquisition time is only limited by the exposure time in our method. This enables faster phase-contrast CT scans.

While no true continuous scan is recorded in this work, employing a continuous rotation is straight forward and the same constraints as in absorption CT come into play, where a continuous rotation is standard in medical CT systems. In particular, the exposure time has to be small enough to ensure that there is not too much sample movement at the edges of the sample. Too much movement during the acquisition of one image results in blurring in the outer parts of the tomographic image. If we had employed a continuous acquisition here, the outer parts of the sample (sample size: 300 pixels, Section 4.2.3) would have moved  $\pi \times 300 \text{ pixels} / 600 \approx 1.5 \text{ pixels}$  during the acquisition of one image. This is roughly the size of the projection of the source size onto the detector – or in other words – the system point spread function. Therefore, no significant additional blurring would be expected in this case.

A shorter exposure time per projection and by that less sample movement during one exposure reduces the blurring that stems from continuous movement. There are several approaches to reduce the exposure time per projection in a tomographic scan.

One possibility is to simply record more projections with shorter exposure times in such a way that the total exposure time stays constant. One could e.g. acquire 2400 projections with 0.25 s exposure time instead of 600 projections with 1 s exposure time each. If we employ a photon-counting detector – which will become the norm in a few years – this will not change the noise in the tomographic reconstruction (Bech et al., 2008). This approach is independent of the flux of the tube or other setup parameters.

Additionally or alternatively, there is the possibility to use gratings fabricated with thinner, less absorbing wafers to increase the flux at the detector allowing for shorter

exposure times. Furthermore, X-ray tubes in the clinical setting have much higher flux compared to the laboratory tube employed in this study. Using a tube of this kind would result in a significant reduction of the exposure time.

The major advantage compared to previously introduced methods that allow a continuous rotation lies in the fact that the gratings can be fixed. The need to translate the gratings with a precision of fractions of the grating pitch, which is around  $5\ \mu\text{m}$ , is eliminated. With fixed gratings the mechanical stability of the system is less critical. This is especially important in systems where not the sample but a gantry consisting of source, gratings and detector is rotating (Tapfer et al., 2012). Keep in mind that a precision of 1% of the stepping curve is equivalent to a relative grating displacement of 50 nm.

In the helical fringe scanning approach the sample needs to be translated with much less precision. Usually the pixel sizes range from  $50\ \mu\text{m}$  for mammographic systems to over  $500\ \mu\text{m}$  for clinical CT systems. In our case, the pixel size considering magnification is  $100\ \mu\text{m}$  and the fringe period spans 30 pixels. Thus, a precision of 1% of the stepping curve equals a sample displacement of  $30\ \mu\text{m}$ . This stability requirement is relaxed by three orders of magnitude compared to the conventional phase-stepping approach and can be further relaxed by using larger pixel sizes and larger fringe periods. Also, this sample motion is no different to the one performed in conventional spiral CT systems and may be necessary anyway when objects larger than the area of the gratings or the detector are to be measured.

Compared to previously introduced methods that rely on fixed gratings, there is no inherent loss in resolution and the full information of attenuation coefficient, refractive index decrement and scattering strength can be accessed. This comes with the drawback of a slightly more challenging grating alignment procedure.

In conclusion, we present a method that allows phase-contrast tomography scans with continuous sample rotation without an inherent loss in resolution. Due to the scanning approach the field of view is extended in vertical direction which enables the imaging of objects larger than the field of view of the system. In addition, the stability requirements of the imaging system are relaxed due to fixed gratings.

Overcoming these limitations is an important step towards industrial and clinical application of grating-based phase-contrast computed tomography.

To improve this approach further, novel intensity-based iterative reconstruction (IB-SIR) schemes can be used (Ritter et al., 2016; Brendel et al., 2016; Teuffenbach et al., 2017), which do not rely on intermediate phase retrieval. Using these methods, variable geometry for different phase steps resulting from the large cone-beam can be considered and correctly modeled. Consequently, data from a helical fringe-scanning

acquisition with a cone-beam setup can be reconstructed correctly. Additionally, it is not required anymore to record multiple phase steps per sample area, as long as the Radon space is sufficiently sampled (Teuffenbach et al., 2017; Xu et al., 2022). This can be ensured by choosing a suitable combination of sample motion and Moiré pattern or electromagnetic phase stepping. Lately, it was shown that the oscillations from a rotating gantry of a medical CT scanner alone are sufficient to ensure adequate sampling (Viermetz et al., 2022).

# CHAPTER 5

## Two-shot phase contrast imaging

### Short summary

One of the disadvantages of the phase-stepping procedure and subsequent phase-retrieval via Fourier analysis is the emergence of statistical phase-wrapping as shown in chapter 2. This phenomenon implies a lower limit of the imaging dose that can be achieved with phase-contrast imaging which is an obstacle for clinical implementation. In this chapter, we show the detrimental effects of statistical phase-wrapping and present a possible solution for low-dose PCCT imaging. The approach presented here enables meaningful phase retrieval and thus quantitative reconstruction at lower imaging doses. Most of the results, figures, tables and text parts have been published in *Revising the lower statistical limit of X-ray grating-based phase-contrast computed tomography* (Marschner et al., 2017). Finally, the chapter is complemented by a yet unpublished section on using projection weights to circumvent current experimental shortcomings, thereby broadening the method’s applicability.

### 5.1 Introduction

There are remaining difficulties which prohibit the use of phase-contrast computed tomography in a clinical setting. Among these, the reduction of scan time and a lower exposure to ionizing radiation are especially important. Over the last years, research on attenuation-based CT has achieved significant improvement with regard to radiation dose reduction (Noël et al., 2011, 2013b; Schuhbaeck et al., 2013; Deák et al., 2013) suggesting the same possibilities for phase-contrast CT. Yet, as detailed in Section 2.3 a minimum radiation dose per projection for PCCT exists when phase retrieval based on Fourier analysis is used. Therefore, alternative methods to extract the phase information are to be examined that may be able to extract the phase information correctly even in the case of very low photon counts.

The reverse projection (RP) method is an alternative phase retrieval scheme, where the phase shift of the sample is obtained using only two phase steps and a linear approximation of the sinusoidal phase stepping curve (Zhu et al., 2010). This method is expected to have a more favorable behavior at low photon counts since it avoids

non-linearity in the phase retrieval. The noise properties of this novel technique have been investigated analytically as well as through simulation studies (Wu et al., 2014, 2015). However, these studies cover only the case of high photon statistics or low noise where Fourier-based phase retrieval still produces reliable results. Correspondingly, a closer look at the behavior of the reverse projection method at low photon counts is necessary. Especially two important properties need to be investigated in the low-dose regime: the amount of noise in the retrieved phase-contrast images as well as whether the measured values are quantitatively correct. Given these properties, the RP method could be able to solve the problem of collapsing signal propagation that occurs in the methods based on conventional signal extraction.

In this chapter, we examine the statistical properties of the RP phase-retrieval method at low photon counts and compare it to the widely-used phase-retrieval method based on Fourier analysis. We study experimentally the dependence of the standard deviation of the retrieved phase values on the number of photons per pixel evaluated over an empty region in the differential phase-contrast projections and in the phase stepping images. Additionally, we present first tomographic results obtained with the RP technique using a Talbot-Lau interferometer with a laboratory x-ray tube.

First, we use these results to compare the image quality of the image quality of the Fourier-based method. We further illustrate how the image quality of the tomographic measurements is affected by statistical phase-wrapping in the projections when employing the Fourier-based approach. Second, we assess the correctness of the quantitative values obtained by the two phase-retrieval methods for the cases of high and low photon counts. Then we combine the RP method with a weighted iterative reconstruction to optimize the method for current laboratory setups. Finally, we discuss the implications of the results for the purpose of low-dose phase contrast CT imaging.

The method of using a Fourier analysis or least-squares fit of a complete stepping curve to retrieve the phase shifts – as presented in Chapters 2 and 3 – is referred to as the phase stepping (PS) approach in this chapter.

## 5.2 Two-shot phase retrieval

### 5.2.1 Reverse projection method

The reverse projection method is an alternative method of phase retrieval that allows for phase-retrieval using only two phase steps (Zhu et al., 2010). In this approach, the sinusoidal phase stepping curve is approximated at its steepest points by a linear function. Only two projections at selected grating positions are recorded instead of

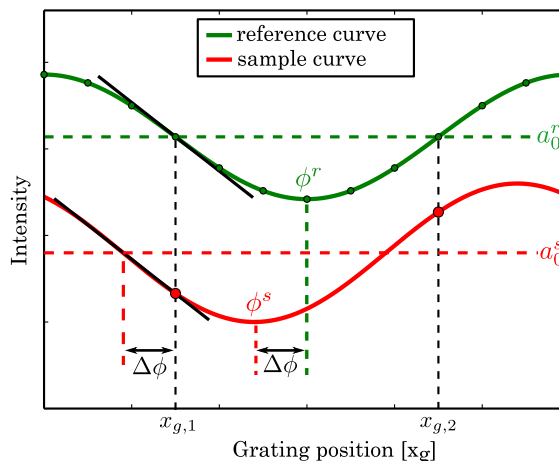


**Fig. 5.1 | Principle of the reverse projection method.** Starting from the phase stepping curve that is recorded without sample (reference scan), the sample is measured with grating positions corresponding to the two linear regions of the stepping curve. The two recorded intensities can then be used to obtain the attenuation  $a_0^s$  of the sample as well as its differential phase shift  $\Delta\phi_s$ . Figure adapted from Marschner et al. (2017).

performing a complete phase stepping scan. This method has been extended to two-dimensional gratings (Wang et al., 2012) and fan-beam geometry (Wu et al., 2013). In the following, it is reviewed shortly.

As discussed in Section 2.2, the intensity recorded at each detector pixel and grating position  $x_g$  can be expressed by

$$I(x_g) = a_0 + a_1 \sin\left(2\pi\frac{x_g}{p} + \phi_1\right). \quad (5.1)$$

The phase stepping curve has two regions, where its slope is linear – provided that a phase stepping is performed over one full period. There, it can be approximated with the linear function

$$I(x_g) \approx a_0 \pm a_1\phi_1. \quad (5.2)$$

Exemplary phase stepping curves of a sample scan and a reference scan are displayed in Fig. 5.1, where also a linear region is highlighted.

This linear approximation will now be used to determine the attenuation and phase shift of the sample. First, a reference scan is recorded featuring a full stepping curve. Using this scan, the two grating positions that correspond to the linear regions of the reference scan’s stepping curve are determined. At these points, the intensity is

$I^r = a_0^r$  and thus the grating positions can be calculated as

$$x_{g,1} = -\frac{\phi_1^r}{2\pi}p \quad \text{and} \quad x_{g,2} = \left(-\frac{\phi_1^r}{2\pi} + \frac{1}{2}\right)p. \quad (5.3)$$

The corresponding grating positions are marked by dashed lines in Fig. 5.1.

Then, a projection with the sample in the beam is acquired at each of these two grating positions. The measured intensities at these gratings positions are

$$\begin{aligned} I_1 &= I(x_{g,1}) \\ &= a_0^s + a_1^s \sin\left(2\pi \frac{x_{g,1}}{g_2} + \phi_1^s\right) \\ &= a_0^s + a_1^s \sin\left(2\pi \frac{x_{g,1}}{g_2} + \Delta\phi + \phi_1^r(x, y)\right) \\ &= a_0^s + a_1^s \sin(\Delta\phi) \\ &\approx a_0^s + a_1^s \Delta\phi \end{aligned} \quad (5.4)$$

and equivalently

$$I_2 = I(x_{g,2}) \approx a_0^s - a_1^s \Delta\phi. \quad (5.5)$$

These projections can be combined to obtain the attenuation and differential phase-contrast projections. The attenuation signal can be determined by taking the mean value of the two measurements and normalizing it to the average intensity in the reference image  $I_0 = a_0^r$ , as shown in the following expression:

$$A = 1 - T = 1 - \frac{a_0^s}{a_0^r} = 1 - \frac{I_1 + I_2}{2a_0^r}. \quad (5.6)$$

The phase shift of the stepping curve – i.e. the differential phase-contrast signal – can be calculated by subtracting Eq. (5.5) from Section 5.2.1

$$I_1 - I_2 = 2a_1^s \Delta\phi, \quad (5.7)$$

resulting in

$$\Delta\phi = \frac{I_1 - I_2}{2a_1^s}. \quad (5.8)$$

The slope of the linear function is determined by the first Fourier coefficient  $a_1^s$  of the sample scan. Since no phase stepping is performed for the sample scan, this coefficient is not known. However, a full phase stepping is performed for the reference scan which is the scan without sample in the beam. This stepping curve can be used to extract  $a_1^r$ , the first Fourier coefficient of the reference scan. If there is no small angle scattering

– i.e. no dark-field signal in the sample ( $D = 1$ ) – these coefficients can be related to each other via the constant visibility, namely

$$\frac{a_1^r}{a_0^r} = V^r \stackrel{D=1}{=} V^s = \frac{a_1^s}{a_0^s}. \quad (5.9)$$

Through rearrangement of Eq. (5.7) and substituting  $a_1^s = V^r a_0^s$ , making use of Eq. (5.9), one arrives at

$$\Delta\phi = \phi_1^s - \phi_1^r = \frac{1}{V^r} \frac{I_1 - I_2}{2a_0^s} = \frac{1}{V^r} \frac{I_1 - I_2}{I_1 + I_2}, \quad (5.10)$$

the equation for the differential phase-contrast signal.

This approximation is only valid for small values of the differential phase shift of the sample  $\Delta\phi$ . While most of the pixels are expected to be close to zero due to the differential nature of the phase-contrast signal, there are also larger values – e.g. at borders between materials. These values strongly influence the quantitative values in the reconstructed volumes due to the integration step prior to reconstruction. Therefore, it is necessary to examine the accuracy of the quantitative values in the reconstructed volumes obtained with the reverse projection method.

Additionally, non-negligible dark-field signal in the sample leads to wrongly determined phase shifts in the reverse projection method. It was shown recently that the retrieved signal then is the product of the objects scattering – dark-field – and phase shift signals (Wang et al., 2015). Thus, the phase shift is systematically underestimated in the presence of scattering in the sample.

Equivalent to a phase stepping acquisition, a set of projections obtained with the RP method at different tomographic angles can be used to obtain the maps of the linear attenuation coefficient  $\mu(x, y, z)$  as well as the refractive index decrement  $\delta(x, y, z)$ . Note that the reverse projection method was implemented slightly different in the original publication (Zhu et al., 2010). There, the two projections were obtained with only one fixed grating position combined with a full scan over  $360^\circ$ . Opposing projections can then be combined to extract the attenuation and differential phase-contrast information. This is possible since the attenuation is symmetric with rotation while the refraction is antisymmetric.

In this work, we use two projections at the same tomographic angle but different grating positions for phase retrieval. For simplicity, we will still call it reverse projection method and refrain from introducing a new name here. After all, the phase retrieval algorithm is the same in both approaches and the results of this work are also applicable to the original reverse projection method. The only practical aspect

that needs to be considered is that the original reverse projection method is not applicable to cone-beam geometries while our approach loses the advantages of stationary gratings.

## 5.2.2 Statistical properties

The statistical properties of the reverse projection method differ from those of the phase stepping method. First of all, the standard deviation of the differential phase-contrast projections is lower by a factor of  $\sqrt{2}$  in the RP method. This can be explained by the fact that the region around the zero-crossings of the sinusoidal phase stepping curve is most sensitive to phase shifts. In contrast, the region around the extrema of the stepping curve is only sensitive to changes in the amplitude of the curve – i.e. to the dark-field signal. This entails that in a phase stepping approach only half of the measured points contribute to the phase information while the other half determines the dark-field signal.

In the RP approach, only the points in the linear region are used which contribute most to the phase signal. Simultaneously, no information about the dark-field signal is obtained. Therefore, only half of the data points are needed for the same precision in the phase-contrast channel. This results in a standard deviation that is lower by the factor of  $\sqrt{2}$  compared to the phase stepping approach when the same amount of photons are used overall (Wu et al., 2015). Thus, the standard deviation of the retrieved differential phase contrast signal is given by (Wu et al., 2014)

$$\sigma_\phi = \frac{1}{V} \tilde{\sigma} = \frac{1}{V} \frac{1}{\sqrt{Na_0}}, \quad (5.11)$$

where  $\tilde{\sigma}$  is the normalized standard deviation (cf. section 2.3 and  $N$  denotes the number of recorded projections).

More interestingly, a linear phase retrieval should not suffer from the same problems at low statistics as the phase stepping approach due to the fact that no periodic function has to be fitted to the data points. This means that meaningful phase retrieval should be possible even for projections with very low photon counts and consequently statistical phase wrapping would be avoided. Despite this promising prospect, the noise properties of the linear phase retrieval have not yet been investigated in this low-count case.

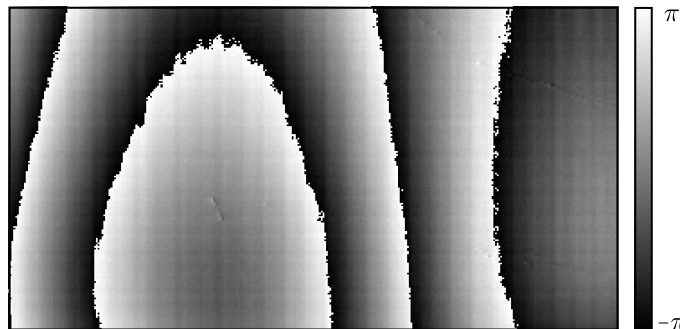


**Fig. 5.2 | Differential phase contrast flatfield.** The DPC flatfield is not flat – i.e. the differential phase is non-uniform over the field of view. Thus, it is not possible to globally select two phase-steps where the stepping curve is linear.

### 5.2.3 Limitations and adaptations

There is one major drawback of this method. The phase of the reference image has to be constant over the field of view to be able to acquire the two projections at the linear regions of the phase stepping curve. This however is challenging with current gratings and setups. Slight deviations from the design period of the gratings, other grating imperfections or non-optimal grating alignment lead to Moiré effects (cf. Fig. 4.2) and non-uniform flatfields.

An exemplary differential phase contrast flatfield is shown in Fig. 5.2. In this flatfield, the value for the differential phase shift varies over the projection from  $-\pi$  to  $\pi$  multiple times. Thus, the straight forward experimental application of the RP method is not possible.

To adapt to this, more than the two theoretically necessary phase steps are recorded. The appropriate steps are then retrospectively selected for each pixel separately, resulting in a much higher than necessary exposure time and thus radiation dose for the sample.

If enough steps are recorded, two steps close to the optimal points for phase retrieval are available for each pixel. These best step  $M_{1,2}$  out of the  $N$  recorded phase steps are calculated as

$$M_1(x, y) = \text{round} \left( \frac{N}{2\pi} \phi^r(x, y) \right), \quad (5.12)$$

and

$$M_2(x, y) = \text{round} \left( \frac{N}{2} + \frac{N}{2\pi} \phi^r(x, y) \right). \quad (5.13)$$

Combining the pixel intensities at the optimal steps  $M_{1,2}$  yields two virtual stepping images  $I_1$  and  $I_2$ , which are depicted in Fig. 5.3. The structure of the DPC flatfield can still be seen as aliasing effects in these images, as the selected steps are only close to

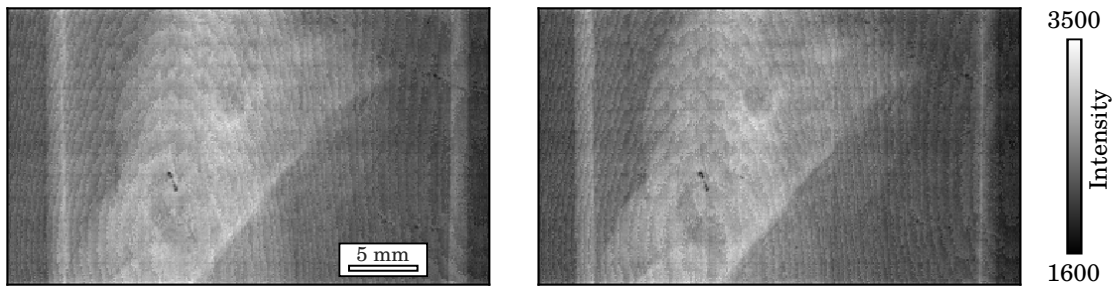


**Fig. 5.3 | Virtual stepping images.** If the flatfield phase is not uniform, the linear region of the stepping curve is located at different grating positions for each pixel. These optimal phase steps can be combined to form two virtual stepping images. They resemble those that would be recorded with a uniform flatfield.

the optimal ones due to the finite amount of recorded phase steps. These images could be recorded directly, without the artifacts, if the flatfield DPC signal were uniform.

The virtual stepping images are then used to obtain the DPC projection as described above. A resulting projection is shown in Fig. 5.4(A). It can be clearly seen that the aliasing effect is superimposed on the projection, which is a result of the slight deviation of the selected phase steps from the optimal points on the stepping curve.

Thus, a linear correction is employed for the remaining deviation from the optimal point using the remainder of the rounding operation. The correction map can be seen in Fig. 5.4(B). The resulting corrected DPC projection and its deviation from the phase-stepping DPC projection are depicted in Fig. 5.4(C) and (D).

The difference image reveals slight deviations from the phase-stepping projection. Large values are underestimated in the two-shot projection. Additionally, there are some artifacts remaining after the correction which could potentially be mitigated using higher order corrections.

Keep in mind that the frequency of flatfield acquisition during the tomographic scan has to be high enough so that there is no significant drift between the recording of the flatfield and the sample projection. Otherwise, the ramp and offset correction discussed in Section 3.2.3 has to be employed, which requires a complete phase stepping scan. Note, that a binned projection can be used for ramp correction to avoid the low-count regime where conventional phase-retrieval fails.

There is also a small systematic error that is introduced because of this approximation as the point now is farther away from the linear region of the stepping curve. By using a higher order function instead of a simple linear approximation for phase retrieval, the phase shift could also be calculated accurately with points farther away from the linear region. Consequently, fewer steps would be needed to achieve successful phase retrieval even when the reference phase is not uniform over the field of view.

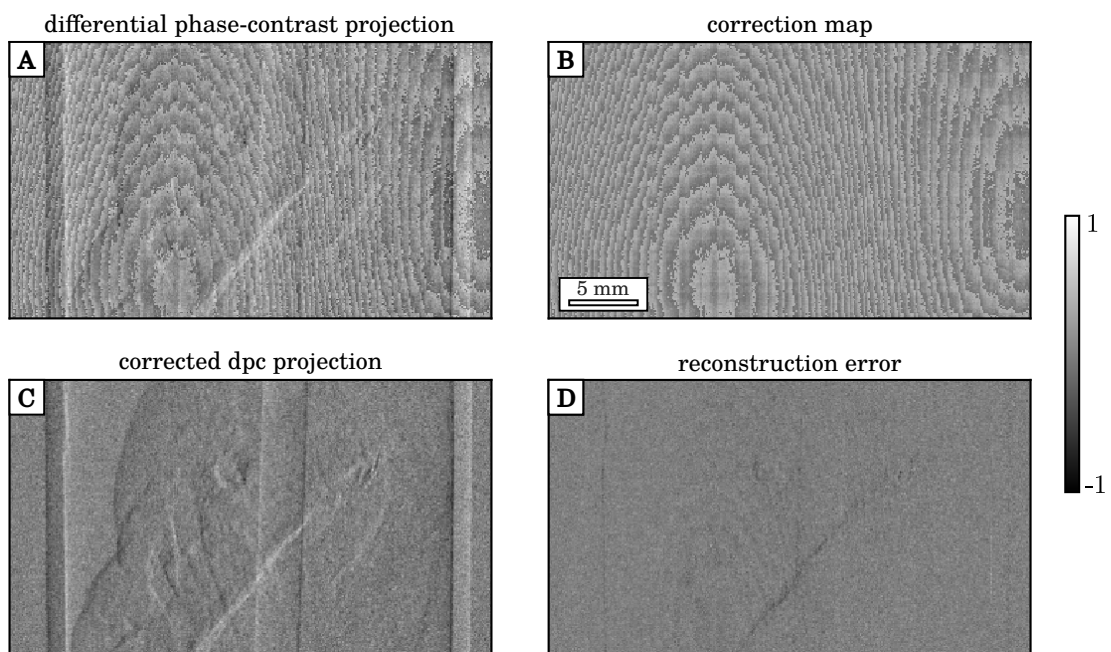


**Fig. 5.4 | Two-shot phase retrieval using virtual stepping images.** The virtual stepping images can be combined to obtain a differential phase-contrast projection (A). A correction map can be obtained using the distance of the used phase step to the optimal phase steps (B). Subtracting the correction map from the DPC projection results in a nearly artifact-free projection (C) that shows only slight differences (D) to the DPC projection obtained with the conventional phase-retrieval via phase-stepping.

However, more than two phase steps would still be required, since meaningful phase retrieval with only two points is not possible when they lie around the turning points of the phase stepping curve. If e.g. four equidistant phase steps were recorded, there would always be at least two steps – or combinations of steps – that could be used for the RP phase retrieval. In this case, the RP approach would still lead to superior reconstructions in low dose scans as will be demonstrated in the example displayed in Fig. 5.10, where even five phase steps are used for the conventional phase retrieval. In a high statistic scan, the noise levels would be similar in both approaches (cf. Eqs. 2.44 and 5.11).

Alternatively, it is also possible to combine the RP method with SIR. With SIR, it is possible to weight pixels – i.e. define their contribution to the reconstruction. In this scheme, two globally fixed steps can be used even for non-uniform flatfields if the pixels are weighted based on their potential to contribute meaningfully to the image formation. This depends on their distance in the DPC flatfields from the linear region. This method as well as experimental results will be discussed in Section 5.3.5.

## 5.3 Experimental results

### 5.3.1 Samples and measurements

A series of tomographic scans with varying exposure times per projection are recorded to investigate the different statistical properties of the PS and the RP method. For each tomographic scan we obtain a total of 1200 sample projection evenly spanning  $360^\circ$  as well as 300 reference projections. A filtered backprojection with a Hilbert filter kernel is used for the reconstruction, where also the slight cone-beam geometry is considered. For each projection, 11 equidistant phase steps are performed over one grating period. The exposure time, which is evenly distributed to the phase steps, is 0.025 s to 3.6 s per phase step and corresponds to a mean of around 15 to 2273 counts per pixel, respectively. Every second step, in total 5 steps, are used to obtain the phase stepping curves in the PS approach and the three imaging signals are extracted using a least-squares fit. Thus, the exposure times range from 0.125 s to 18 s per projection.

For the RP method, the two phase steps closest to the zero crossings of the stepping curve are selected for each pixel separately. Consequently, the exposure times ranged from 0.05 s to 7.2 s per projection, which corresponds to a mean of roughly 30 counts per pixel and 4546 counts per pixel, respectively. Note, that these exposure times are theoretical in the sense that 11 exposures are taken but only 2 particular data points – not the same for each pixel – are used for phase retrieval. This is necessary since it is not

possible to achieve a homogeneous, flat reference phase with our experimental setup. The reference images without the sample are recorded with 11 phase steps and a total exposure time of 39.6 s per projection. Consequently, the influence of the reference images on the noise in the final projections can be neglected. The measurements are carried out with the setup described in Chapter 3.

### 5.3.2 Quantitative accuracy

First of all, we evaluate a scan with long exposure – i.e. high photon counts – to verify the accuracy of the RP method, thereby investigating its applicability to tomographic scans of biological soft-tissue. It is clear that the error that is introduced due to the linear approximation of the sinusoidal phase stepping curve depends on the value of the differential phase-contrast signal.

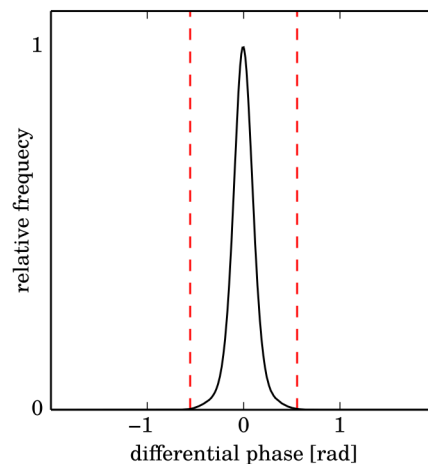


**Fig. 5.5 | Histogram of differential phase-contrast projections.** This figure shows the histogram of the differential phase-contrast projections of a tomographic scan of a biomedical sample. The red lines mark the region where the error of the linear approximation is less than 5%. Only 0.1% of all pixels lie outside of this region. Figure adapted from Marschner et al. (2017).

Thus, the distribution of values in a typical scan is of concern with regard to the approximation’s accuracy. Fig. 5.5 shows the relative frequency of occurrence of phase shift values in all of the DPC projections of the tomographic scan of a biological sample. It can be clearly seen that the values are centred around a phase shift of zero because of the differential nature of the signal. Further, the distribution of values is quite narrow with only 0.1% of pixels having an absolute value greater than  $\phi^s(x, y) > 0.55$  rad (marked by the red dashed lines). There, the absolute error of the linear approximation is 0.028 rad while the relative error is 5%. Note that the standard deviation due to Poisson noise  $\sigma_\phi=0.07$  rad is already higher than this error even in a scan with a very

Scan descr.	$\delta_{\text{formalin}}$	rel. err.	$\delta_{\text{PMMA}}$	rel. err.	$\delta_{\text{tube}}$	rel. err.
<i>Fig. 5.6</i>						
reference	$0.54 \pm 0.14$		$4.65 \pm 0.16$		$-1.94 \pm 0.15$	
RP (1172 cts)	$0.51 \pm 0.16$	-5%	$4.29 \pm 0.19$	-8%	$-1.91 \pm 0.17$	-2%
<i>Fig. 5.9</i>						
PS (70 cts)	$0.37 \pm 1.37$	-31%	$3.85 \pm 1.36$	-17%	$-1.48 \pm 1.33$	-24%
RP (76 cts)	$0.58 \pm 0.89$	7%	$4.35 \pm 0.86$	-6%	$-2.06 \pm 0.81$	6%
<i>Fig. 5.10</i>						
PS (111 cts)	$0.44 \pm 1.26$	-18%	$3.6 \pm 1.17$	-23%	$-1.78 \pm 1.39$	-8%
RP (44 cts)	$0.47 \pm 1.06$	-14%	$4.16 \pm 1.05$	-10%	$-1.98 \pm 1.03$	2%

**Tab. 5.1 | Comparison of the quantitative values in the tomographic reconstructions.** Mean values and the corresponding standard deviation of the refractive index decrement  $\delta$  relative to water, exemplary for the materials formalin (fluid inside the tube), PMMA and the Falcon tube. The mean values and standard deviations are evaluated over volumes containing  $>100,000$  voxels.

long exposure time of 18 s per projection. Also keep in mind that this scan is obtained at a setup with very high sensitivity that cannot be reached with a potential clinical setup, which has to be more compact. Consequently, even the phase-shifts of bigger objects could still be small enough to justify using the linear approximation.

An additional source of error is a change in interferometer visibility due to small-angle scattering inside the sample. However, the dark-field signal of biological soft tissue is weak and is therefore not expected to significantly disturb the results obtained with the RP method.

Still using the same high-count scan, we inspect the tomographic reconstructions of the differential phase-contrast projections gathered by the two different methods. Axial slices of the reconstructed volume of the refractive index decrement  $\delta$  are displayed in Fig. 5.6(A). A visual inspection reveals no apparent differences between the phase-contrast tomography slices of the two methods. However, a look at the line plot shown in Fig. 5.6(B) reveals slight discrepancies between the two reconstructions, especially in areas with very high and very low values. In these regions, the magnitude of the refractive index decrement is underestimated in the RP reconstruction. This is an expected result since the linear approximation underestimates large phase shifts, which correspond to high absolute values of the refractive index decrement after tomographic reconstruction. In the other regions, the values are very similar for both methods with some fluctuations due to image noise.

Additionally, the mean values in three homogeneous regions in the image volume are evaluated. The results of this analysis are displayed in rows 1 and 2 of Table 5.1. The differences of the quantitative values for formalin and the Falcon tube between

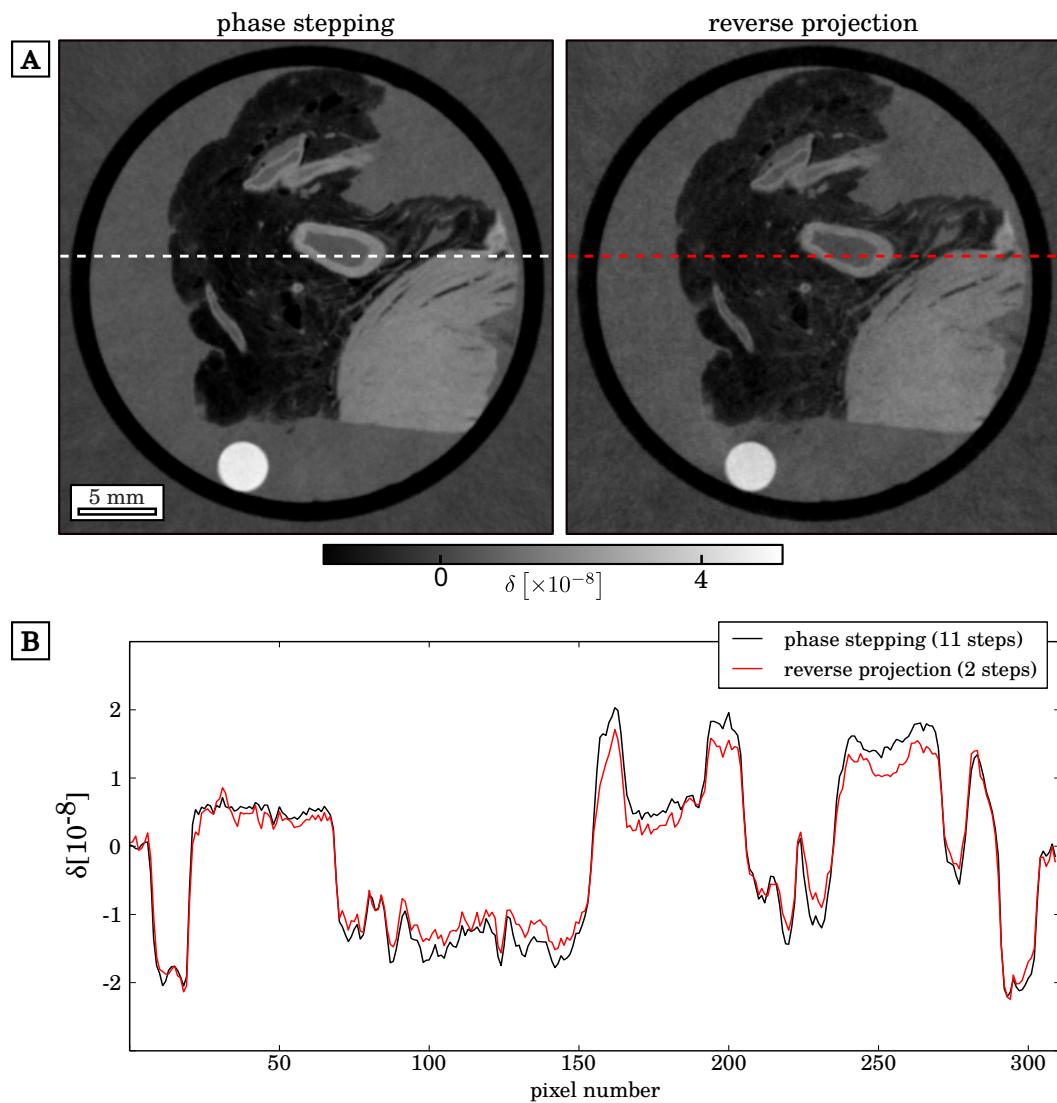


**Fig. 5.6 | Comparison of the tomographic reconstructions** (A) Comparison of tomographic reconstructions of the differential phase contrast projections, obtained with the widely-used phase stepping approach (left) and the reverse projection method (right). There are no visual differences between the two images. A more detailed comparison can be achieved by examining the line plot (B), which is taken at the position marked by the dashed lines. High values of the refractive index decrement are partly underestimated in the RP reconstruction. Figure adapted from Marschner et al. (2017).

the two methods lie well within one standard deviation. Only for the PMMA rod, which is the bright circle visible in the reconstructed slices, the values differ more significantly: as expected, the refractive index is underestimated in the RP method by around 8 % since this material exhibits a high phase shift. From this point on, the mean delta values of the PS scan with high photon counts will be used as a reference when analyzing the low-counts scans.

### 5.3.3 Statistical properties

In the next step, the dependence of the image noise or the standard deviation in the differential phase-contrast projections on the exposure time or the number of photons is examined. A region of interest is defined to evaluate the number of counts in the phase stepping images, the visibility in the reference projections and the standard deviation in the DPC projections. An example of attenuation contrast and phase-contrast projections obtained with the PS procedure and the linear approximation is shown in Fig. 5.7. Again, the visual appearance is very similar for both methods. The region of interest used for the analysis is marked by a rectangle. The mean visibility in the region of interest is measured at 18.6%.

The results of the noise analysis are shown in Fig. 5.8, which illustrates the dependency of the standard deviation in the differential phase-contrast projections on the number of photons per pixel in the stepping images. These results will now be discussed in detail.

First of all, we evaluate the measured standard deviation of the DPC projections  $\sigma_\phi$  obtained by the PS method. It can be seen that the values for projections with high photon counts agree well with the results predicted by the theoretical calculations (cf. equation 2.44). Going towards lower mean photon counts per pixel, the standard deviation rises more rapidly than the purely Poisson-based theory suggests. This can be explained by the occurrence of statistical phase wrapping. The same behavior is visible in the simulation results although there the resulting values are slightly higher. This is due to the fact that the detector used in the experiment exhibits charge sharing, an effect that is not considered in the simulations. Charge sharing introduces a correlation between neighboring pixels, which in turn reduces the standard deviation slightly, especially when the mean number of photons is low.

At even lower photon counts, the standard deviation starts to saturate and is therefore getting closer again to the theoretical prediction for high statistics. This is the result of a convergence towards the uniform limit which entails that the measured values resemble a random distribution in the interval  $I_\phi = [-\pi, \pi]$ . Thus, the retrieved phase is not correct anymore. Therefore, scans in this regime do not show an improved

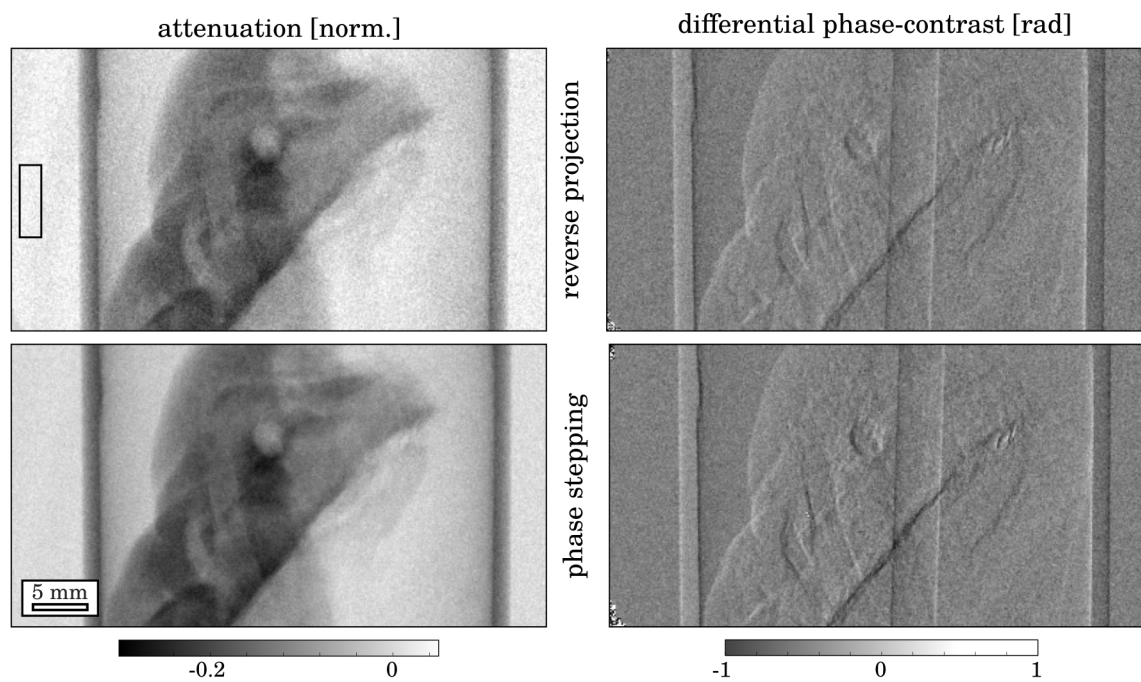


**Fig. 5.7 | Comparison of projection images obtained by both methods.** The projections obtained with the reverse projection method are shown in the top row and the phase-stepping projections are shown in the bottom row. The ROIs indicated by rectangles are used to extract the mean photon counts, standard deviation and mean visibility for the statistical analysis. Figure adapted from Marschner et al. (2017).

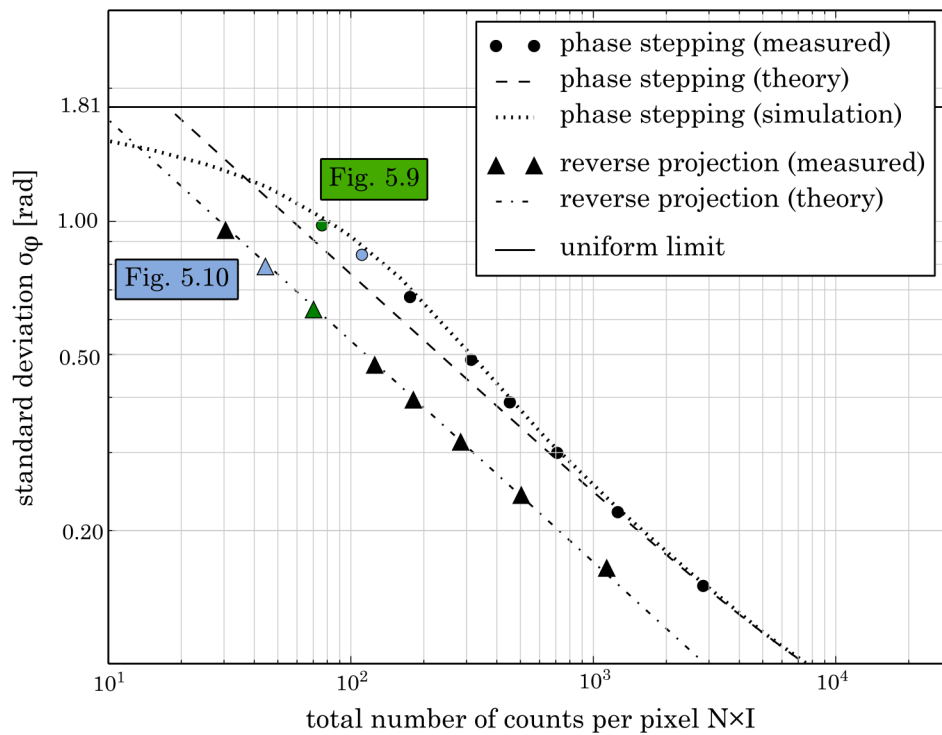


**Fig. 5.8 | Dependency of the standard deviation of the differential phase-contrast projections on the number of photon counts per pixel.** The projections obtained with the RP method show a lower standard deviation than the ones obtained with PS by a factor of  $\sqrt{2}$ . In comparison to the PS procedure, the standard deviation of the RP projections does not show a deviation from Poissonian behavior when going to lower photons counts. The tomographic reconstructions for selected measurements are displayed in Figures 5.9 and 5.10. This is indicated by the green and blue markings. Figure adapted from Marschner et al. (2017).

image quality but instead are dominated by noise.

Next, the measured standard deviation of the DPC projections obtained with the RP method is considered. Here the theoretical values are lower by a factor of  $\sqrt{2}$  compared to the PS values as explained previously. We find that the measured values agree well with the theoretical predictions. Therefore, we have confirmed experimentally the theoretical predictions and simulations for the case of high photon counts (Wu et al., 2014, 2015).

In addition to that, we show that the standard deviation follows the theoretical values of a Poisson distribution even for scans with very low photon counts. We therefore conclude that the RP method does not suffer from statistical phase wrapping at very low photon counts, in contrast to the conventional phase retrieval technique. However, it is still to be examined whether the RP approach will also yield quantitatively correct reconstructions at these low photon counts.

For this purpose, we compare tomographic reconstructions of the projections that are obtained with the two methods. The visual appearance of these images as well as the quantitative values of the refractive index decrement are evaluated. Additionally, the reconstructions are compared using two standard metrics: the root mean squared error (RMSE) and the structure similarity index (SSI).

First, we take a look at two scans that are acquired with nearly the same exposure time – i.e. mean number of photons per pixel. In the first scan, five equidistant phase steps with a mean number of 15.2 counts per pixel are used to obtain the stepping curves, which are in turn analyzed using a least-squares fit. For the RP scan, only two phase steps with a mean number of 35 counts are utilized to extract the attenuation and DPC projections. Combined, the mean number of counts per projection is then 76 per pixel for the PS and 70 per pixel for the RP method (cf. green markings in Fig. 5.8). Filtered backprojection is once again used to reconstruct the distributions of the attenuation coefficient and the refractive index decrement from the measured projections.

The comparison is displayed in Fig. 5.9. Evidently, the reconstruction of the linear attenuation coefficient has the same visual appearance for both methods. This is an expected result, since both methods simply average all phase steps for the retrieval of the attenuation projections.

However, the situation looks quite different in the phase-contrast channel, where the reconstruction of the RP projections has superior image quality. There is less noise and thus more features can be recognized compared to the PS reconstruction. This can be explained by the lower amount of noise that is present in the DPC projections of the RP method.

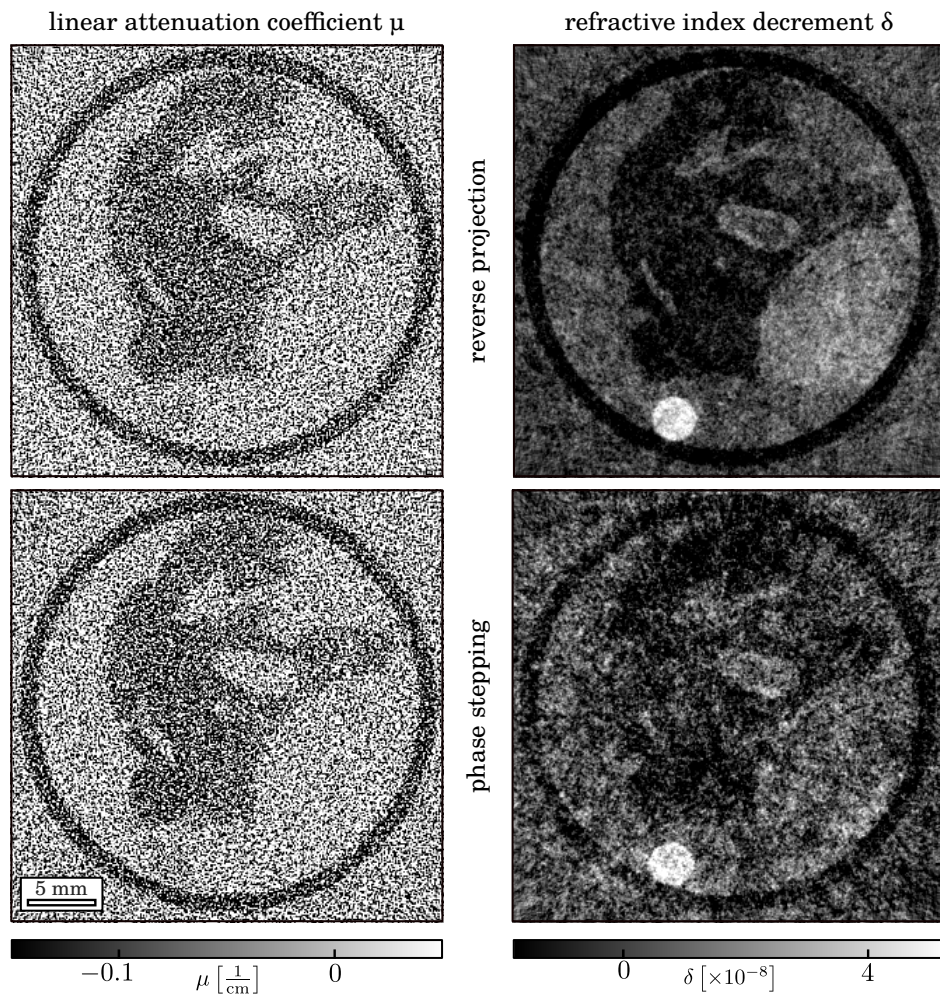


**Fig. 5.9 | Comparison of low-dose reconstructions.** Comparison of reconstructions obtained with the RP method (top, 70 counts/pixel/projection) and the PS approach (bottom, 76 counts/pixel/projection). Note, that while the total applied dose is even slightly lower for the scan obtained with the RP method, the reconstruction of the refractive index decrement still shows much better image quality and also less noise compared to the PS method. As expected, there is no visible difference in the reconstruction of the linear attenuation coefficient. Figure adapted from Marschner et al. (2017).

Additionally, the RP projections are not affected by statistical phase wrapping and its corresponding loss of signal in some pixels. This effect does not only worsen the image quality of the PS reconstruction but also affects its quantitiveness. This is evident from the comparison of the mean values of the three homogeneous regions. The results of this analysis are displayed in rows 3 and 4 of Table 5.1. Clearly, the RP method delivers more accurate values of the refractive index decrement.

For all three materials, the relative errors lie between -6 and 7 percent. In contrast, the relative errors in the PS reconstructions are between -17 and -31 percent. It is evident that the  $\delta$ -values are severely underestimated suggesting statistical phase wrapping as the cause: The phase is not retrieved correctly in pixels affected by this phenomenon. Instead, random values from a uniform distribution, which correspond to a reconstructed mean  $\delta$  of zero, are returned. Therefore, non-significant amounts of phase-wrapped pixels lead to mean values closer to zero.

The RMSE and SSI values of the two reconstructions, compared to the reference scan, are displayed in rows 1 and 2 of Table 5.2. Here, the RP methods shows better performance, too. There is a lower RMSE and a higher SSI in comparison to the PS approach.

scan descr.	RMSE [ $\cdot 10^{-8}$ ]	SSI
<i>Fig. 5.9</i>		
PS (76 cts)	1.34	0.89
RP (70 cts)	0.89	0.95
<i>Fig. 5.10</i>		
PS (111 cts)	1.26	0.89
RP (44 cts)	1.03	0.93

**Tab. 5.2** | Root mean squared error and structure similarity of the tomographic reconstructions displayed in Figures 5.9 and 5.10 compared to the reference scan.

### 5.3.4 Comparison to phase stepping

It could be argued that the superior quality of the RP reconstructions stems solely from the lower noise level in its projections compared to the PS projections as the noise level is lower for the RP approach when using the same exposure time for both methods. We compare two scans that were obtained using the same set of phase stepping images to dispute this assumption and examine more closely the influence of statistical phase wrapping.

In that case, both scans have the same number of mean photon counts per phase step, namely 22.2 counts. As before, five phase stepping images are used to obtain the

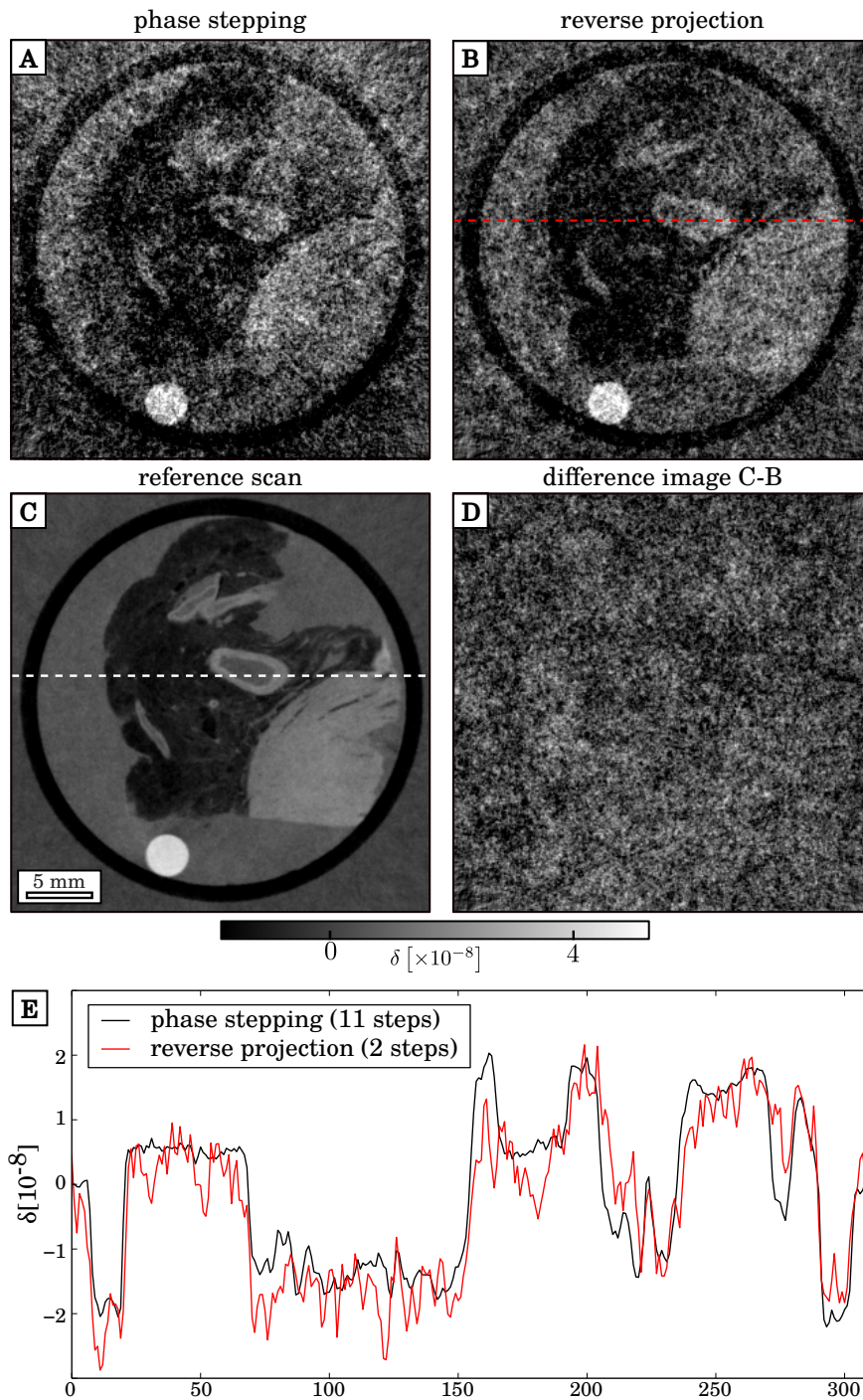


**Fig. 5.10 | Quantitative accuracy of low-dose reconstructions.** Comparison of the reconstructions obtained with the PS method (A, 111 counts/pixel/projection) and the RP method (B, 44.4 mean counts) with a reference scan (C). Panel (D) shows a difference image of (B) and (C). A plot through the lines in panels (B) and (C) is displayed at the bottom (E). Note that the values for the RP method are averaged over 4 slices and 4 pixels in direction perpendicular to the line for improved readability. Figure adapted from Marschner et al. (2017).

DPC projections for the PS method leading to a mean total number of 111 counts per pixel and projection. In contrast, only two steps are used to extract the DPC projections in the RP method amounting to 44.4 counts per pixel and projection. That means the number of counts per pixel is higher by a factor of 2.5 for the PS method (cf. blue markings in Fig. 5.8). Consequently, one would expect that the tomographic reconstruction of the PS projections features superior image quality.

However, when looking at these reconstructions (Fig. 5.10 (A,B)), it can be clearly seen that this is not the case at all. The reconstruction of the PS projections exhibits more noise than the reconstruction of the RP projections. Thus, the image quality of the RP reconstruction is superior which also leads to better feature recognition in this image. These results show that statistical phase wrapping in the projections has a drastically negative effect on the image quality in the reconstructions. Additionally, statistical phase wrapping leads to wrong quantitative values, which will be investigated next.

First, we compare visually the reconstructed values of the RP method with the reference scan using a difference image which is displayed in Fig. 5.10 (D). This image is dominated by noise and there are no features visible suggesting that the RP method is able to reconstruct quantitatively the refractive index decrement even at very low photon counts.

Second, a line plot (cf. Fig. 5.10 (E)) of the same two images is used for further comparison. Note that the line of the RP scan is obtained by averaging over 4 slices and 4 pixels in direction perpendicular to the line in order to decrease the noise level and thereby make the interpretation of the plot easier. The line corresponding to the RP reconstruction matches the reference line quite well. However, there are still fluctuations because of noise despite the averaging procedure. Overall, the quantitiveness is comparable to the analysis that is performed in Fig. 5.6.

Next, the mean  $\delta$ -values that are measured in the three homogeneous regions are inspected. The values are shown in rows 5 and 6 of Table 5.1. For all three materials, the values obtained by the RP method are closer to the reference values than the PS values. Additionally, the standard deviation in the three regions is also lower for the RP method. Finally, a comparison of RMSE and SSI of the two reconstructions (see Table 5.2, rows 3 and 4) also shows superior performance of the RP method. Overall, these findings are quite remarkable: discarding three of the five phase steps, and with that 60% of the photons, results in superior image quality and more accurate quantitative values in the tomographic reconstruction.

### 5.3.5 Tomography using projection weights

As discussed in Section 5.2.3, it is possible to adapt the reverse projection method to being applicable to non-uniform flatfields by using SIR with suitable projection weights.

In principle, one can record the two phase steps at arbitrary grating position as long as the grating positions are roughly half a grating period apart. Then, the phase-retrieval with the reverse projection method is applied as described. The resulting DPC projection is shown in Fig. 5.11(A). As expected, the projection shows severe artifacts in the shape of the DPC flatfield.

In this case, a linear correction cannot work, since the deviation from the optimal step can be as large as  $\pi/2$ . Improved results can be achieved using the sine of the deviation from the optimal point. Then, the correction factor is smallest for steps close to the optimal point and biggest for a deviation of  $\pi/2$  which is the farthest possible distance. The resulting correction map is displayed in Fig. 5.11(B).

Subtracting the correction map from the DPC projection gives a corrected DPC projection (Fig. 5.11(C)), where sample features are visible. However, there still remain rather strong artifacts that again resemble the shape of the DPC flatfield. These artifacts are in regions, where the measured points are around the turning points of the phase stepping curve. The stepping curve is least sensitive to the phase-contrast signal around the turning points. Therefore, phase-retrieval using only two steps fails in these regions, resulting in visible artifacts. These artifacts can also be seen in the difference map of the two-shot and phase-stepping projection as visualized in Fig. 5.11(D).

The location of these artifacts can be calculated using the DPC signal of the flatfield. Thus, we can create a mask to exclude this faulty data from the reconstruction to achieve better results. More accurately, the projection's pixels can be weighted based on their estimated statistical significance – i.e. their contribution to a correct reconstruction. Thereby, the influence of the artifacts on the reconstruction can be limited.

Possible weights are

$$w(x, y) = \left[ \cos \left( \frac{\Delta x_{g,1}}{p} \frac{2\pi}{N} \right) + \cos \left( \frac{\Delta x_{g,2}}{p} \frac{2\pi}{N} \right) \right]^2, \quad (5.14)$$

where  $\Delta x_{g,1}$  and  $\Delta x_{g,2}$  are the distances from the optimal grating positions. Points close to the optimal grating positions are weighted more strongly than points farther away. Fig. 5.11(E) and (F) show a map of the calculated projections weights  $w$  and

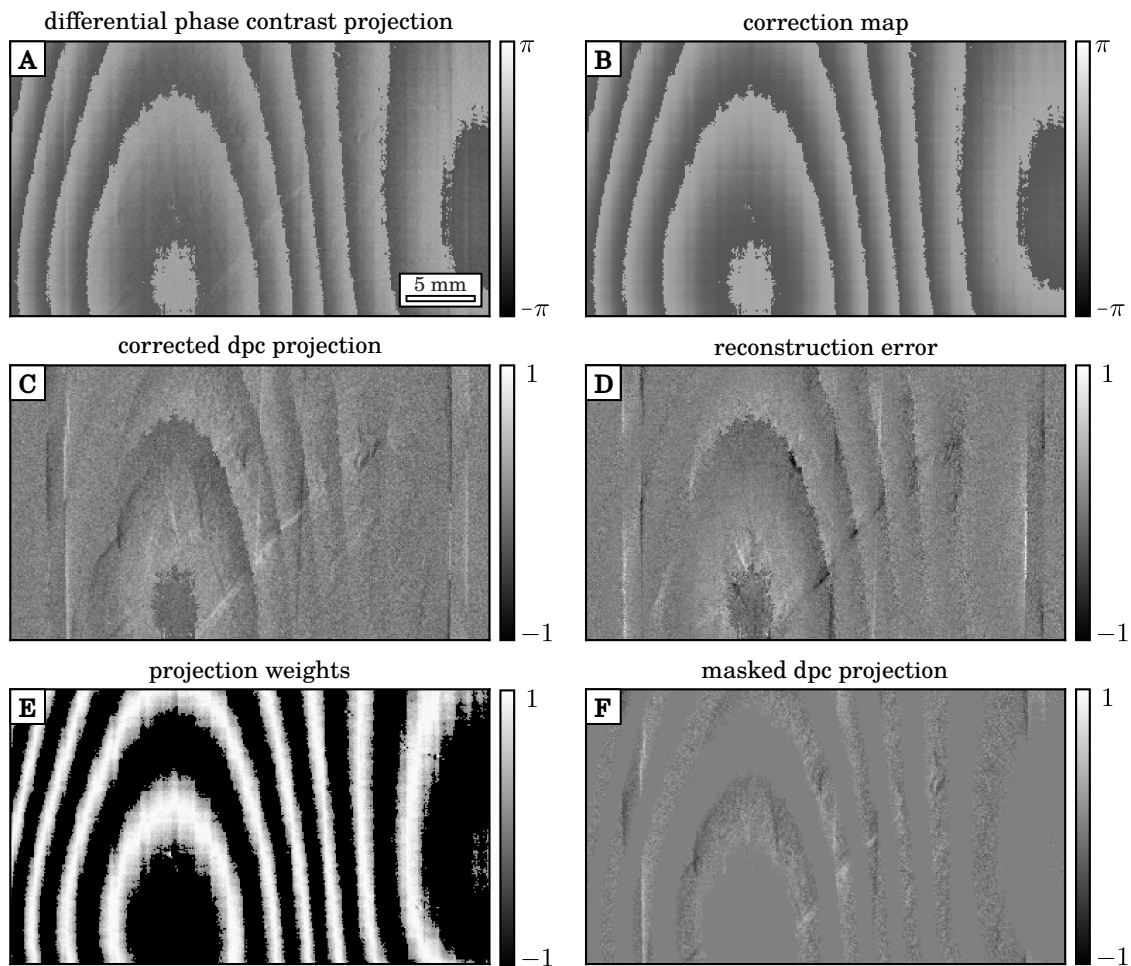


**Fig. 5.11 | True two-shot phase retrieval with non-uniform flatfields.** The resulting DPC projection (A) contains strong artifacts in the shape of the DPC flatfield, that need to be corrected using a suitable correction map (B). The corrected projection (C) reveals details of the sample but still contains artifacts in the regions where the phase-retrieval using two steps does not work because the two steps lie too close to the turning points of the stepping curve. The difference image (D) of phase-contrast and RP projection highlights these errors. Projection weights  $w^*$  (E) can be calculated from the correction map, which can be used to mask the corrupt regions of the RP projection. The masked projection (F) can be used for tomographic reconstruction.

the masked projection, respectively.

The result of the tomographic reconstructions are shown in Fig. 5.12. The straightforward FBP reconstruction (A) and the iterative reconstruction without weights (B) give nearly identical results. The wrongly reconstructed pixels in the DPC projections result in severe semicircular artifacts that decrease image quality.

Fig. 5.12(C) shows a reconstructed slice with the projection weights of Eq. (5.14) applied during reconstruction. The artifacts are reduced significantly but residual artifacts remain.

Some of the artifacts also stem from the fact that certain areas of the sample are not sampled sufficiently from certain view angles, due to the large masked areas. Flatfields that are more spatially varied would improved reconstruction quality in this regard.

Still, it seems that the proposed weights are not sufficient, yet. Keep in mind that the reconstruction of the refractive index decrement involves the integration of the *differential* phase-contrast projection. Thus, wrong pixels with high values, as present in the two-shot projections, affect the DPC reconstruction extremely.

To further reduce the effect of the artifacts, the weights are modified by

$$w^* = \begin{cases} w & \text{for } w > 0.5 \\ 0 & \text{for } w \leq 0.5 \end{cases}, \quad (5.15)$$

meaning pixels with weights below 0.5 are not considered in the reconstruction.

The resulting reconstruction (D) shows even further reduced but still not completely removed artifacts, which suggests that even better correction and weighting schemes are needed, which could be subject of further research.

These results show the possibility to successfully reconstruct the map of the refractive index decrement – i.e. perform phase-contrast CT – by just using two arbitrary phase steps that are approximately half a grating period apart.

The main advantage is that the acquisition of only two phase steps limits the radiation dose to the sample. Also, a continuous rotation of the gantry is theoretically possible as described in the original publication (Zhu et al., 2010). However, on average only half the pixels really contribute to the image formation. This will lead to higher noise levels in the reconstructed images. A uniform flatfield, where the correct steps can be recorded a priori will still yield superior results in this regard.

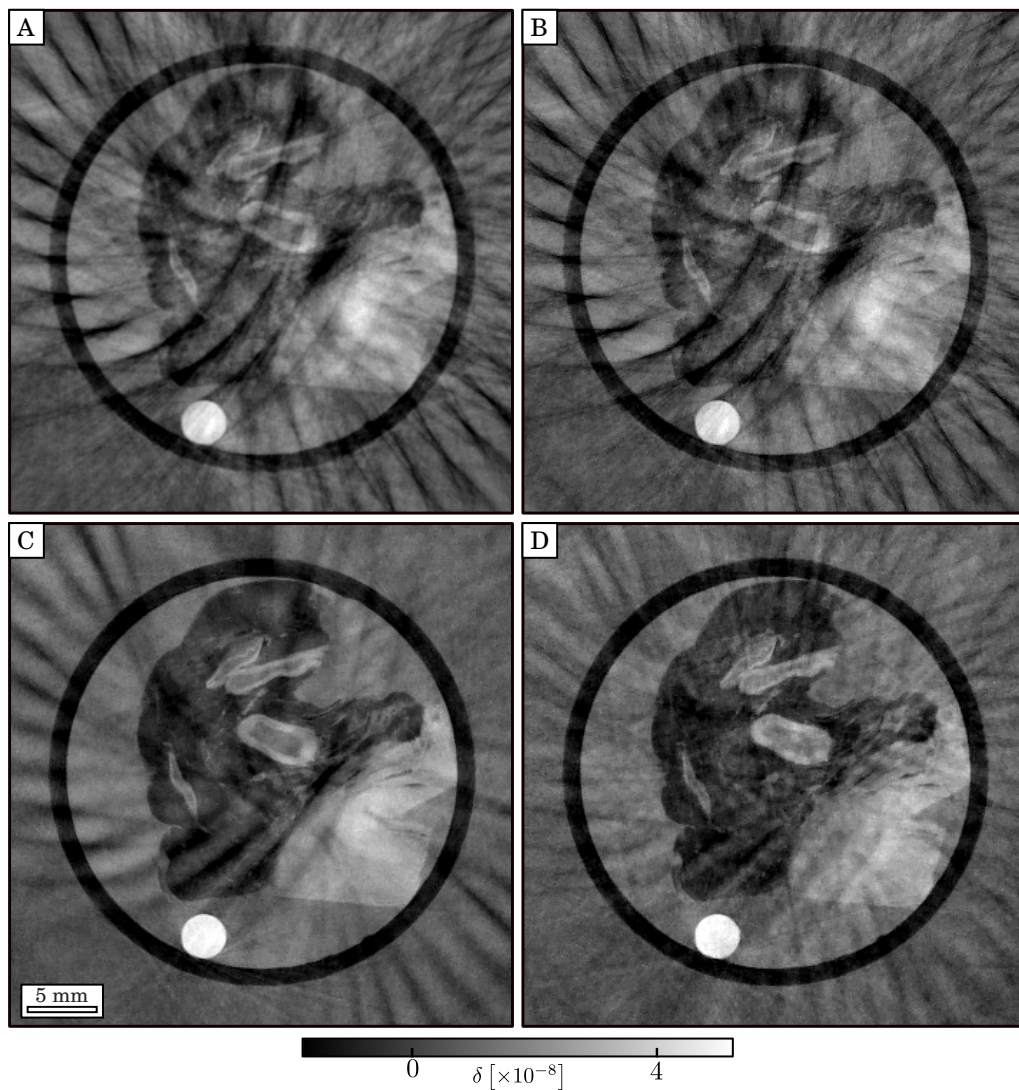


**Fig. 5.12 | Iterative tomographic reconstruction with and without projection weights.** A straight-forward reconstruction using FBP yields an artifact-ridden reconstruction (A). The result does not improve using iterative reconstruction without weights (B), since no additional information is available. Adding the proposed projection weights (Eq. (5.14)) to the statistical iterative reconstruction (SIR) leads to a much better result (C) with less artifacts. Applying the improved weights (Eq. (5.15)) to SIR suppresses the artifacts even further, boosting image quality.

## 5.4 Discussion

In this chapter, we have shown an improved performance of the RP method compared to the conventional PS method in low-dose applications. This improved performance essentially stems from the use of prior knowledge in the phase retrieval: the dynamic range is artificially limited compared to the conventional approach, which can be justified by the prevalence of small values in a differential signal.

Evidently, there are limitations to this method. First, the phase retrieval is based on an approximation that is only correct for small values of the phase shift. On the one hand, most of the values typically are small due to the differential nature of the phase-contrast signal. On the other hand, the influence of large values is disproportionately high due to the integration during the filter step of the tomographic reconstruction. Secondly, only the attenuation and the phase-contrast signal can be obtained. The dark-field signal is not only inaccessible but even leads to wrongly determined phase shift values.

In our experiments, we show that the differential phase-contrast is small and the dark-field signal can be neglected for samples of biological soft-tissue at our setup. Our reconstructions yield correct quantitative values for the RP method.

One could also imagine extensions to this method that could make the method applicable to a wider range of samples. Among them is the possibility of employing a third phase step to quantify the dark-field signal (Pelliccia et al., 2013), although the noise properties of this method have yet to be explored.

Additionally, the straight forward experimental application of the method is limited to cases where the reference phase is uniform over the whole field of view. Only then, the necessary phase-steps can be obtained by recording only two projections. This is the case since meaningful phase-retrieval with two steps is not possible when the steps lie around the tuning points of the phase-stepping curve. However, a uniform reference phase was not available for our experiment. This is a result of grating imperfections which could be solved by future, more uniform gratings from improved fabrication processes.

Therefore, we record more than the two theoretically necessary phase steps and then retrospectively select the appropriate steps for each pixel separately. A step close to the optimal point for phase retrieval is available for each pixel with the 11 phase steps that are recorded in our experiment. Thus, the RP method could be applied despite this experimental limitation.

Note that even in cases where more than two phase-steps are recorded it can still be beneficial to apply the RP method to two appropriate steps and to discard the

remaining ones. This is the case since conventional phase-retrieval fails to extract any meaningful information in the low-SNR case. An example of this phenomenon is displayed in Fig. 5.10, where five phase steps are used for the conventional phase retrieval. Using two of these phase steps for the RP method still delivers superior results.

However, recording additional – i.e. more than two – phase steps is not time- and dose-efficient. Therefore, we enhance the RP approach by combining it with a statistical iterative reconstruction. There, pixels can be assigned weights that determine their influence on the reconstruction. That makes it possible to exclude regions of the projections where phase-retrieval is unfeasible. The reference phase can be used to calculate these projection weights.

We demonstrate successful reconstructions with two globally fixed steps and non-uniform reference phases. However, there is still room for improvement to further reduce artifacts and optimize image quality. In conclusion, we show that the enhanced RP method is compatible with most Talbot-Lau interferometers and could even be applied in pre-clinical imaging systems.

In general, iterative reconstruction can be used to significantly increase the image quality of tomographic imaging. However, it is important to note that conventional iterative reconstruction algorithms work on the already retrieved projections. If a wrong phase is retrieved – e.g. in the PS approach due to statistical phase wrapping – the iterative reconstruction’s ability to improve the image quality will be hindered. It cannot correct for the influence of ”wrong pixels” because there is no way to know which pixels are affected.

In the RP approach however, where the phase is determined correctly and only affected by Gaussian noise, the SIR scheme is more successful in improving the image quality of the reconstructions.

Lately, intensity-based iterative reconstruction schemes for differential phase contrast data have been introduced (Ritter et al., 2016; Brendel et al., 2016; Teuffenbach et al., 2017; Xu et al., 2022). There, the reconstruction is done directly from the measured intensities. This means that the intermediate step of phase retrieval is directly incorporated into the tomographic reconstruction. In this case, the prior knowledge of small differential phase shifts has to be incorporated in a different way – e.g. via regularization. Whether these methods can achieve meaningful phase retrieval at low photon counts has yet to be shown.

## 5.5 Conclusion

Up until now, it has been assumed that the potential for dose reduction in phase-contrast CT is limited compared to attenuation CT. This is one obstacle that stands in the way of more mainstream or even clinical application of phase-contrast CT. This claim is mainly based on the work of Raupach and Flohr (2011), where a low-dose limit for phase-contrast CT is derived. However, only the phase-stepping approach for phase retrieval is considered in their work. As we have shown here, a phase-stepping approach is not the optimal choice for scans with low mean photon counts, since statistical phase wrapping leads to adverse effects on image quality. As a possible alternative, we have examined the reverse projection method and have illustrated that it yields quantitatively and visually satisfactory results for phase-contrast CT scans of biological soft-tissue. More importantly, our results also show that this novel method can extract the differential phase correctly where phase retrieval via phase stepping fails due to statistical phase wrapping. We also demonstrate a way to overcome a major experimental obstacle of this method, thereby making it more widely applicable. Overall, we imagine that based on the results of this study further phase-retrieval and reconstruction schemes can be developed that are optimized for low-dose applications.

# CHAPTER 6

## Two-shot X-ray dark-field imaging

### Short summary

In this chapter, we report on a novel acquisition scheme for time- and dose-saving retrieval of dark-field data in grating-based phase-contrast imaging. In analogy to the approach presented in Chapter 5, the proposed approach only requires two phase steps. This method is capable of accurately retrieving the dark-field signal in the case of very low photon statistics, where conventional approaches introduce bias. Again, we successfully extend the two-shot approach to tomographic investigations by implementing an iterative reconstruction with appropriate weights. Our results indicate an important progression towards the clinical feasibility of dark-field tomography. Most of the results, figures, and text presented in this chapter have been published in *Two-shot X-ray dark-field imaging* (Marschner et al., 2016a).

### 6.1 Introduction

Considering a potential future clinical or on-line implementation of dark-field imaging, strict requirements with respect to low radiation doses and/or short acquisition times have to be satisfied. However, dose reduction in dark-field imaging could prove difficult: as shown in Chapter 2 the dark-field signal cannot be retrieved correctly in the limit of low photon numbers when using the conventional signal extraction scheme, a phase-stepping procedure and subsequent Fourier analysis or least-squares fitting.

### 6.2 Two-shot dark-field imaging

In this chapter, we investigate a different approach to extract the dark-field and attenuation signals in grating interferometry using only two phase steps (Li et al., 2016). This technique was inspired by similar approaches for analyzer-based imaging (Rigon et al., 2003). Both grating interferometry and analyzer-based imaging are sensitive to the same physical quantities and thus share parallels in some aspects of measurement and signal extraction (Pelliccia et al., 2013; Bao et al., 2015).

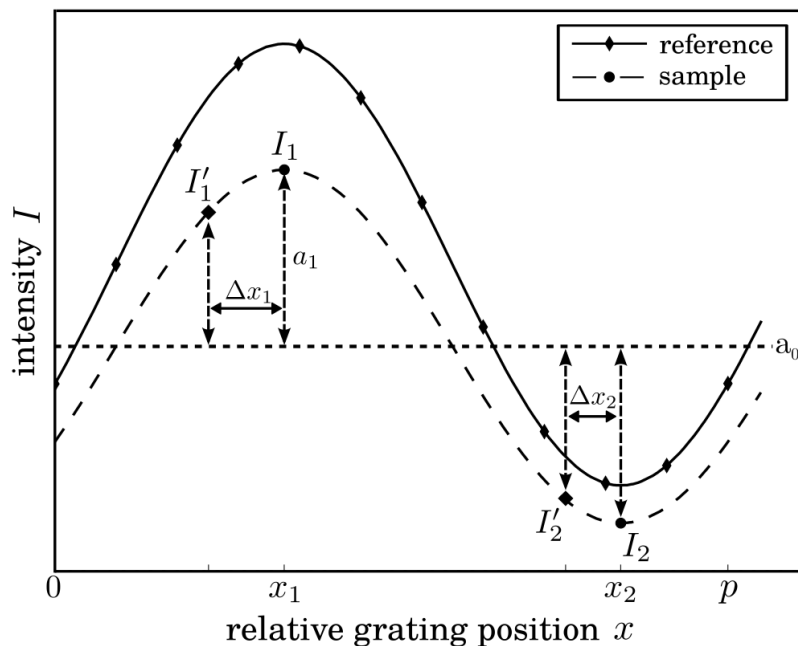


**Fig. 6.1 | Principle of the two-shot dark-field acquisition scheme.** The reference stepping curve is recorded with high statistics and a sufficient number of phase steps. The dark-field signal is directly retrieved from the two measured intensities  $I_{1,2}$ , rather than by performing a fitting procedure. Figure adapted from (Marschner et al., 2016a).

Technically, this "two-shot" method can only accurately retrieve the dark-field signal in pixels that do not show differential phase-contrast signal. However, the accompanied error is minor for small *differential* phase-shifts which is often satisfied for biological samples in typical Talbot-Lau interferometers (cf. subsection 5.3.2).

For samples imposing no differential phase-shifts  $\Delta\phi$ , the phase-stepping curve has extrema at  $x_g/p_t = 0$  and  $1/2$ . At these working points, the measured intensity is only changed slightly by a phase shift. Instead, it is influenced most strongly by a change in the visibility – i.e. the dark-field signal. The corresponding grating positions are from here on called  $x_1$  and  $x_2$ .

A Taylor expansion of the phase stepping curve at the working points  $x_{1,2}$  is

$$I(x_{1,2}) = a_0 \pm a_1 \mp a_1 \frac{\Delta\phi^2}{2} + \dots \quad (6.1)$$

We assume small phase shifts  $\Delta\phi \approx 0$ . Therefore, we only consider the first order of the expansion. Thus, the mean and the amplitude of the fitted cosine can be extracted from these two measured intensities by addition

$$a_0 = \frac{1}{2} (I(x_1) + I(x_2)) \quad (6.2)$$

or subtraction

$$a_1 = \frac{1}{2} (I(x_1) - I(x_2)) , \quad (6.3)$$

respectively.

Correspondingly, the visibility reduction caused by the sample is given by

$$V = \frac{a_1}{a_0} = \frac{I(x_1) - I(x_2)}{I(x_1) + I(x_2)} . \quad (6.4)$$

The major advantage of our method is the fact that no retrieval of the phase-stepping coefficients through Fourier analysis is required. Thus the dark-field values are expected to be free from estimation bias Section 2.3.3. This would make correct retrieval of the dark-field signal possible even for very short exposure times – i.e. low dose.

In current experimental setups, the differential phase of the reference scan is not uniform over the field of view. This is because of grating imperfections and beam divergence. This implies that sampling the stepping curve at the two extrema for each pixel is not feasible by only recording two images. If the stepping curve is not sampled exactly at its minimum and maximum, but at offsets  $\Delta x_1$  and  $\Delta x_2$  from these points, the intensities  $I'_1$  and  $I'_2$  will be measured (cf. Fig. 6.1).

In this case, additional corrections have to be applied to extract the correct visibility and attenuation signal. The extracted coefficients are denoted as  $a'_0$  and  $a'_1$ . The correction factors derived below can be used to relate the measured coefficients  $a'_{0,1}$  to the correct coefficients  $a_0$  and  $a_1$ .

The first extracted Fourier coefficient is related to the correct one by

$$\begin{aligned} a'_1 &= \frac{1}{2} (I'_1 - I'_2) \\ &= \frac{1}{2} \{ [a_0 + a_1 \cos(2\pi\Delta x_1)] - [a_0 - a_1 \cos(2\pi\Delta x_2)] \} \\ &= \frac{a_1}{2} [\cos(2\pi\Delta x_1) + \cos(2\pi\Delta x_2)] \\ &\equiv a_1 c_1. \end{aligned} \quad (6.5)$$

The extracted and the correct zeroth Fourier coefficients are related as follows

$$\begin{aligned} a'_0 &= \frac{1}{2} (I'_1 + I'_2) \\ &= \frac{1}{2} \{ [a_0 + a_1 \cos(2\pi\Delta x_1)] + [a_0 - a_1 \cos(2\pi\Delta x_2)] \} \\ &= a_0 + \frac{a_1}{2} [\cos(2\pi\Delta x_1) - \cos(2\pi\Delta x_2)] \\ &\equiv a_0 + c_0. \end{aligned} \quad (6.6)$$

Consequently, in order to obtain the corrected values the measured values  $a'_0$  and  $a'_1$  have to be corrected using the factors

$$c_0 = \frac{a_1}{2} \left[ \cos \left( 2\pi \frac{\Delta x_1}{p} \right) - \cos \left( 2\pi \frac{\Delta x_2}{p} \right) \right] \quad (6.7)$$

and

$$c_1 = \frac{1}{2} \left[ \cos \left( 2\pi \frac{\Delta x_1}{p} \right) + \cos \left( 2\pi \frac{\Delta x_2}{p} \right) \right], \quad (6.8)$$

respectively.

## 6.3 Experimental results

In the following, the performance of the two-shot dark-field acquisition and the conventional dark-field retrieval technique are compared on experimental data. The Talbot-Lau interferometer used for this measurement is described in Chapter 3. Two changes to the experimental setup are made in comparison to the previous measurements. The sample is moved closer to the source by 60 cm and thereby farther away from the phase grating. This reduces the sensitivity of the setup and is necessary due to the strongly scattering sample. Also, the sample was not submerged in a water bath.

### 6.3.1 Radiography of a scattering sample

We measured a sample made of layers of common printer paper using a range of different exposure times. The average visibility in the reference projections is 30.3%. The phase-stepping procedure is used to obtain phase-stepping curves with 11 phase steps. The exposure time per phase step ranges from 0.1 ms to 26.2 s. In a sample-free area, this equates to around 0.5 to 120000 photons per pixel or *counts*.

A weighted least-squares fit (cf. Section 3.2.2) is used to obtain the three image signals. Additionally, the novel two-shot method is used to obtain the attenuation and the dark-field signal. For this analysis, the reference scan is used to select the two steps closest to the extrema of the stepping curve for each pixel separately. The reason for this procedure is the aforementioned non-uniformity of the reference phase. In addition, Eqs. (6.7) and (6.8) are used to correct the retrieved values.

The results of the experiment are displayed in Fig. 6.2. The scan with the highest statistics – i.e. longest exposure time – is shown in the left column. The transmission and dark-field images that are retrieved using the phase-stepping procedure with subsequent least-squares fitting are shown in the top rows. In the high statistics scan, the five different areas of the sample show distinct values of the dark-field signal. In the

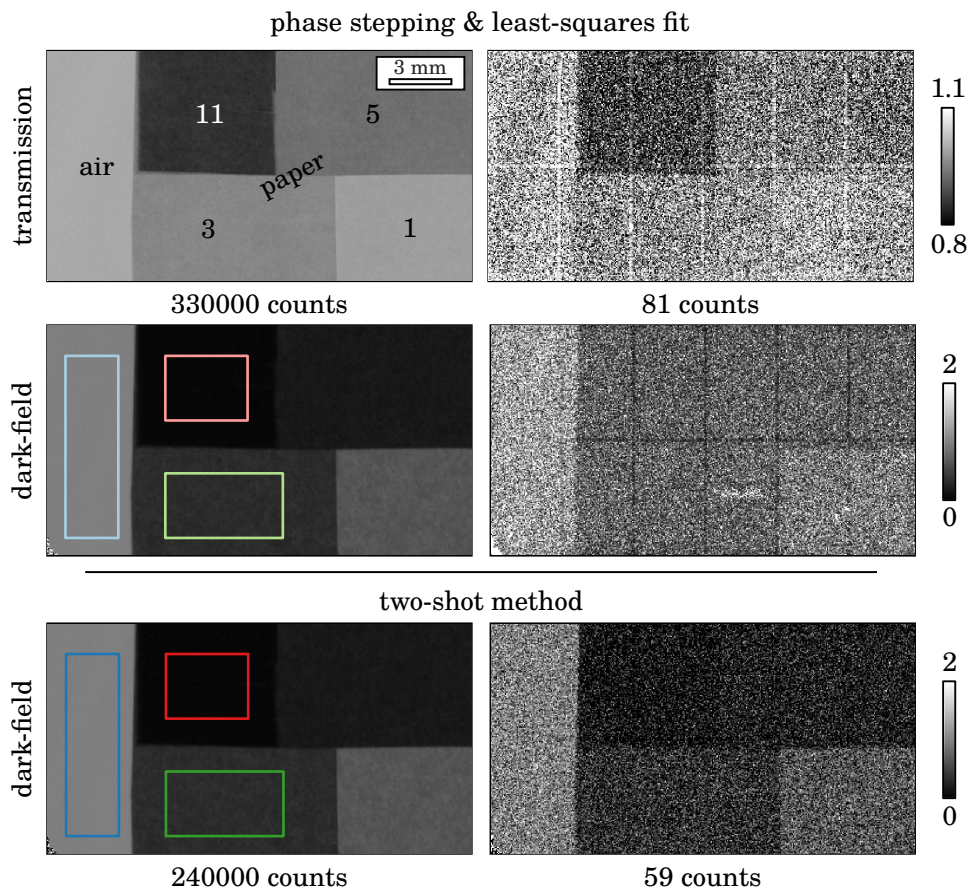


**Fig. 6.2 | Radiography of a scattering sample.** Transmission and dark-field projections of air and stacks of paper (number of layers: 1, 3, 5, and 11) with high and low SNR obtained using the conventional and the novel two-shot method. Using the phase-stepping approach, the dark-field values rise in all areas of the sample when the exposure time is decreased. In comparison, when using the two-shot method the correct values are maintained even for low statistics. The mean count numbers refer to the number of photons per pixel and were measured in a sample free area. Figure adapted from Marschner et al. (2016a).

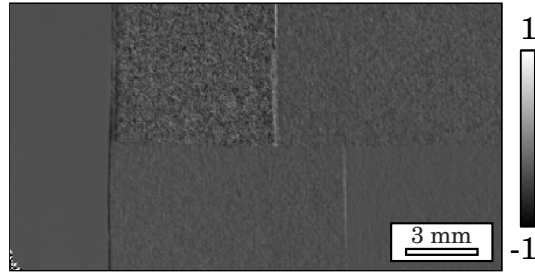


**Fig. 6.3 | Differential phase-contrast projection of the paper sample.** The projection was obtained using the phase-stepping approach with subsequent least-squares fitting and an exposure time of 26.2s. The area where the most sheets of paper are stacked shows the highest noise level. This is a result of reduced visibility due to scattering. The mean value of the differential is close to zero for all areas. Figure adapted from Marschner et al. (2016a).

low statistics scan, however, the retrieved dark-field signals are higher than the values measured previously. Further, the dark-field signals in the areas of 11, 5 and 3 sheets of paper are of similar value, rendering a distinction of the different material thickness impossible.

The dark-field projections that are obtained with the proposed two-shot method are shown in the bottom row. Here, the average dark-field signal does not deviate from the correct value when the exposure time is decreased. The corresponding differential phase-contrast projection is shown in Fig. 6.3. Even though paper is refracting and scattering, the values of the *differential* phase-contrast signal feature a small amplitude. This is an important prerequisite for the applicability of the two-shot dark-field acquisition technique. In the area in the middle of the top part of the projection (11 sheets of paper, cf. Fig. 6.1), the differential phase-contrast signal shows higher image noise. This is a result of the decreased visibility due to scattering – i.e. dark-field signal – in this region.

The mean dark-field values for three regions of interest in the sample are visualized in dependence on exposure time, respectively noise level, in Fig. 6.4. Again, it can clearly be seen that the retrieved dark-field signal deviates from the correct mean for the conventional signal extraction method. In contrast, the proposed method is able to correctly retrieve the dark-field signal even for scans with very high noise levels.

### 6.3.2 Radiography of a strongly absorbing, non-scattering sample

We also successfully apply the two-shot method to a highly absorbing sample. We measure a sample consisting of aluminum blocks with a thickness of 1.95 mm, 4.95 mm and 8.95 mm and exposure times ranging from 0.1 ms to 26.2 s at close to 5000 photons

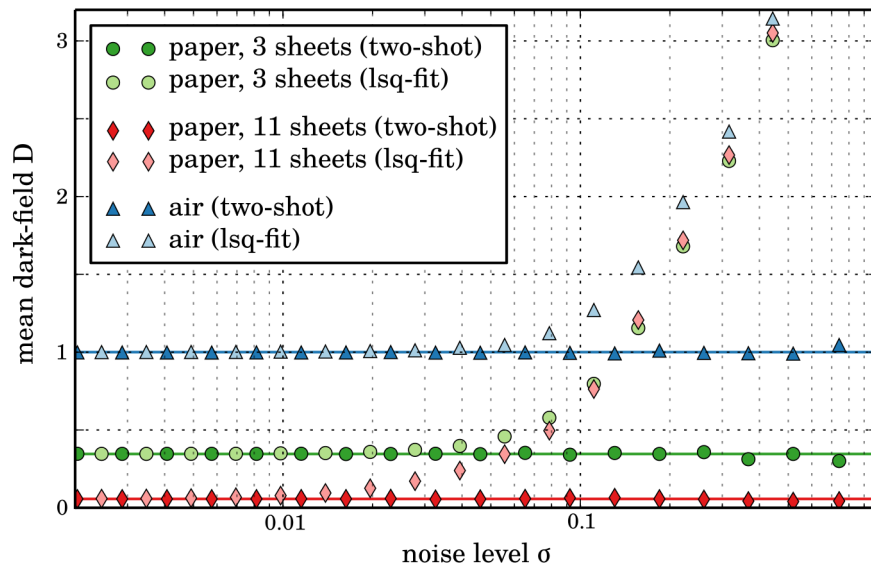


**Fig. 6.4 | Mean dark-field values at varying noise levels.** Dependency of the measured mean dark-field values on the noise levels in the attenuation channel for the three ROIs marked in Fig. 6.2. In the case of least-squares fitting (lsq-fit), which is the conventional signal extraction method, the measured values deviate from the correct values for high noise levels. This indicates a failure of signal retrieval. In contrast, using the novel two-shot approach the image results remain still consistent for highly increased noise levels. Figure adapted from Marschner et al. (2016a).

per second per pixel in a sample-free area.

Generally, the dark-field image arises from (ultra) small-angle scattering at microstructures of the investigated material. However it may also be related to so-called visibility hardening. Here, the absorption of low energy photons leads to a change in overall visibility (Hipp et al., 2014; Chabior et al., 2011; De Marco et al., 2024). This is due to the fact that the visibility is energy-dependent. To compensate for this effect, the dark-field signal of all materials is normalized to unity using the appropriate values from the high statistics scans.

The results of the experiment are displayed in Fig. 6.5. The scan with the highest statistics – i.e. longest exposure time – is shown in the left column. The transmission and dark-field images that are retrieved using the phase-stepping procedure with subsequent least-squares fitting are shown in the top rows. The average transmission in the indicated regions of interest is unity for air and 0.08 for 8.95 mm of aluminum in all scans.

In the high statistics scan, the dark-field signal is unity for all four uniform parts of the sample after correction for visibility hardening. In the low statistics scan, the retrieved dark-field signal is higher than unity for all material thicknesses. This is most strongly visible in the region of the thickest aluminum plate since this effect depends

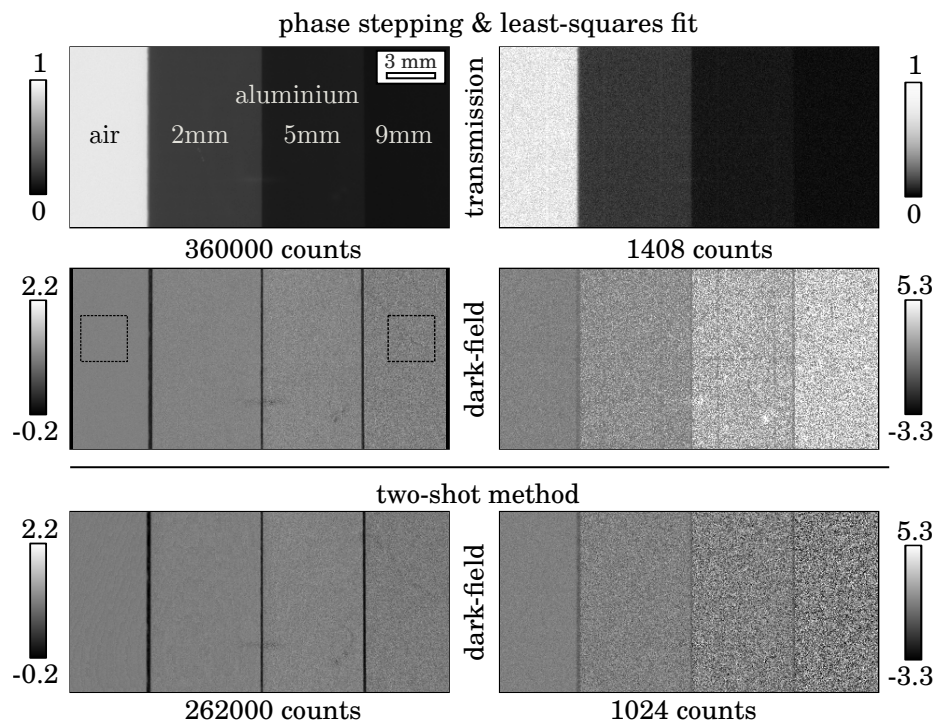


**Fig. 6.5 | Transmission and dark-field projections of air and aluminum.** The high and low SNR projections of air and aluminum (thickness 1.95 mm, 4.95 mm and 8.95 mm) are obtained using the conventional and the novel two-shot method. Visibility hardening is corrected for which results in a mean dark-field of unity for all materials in the high-SNR scan. Regions with lower transmission exhibit a dark-field signal exceeding the correct value of unity with decreasing exposure time using the phase-stepping approach. In comparison, when using the two-shot method the correct value is maintained even for low statistics. The dark-field images are scaled from  $[0 - 2\sigma, 2 + 2\sigma]$ , with  $\sigma$  being the standard deviation in a region of interest in the dark-field projection of 8.95 mm aluminum. Figure adapted from Marschner et al. (2016a).

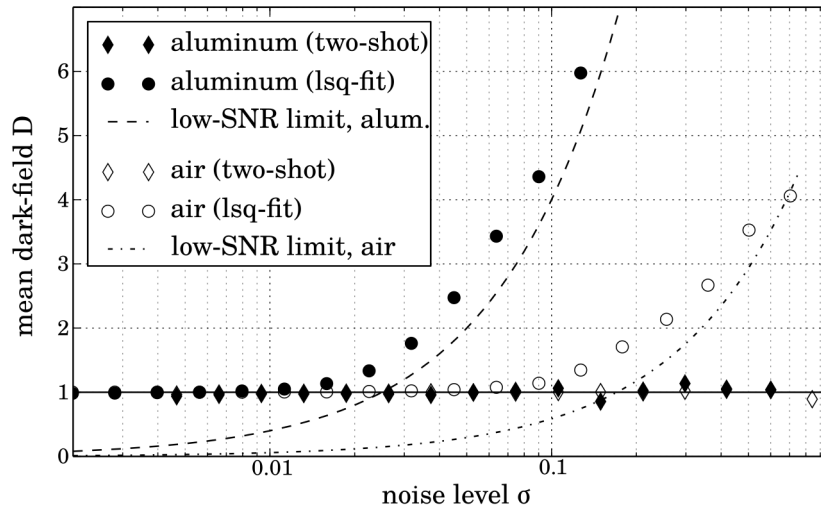


**Fig. 6.6 | Mean dark-field signal at varying noise levels.** Dependency of the measured mean dark-field values on the noise levels in the attenuation channel for two materials with vastly differing attenuation properties. In the case of least-squares fitting, which is the conventional signal extraction method, the measured values deviate from the expected value of unity for high noise levels. This indicates a failure of signal retrieval. Using the novel two-shot approach, the image results remain still consistent for highly increased noise levels. The mean values are measured in the regions of interest as displayed in Fig. 6.5. Figure adapted from Marschner et al. (2016a).

on the attenuation of the sample. The dark-field projections that are obtained with the proposed two-shot method are shown in the bottom row. Here, the average dark-field signal does not deviate from the correct value when the exposure time is decreased.

The mean dark-field values for air and aluminum in dependence on exposure time, respectively noise level, are visualized in Fig. 6.6. Again, it can clearly be seen that the retrieved dark-field signal deviates from the correct mean for the conventional signal extraction method. In contrast, the proposed method is able to correctly retrieve the dark-field signal even for scans with very high noise levels.

### 6.3.3 Tomographic two-shot dark-field imaging

Unlike in radiographic applications where only a few exposures are taken, the applied radiation dose has to be split up between many exposures in tomographic imaging. Thus, the aforementioned problem of failing signal retrieval is of particular relevance there.

In the following, we will demonstrate experimentally that the two-shot method is also applicable to tomographic imaging. A foam ear plug with a diameter of roughly 10 mm is measured in a tomographic scan with 2400 projections, each comprising 11 phase steps. Additionally, a reference projection is recorded every 15 projections. To



**Fig. 6.7 | Foam ear plug.** Photo of the foam ear plug that is used as a weakly-absorbing but strongly-scattering sample.

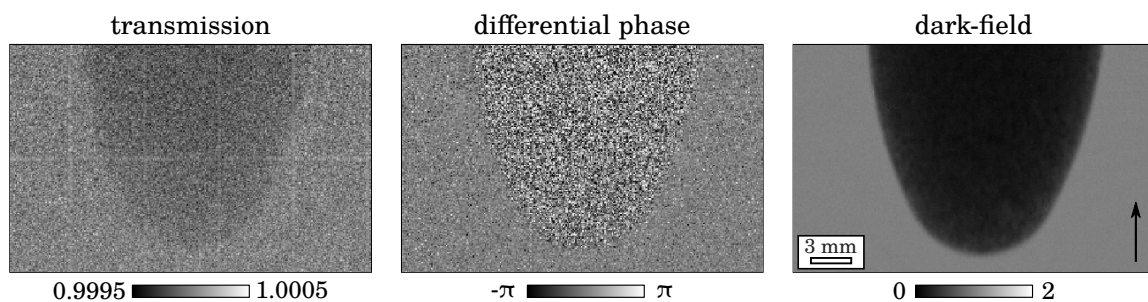


**Fig. 6.8 | Projection images of the foam earplug.** Transmission, differential phase-contrast and dark-field projections of the foam ear plug. The attenuation of the sample is very weak. This leads to transmission values close to unity. The sample has a very noisy differential phase-contrast signal, because of its strong scattering – dark-field – signal. The arrow marks the rotation axis of the tomographic measurement. Figure adapted from Marschner et al. (2016a).

avoid ring artifacts, the sample is shifted randomly in the range of 10 pixels in x- and y-direction after each projection. Fig. 6.7 shows a photography of the sample. This sample is selected since it is weakly absorbing but strongly scattering.

Exemplary transmission and differential phase-contrast projections of this sample are shown in Fig. 6.8. The transmission of the sample is close to unity due to its weak absorption properties. The sample’s differential phase-contrast signal is centered around zero and shows substantial image noise. This is due to the fact that the corresponding dark-field signal is very strong which leads to high image noise in the differential phase-contrast projections (cf. Section 2.3). The number of photons per pixel are around 96,800 for this high statistics scan which corresponds to a total exposure time of 33 s – i.e. 3 s per phase step. The average flux at one detector pixel is roughly 2933 photons per second.

The SIR algorithm is used to reconstruct maps of the linear attenuation coefficient and the linear diffusion coefficient (cf. Section 2.4.2). We assume a Gaussian distribution for the dark-field signal for both the two-shot and the least-squares method. This assumption is incorporated into the data model of the SIR.

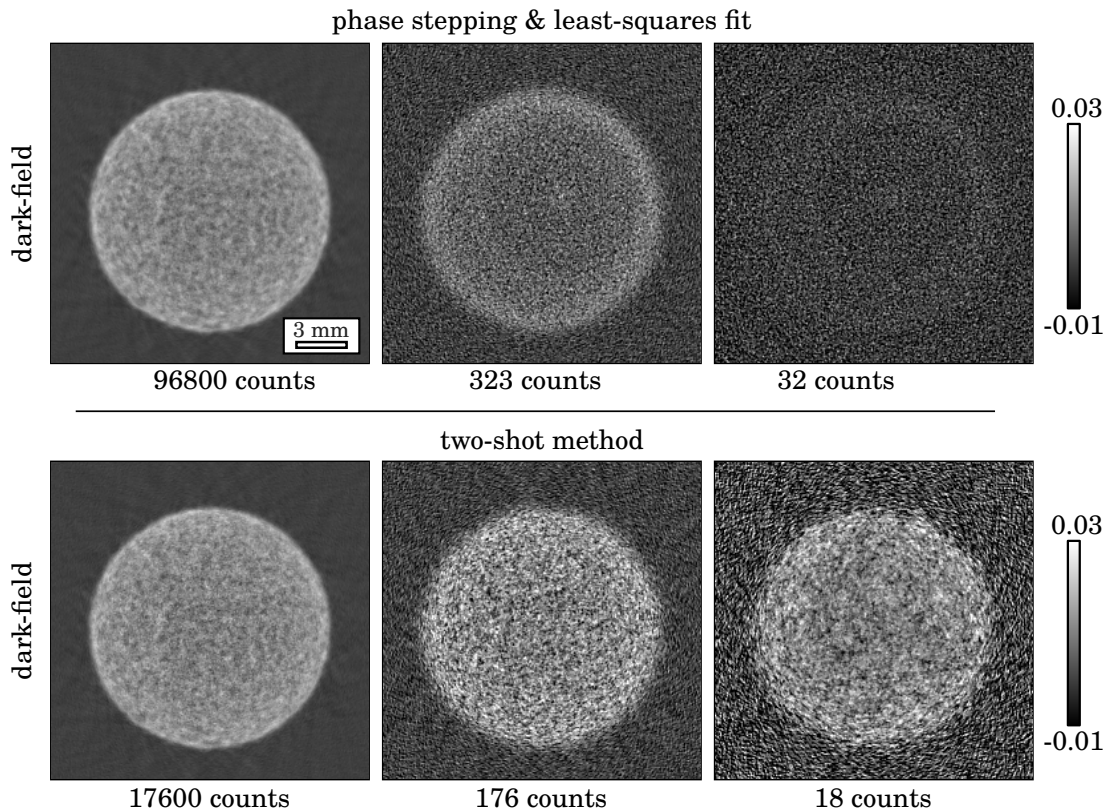


**Fig. 6.9 | Reconstruction of the foam earplug.** Axial slices of the reconstructed dark-field tomography of a foam earplug. The count numbers correspond to one projection and pixel. The reconstructions of the phase-stepping projections show a vanishing signal for scans with low counts. In contrast, the two-shot method is able to visualize the sample even in low-SNR scenarios. Figure adapted from Marschner et al. (2016a).

A Huber potential function is used for regularization. For better comparability, the regularization strength is chosen to be rather weak and kept constant for all reconstructions.

The results of the tomographic reconstruction are displayed in Fig. 6.9. The inner structure of the foam plug is clearly visible in the high-SNR reconstructions of both techniques and their quantitative values are comparable. However, the two methods respond differently to a decrease in exposure time. In the phase-stepping approach, the signal of the ear plug starts to vanish already at counts of around 300 photons per pixel and projection which corresponds to an exposure time of around 0.1 s.

When further reducing the number of counts, the ear plug is no longer distinguishable from the background. This can be explained by similar noise levels in all areas of the projection as the foam sample is barely absorbing (see Fig. 6.8). Since the extracted dark-field signal is only dependent on the noise level in the low-SNR case, the projections and hence the reconstructions do not contain any information about the true dark-field signal of the sample any more.

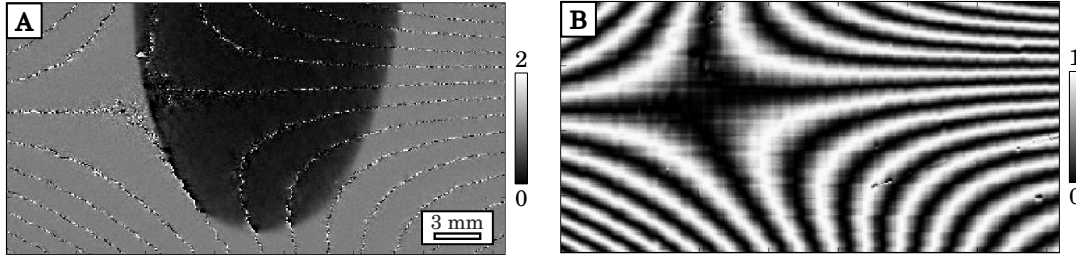


**Fig. 6.10 | Results of two-shot dark-field tomography with globally fixed steps.** Panel (A) on the left shows a two-shot dark-field projection where the areas of unsuccessful signal extraction can be clearly seen. These areas follow a pattern similar to the flatfield phase-contrast signal. The flatfield DPC signal can be used to calculate weights for a tomographic reconstruction, as shown in panel (B). Areas where signal retrieval failed have weights close to zero and will therefore contribute less to the iterative reconstruction. Figure adapted from Marschner et al. (2016a).

In contrast, the signal does not vanish in the reconstructions of the two-shot method when reducing the exposure time. The sample is still visible in the scan with the shortest exposure time of 6 ms which corresponds to only 18 photons per pixel and projection. Even though the noise level is increased significantly, it is still possible to distinguish a difference in signal intensity between the inner and the outer part of the sample.

#### 6.3.4 Dose-optimized tomography using projection weights

Up to this point, we always recorded a complete phase-stepping dataset and retrospectively selected the two optimal phase steps for each pixel separately. We then use these steps for signal extraction in the two-shot method. Consequently, the total required dose for imaging is significantly higher than needed, since a majority of the acquired phase steps is not used. Clearly, this is not the optimal procedure although we have shown that it still can be useful to extract the dark-field signal in cases where the conventional retrieval algorithms fail.

In the following, we propose a dose optimized variant of the aforementioned approach, where only a total of two phase steps are recorded. These are placed roughly half a grating period apart. Using Eqs. (6.7) and (6.8), accurate retrieval of the dark-field signal is possible with these two phase steps. However, the retrieved values will be dominated by noise in pixels where the two measured points lie too close to the zero crossings of the phase-stepping curve.

This time, we re-evaluate the data from the tomographic experiment described previously without selecting the optimal phase steps for each pixel separately. Instead, we globally select the 1<sup>st</sup> and 6<sup>th</sup> step of the 11 phase steps that are recorded – i.e. the same phase steps for each pixel. The method is first demonstrated for the scan with

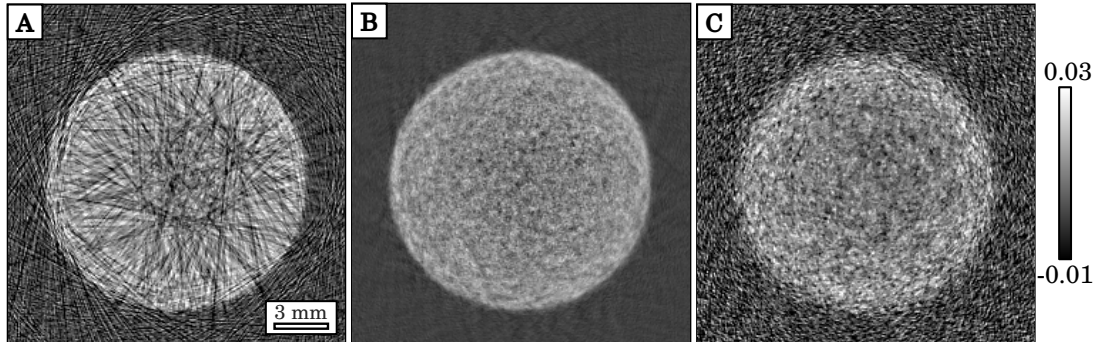


**Fig. 6.11 | Results of two-shot dark-field tomography with globally fixed steps.** The first panel (A) shows a reconstruction without weights featuring severe artifacts that arise out of the pixels where signal retrieval failed. Panel (B) displays an artifact-free reconstruction of the same projections using the weights shown above. A successful reconstruction of low-SNR scan (59 counts) using weights can be seen in the last panel (C). Figure adapted from Marschner et al. (2016a).

the highest statistics with an exposure time of 3 seconds per phase step – i.e. 6 seconds per projection. It can be seen from the dark-field projection shown in Fig. 6.10(A) that the signal retrieval works well for most pixels. Note that the pixels for which the signal extraction fail form a pattern that matches the shape of the phase in the reference scan.

The reference phase can change over the course of a long scan due to setup instabilities and temperature changes. These changes introduce artifacts in conventional phase-stepping acquisitions. This is why reference projections or *flatfields* are recorded in a regular interval between projections. The reference projection recorded closest in time to the sample projection is used for a reference correction to achieve artifact free images. We use the same reference projections to calculate the projection weights for the two-shot dark-field method. No additional reference projections have to be recorded compared to a conventional phase-stepping acquisition.

The reconstructions of these two-shot dark-field projections are shown in Fig. 6.11(A). The noisy pixels present in the projection result in severe artifacts in the reconstructed slice. However, the overall shape and the quantitative values match the reconstructed slice of the phase-stepping projections shown in Fig. 6.9.

With the goal of mitigating the reconstruction artifacts, the iterative reconstruction was combined with pixel-wise weights. These weights contain information about the accuracy of the two-shot retrieval in each pixel which depends on the reference phase of each pixel. In particular, the weights are set as the square of the correction factor  $c_1$ , cf. Eq. (6.8).

The weights determined from the projection shown in Fig. 6.10(A) are presented in

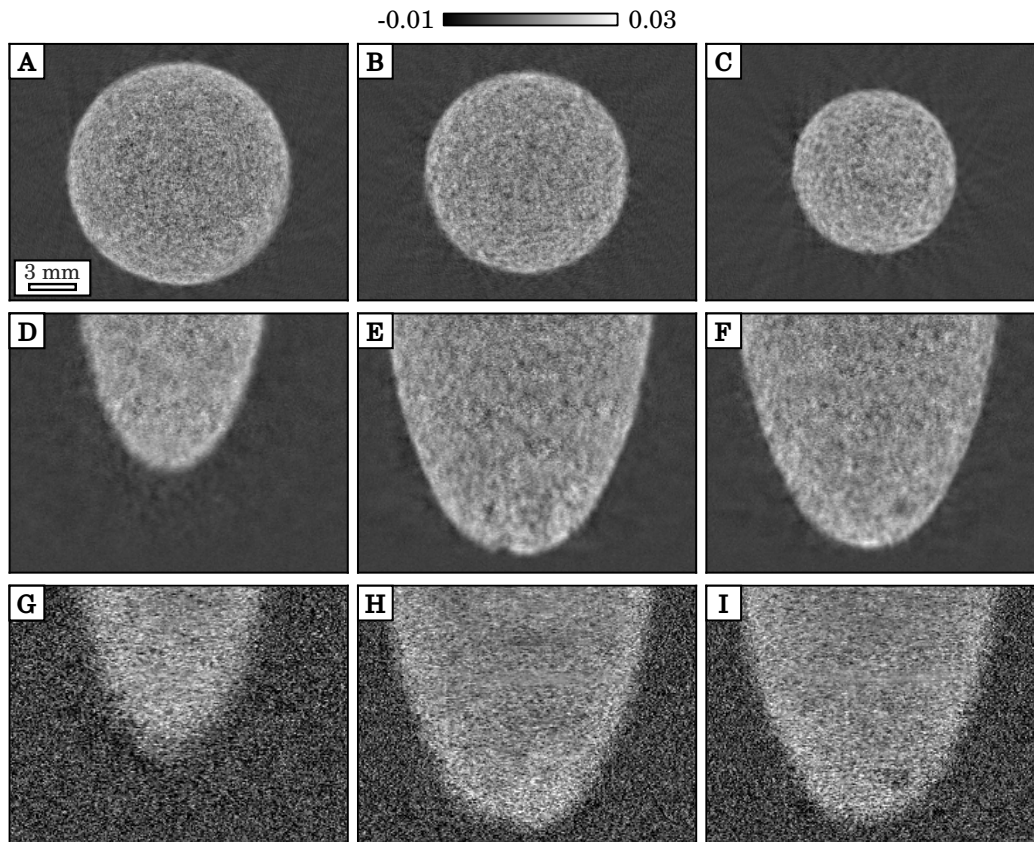


**Fig. 6.12 | Additional slices of the two-shot dark-field tomography with globally fixed steps.** The top two rows (A-F) show the high statistics scan that was previously displayed in Fig. 6.11(B). The bottom row shows the low statistics scan (59 photons per pixel and projection) of Fig. 6.11(C). All slices through the volumes are 50 pixels apart. The slices are in axial (A-C) and coronal (D-I) direction. The image quality is consistent in all slices, which illustrates the effectiveness of the weighted reconstruction scheme. Figure adapted from Marschner et al. (2016a).

Fig. 6.10(B). The regions where the weights have the lowest values correspond to the regions where the signal retrieval fails. These weights are used for a reconstruction using the SIR algorithm with the same parameters as described earlier. The result of this reconstruction is shown in Fig. 6.11(B). It is apparent that this reconstruction is far superior compared to the one without weights displayed in Fig. 6.11(A) and comparable to the reconstructions shown in Fig. 6.9.

We also apply this approach to a low-dose scan and a successful reconstruction is shown in Fig. 6.11(C). Finally, the reconstruction benefits from a random translation of the sample between projections, since pixels are moved over both good and poor weights.

The iterative tomographic reconstruction of the two-shot dark-field acquisition with

fixed steps relies on the projection weights. These weights vary considerably throughout the image. Therefore, it is important to inspect the reconstruction quality in the complete 3D-volume. A variety of slices through the volume is displayed in Fig. 6.12. It is evident that the image quality is consistent over the whole field of view.

This scheme delivers better results than the equivalent procedure used for two-shot phase-contrast tomography. This could be due to the fact that the dark-field signal is not differential like the phase-contrast signal. Therefore, the impact of wrongly measured values is not as severe and more localized as the reconstruction does not include an integrating step.

## 6.4 Conclusion

In conclusion, we have demonstrated an alternative procedure to acquire the dark-field signal in X-ray grating-based phase-contrast radiography. We have further shown that it is possible to successfully reconstruct tomographic dark-field scans from only two phase steps by combining the two-shot procedure with an appropriately weighted iterative reconstruction. We have shown that the noise properties of this algorithm are superior to the conventional approach for scans with low photon counts. Thus, it enables the correct retrieval of the dark-field signal even for scans with very low photon counts, where the conventional signal extraction procedure fails. The disadvantages of this method are its inability to simultaneously extract the phase-contrast signal as well as its inapplicability to samples with a strong differential phase shift. Since the current medical investigations of grating-based imaging focus on the dark-field signal (e.g. lung imaging, mammography, kidney stones) we consider this technique a step towards the clinical feasibility of grating-based dark-field imaging.



# CHAPTER 7

## Summary & Outlook

This work addresses some of the – apparently inherent – limitations of grating-based phase-contrast and dark-field CT as it is commonly implemented in laboratory setups. It is known that the commonly-used phase-stepping procedure prohibits fast measurements and significant dose reduction. During the course of this work, these limitations were mitigated by developing and implementing new approaches for data acquisition and data analysis.

In particular, in Chapter 4 we introduce the helical fringe-scanning procedure, which allows faster acquisition of phase-contrast and dark-field CT scans. This new measurement procedure combines a helical sample movement with fringe scanning. Thereby, the phase-stepping curves can be obtained without grating movement and spatial interpolation. This enables a continuous rotation of sample or gantry, which is needed to be able to reach the speed of modern CT scanners. Additionally, it relaxes the stability requirements of the setup by forfeiting grating movement. We demonstrate the feasibility of this method and its accompanying analysis method by showing tomographic reconstructions of a phantom obtained at our laboratory setup.

We also circumvent the previously established lower limit of photon counts per pixel where meaningful retrieval of the phase-contrast and dark-field signal was deemed possible. This is achieved by developing and implementing data acquisition and reconstruction approaches that use two phase steps at particular regions of the stepping curve. These two-shot methods, detailed in Chapters 5 and 6, enable more dose-effective tomographic scans with laboratory sources. They come with the drawback of being mutually incompatible in the sense that always only the phase-contrast or dark-field signal can be acquired. An additional phase-step would be needed to acquire the missing signal. We show that these novel methods yield improved image quality and enable quantitative reconstruction at low photon counts. In order to overcome technical shortcomings of the experimental setup, we adopt an iterative reconstruction algorithm using image-based weights. As a result, our acquisition scheme can successfully be used in current laboratory settings.

In conclusion, this work establishes that the conventional phase-stepping procedure is not the optimal approach in all cases. While it is still best suited for reaching high sensitivity in laboratory setups, a helical or two-shot scan can be a more viable

alternative when short scan times and reduced radiation dose are desired.

These insights motivate the development of other optimized processing methods. In the so-called intensity-based statistical iterative reconstruction (IB-SIR) the volumes are reconstructed directly from the measured intensities (Teuffenbach et al., 2017). Skipping the intermediate retrieval of the projections should solve the low-count problems discussed in Chapters 5 and 6. Additionally, a variety of experimental configurations and measurement protocols can be directly reconstructed by this method.

Recently, the helical CT method developed in this thesis was combined with IB-SIR to enable phase-contrast breast CT at clinical dose-levels (Xu et al., 2022; van Gogh et al., 2023), highlighting the potential of this method for clinical imaging.

Additionally, the processing methods and optimization outlined in Chapter 3 were a vital part to achieve high image quality and sensitivity at our laboratory setup. This was the basis for many pre-clinical studies that were carried out during the course of this thesis (Birnbacher et al., 2016, 2023; Braunagel et al., 2017; Grandl et al., 2014; Hellerhoff et al., 2019; Herzen et al., 2019; Hetterich et al., 2014, 2015, 2016, 2017; Mohajerani et al., 2014; Notohamiprodjo et al., 2018; Richter et al., 2017; Willner et al., 2015)

These processing methods and their theoretical foundation were further developed in De Marco et al. (2018) and culminated in the successful implementation of fringe scanning for dark-field radiography on a human scale (Willer et al., 2018; Frank et al., 2022). Integrating a Talbot-Lau interferometer into a clinical CT system posed even more algorithmic challenges that were recently overcome (Viermetz et al., 2022, 2023), highlighting that clinical dark-field CT is within reach.

# Bibliography

- Als-Nielsen, J. and McMorrow, D. *Elements of Modern X-ray Physics*. John Wiley & Sons, 2011. ISBN 9781119970156.
- Arboleda, C., Wang, Z., and Stampanoni, M. Tilted-grating approach for scanning-mode X-ray phase contrast imaging. *Opt. Express*, 22(13):131–137, 2014.
- Bao, Y., Wang, Y., Gao, K., Wang, Z.-L., Zhu, P.-P., and Wu, Z.-Y. Investigation of noise properties in grating-based x-ray phase tomography with reverse projection method. *Chinese Phys. B*, 24(10):108702, 2015.
- Bech, M. *X-ray imaging with a grating interferometer*. PhD thesis, University of Copenhagen, 2009.
- Bech, M., Bunk, O., David, C., Kraft, P., Brönnimann, C., Eikenberry, E. F., and Pfeiffer, F. X-ray imaging with the PILATUS 100k detector. *Appl. Radiat. Isot.*, 66(4):474–8, 2008.
- Bech, M., Bunk, O., Donath, T., Feidenhans'l, R., David, C., and Pfeiffer, F. Quantitative x-ray dark-field computed tomography. *Phys. Med. Biol.*, 55(18):5529–39, 2010.
- Bech, M., Tapfer, A., Velroyen, A., Yaroshenko, A., Pauwels, B., Hostens, J., Bruyn-donckx, P., Sasov, A., and Pfeiffer, F. In-vivo dark-field and phase-contrast x-ray imaging. *Sci. Rep.*, 3:10–12, 2013.
- Berger, M., Hubbell, J., Seltzer, S., Chang, J., Coursey, J., Sukumar, R., Zucker, D., and Olsen, K. XCOM: Photon cross section database (version 1.5)., 2010.
- Bevins, N., Zambelli, J., Li, K., Qi, Z., and Chen, G.-H. Multicontrast x-ray computed tomography imaging using Talbot-Lau interferometry without phase stepping. *Med. Phys.*, 39(1):424, 2012.
- Birnbacher, L., Willner, M., Velroyen, A., Marschner, M., Hipp, A., Meiser, J., Koch, F., Schröter, T., Kunka, D., Mohr, J., Pfeiffer, F., and Herzen, J. Experimental Realisation of High-sensitivity Laboratory X-ray Grating-based Phase-contrast Computed Tomography. *Sci. Rep.*, 6:24022, 2016.
- Birnbacher, L., Viermetz, M., Noichl, W., Allner, S., Fehringer, A., Marschner, M., von Teuffenbach, M., Willner, M., Achterhold, K., Noël, P. B., et al. Tilted grating

- phase-contrast computed tomography using statistical iterative reconstruction. *Sci. Rep.*, 8(1):1–8, 2018.
- Birnbacher, L., Braig, E.-M., Pfeiffer, D., Pfeiffer, F., and Herzen, J. Quantitative x-ray phase contrast computed tomography with grating interferometry. *European Journal of Nuclear Medicine and Molecular Imaging*, 2021.
- Birnbacher, L., Braunagel, M., Willner, M., Marschner, M., De Marco, F., Viermetz, M., Auweter, S., Notohamiprodjo, S., Hellbach, K., Notohamiprodjo, M., Staehler, M., Pfeiffer, D., Reiser, M. F., Pfeiffer, F., and Herzen, J. Quantitative differentiation of minimal-fat angiomyolipomas from renal cell carcinomas using grating-based x-ray phase-contrast computed tomography: An ex vivo study. *PLOS ONE*, 18(4): e0279323, 2023.
- Bonse, U. and Hart, M. An X-ray interferometer. *Appl. Phys. Lett.*, 6(1965):155–156, 1965.
- Braunagel, M., Birnbacher, L., Willner, M., Marschner, M., De Marco, F., Viermetz, M., Notohamiprodjo, S., Hellbach, K., Auweter, S., Link, V., Woischke, C., Reiser, M. F., Pfeiffer, F., Notohamiprodjo, M., and Herzen, J. Qualitative and quantitative imaging evaluation of renal cell carcinoma subtypes with grating-based x-ray phase-contrast ct. *Scientific Reports*, 7:45400, 2017.
- Bravin, A., Coan, P., and Suortti, P. X-ray phase-contrast imaging: from pre-clinical applications towards clinics. *Phys. Med. Biol.*, 58(1):R1, 2013.
- Brendel, B., von Teuffenbach, M., Noël, P. B., Pfeiffer, F., and Koehler, T. Penalized maximum likelihood reconstruction for x-ray differential phase-contrast tomography. *Med. Phys.*, 43(1):188–194, 2016.
- Burger, K., Koehler, T., Chabior, M., Allner, S., Marschner, M., Fehring, A., Willner, M., Pfeiffer, F., and Noël, P. Regularized iterative integration combined with non-linear diffusion filtering for phase-contrast x-ray computed tomography. *Opt. Express*, 22(26):32107, 2014.
- Buzug, T. *Computed tomography: From photon statistics to modern cone-beam CT*. Springer-Verlag Berlin Heidelberg, 2008.
- Chabior, M. *Contributions to the characterization of grating-based x-ray phase-contrast imaging*. PhD thesis, Technische Universität München, 2011.

- Chabior, M., Donath, T., David, C., Bunk, O., Schuster, M., Schroer, C., and Pfeiffer, F. Beam hardening effects in grating-based x-ray phase-contrast imaging. *Med. Phys.*, 38(3):1189–1195, 2011.
- Chabior, M., Schuster, M., Schroer, C., and Pfeiffer, F. Grating-based phase-contrast computed tomography of thick samples. *Nucl. Instrum. Methods Phys. Res. A*, 693:138–142, 2012.
- Chen, G.-H., Zambelli, J., Li, K., Bevins, N., and Qi, Z. Scaling law for noise variance and spatial resolution in differential phase contrast computed tomography. *Med. Phys.*, 38(2):584, 2011.
- David, C., Nöhammer, B., Solak, H. H., and Ziegler, E. Differential x-ray phase contrast imaging using a shearing interferometer. *Appl. Phys. Lett.*, 81(17):3287, 2002.
- De Marco, F. *Optimizing data processing for grating-based X-ray phase-contrast computed tomography*. Master thesis, Technical University of Munich, 2015.
- De Marco, F., Marschner, M., Birnbacher, L., Noël, P., Herzen, J., and Pfeiffer, F. Analysis and correction of bias induced by phase stepping jitter in grating-based X-ray phase-contrast imaging. *Opt. Express*, 26(10):12707–12722, 2018.
- De Marco, F., Andrejewski, J., Urban, T., Willer, K., Gromann, L., Koehler, T., Maack, H.-I., Herzen, J., and Pfeiffer, F. X-ray dark-field signal reduction due to hardening of the visibility spectrum. *IEEE Transactions on Medical Imaging*, pages 1–1, 2024.
- De Marco, F. D. *Image reconstruction, pre-clinical studies, and signal formation investigations at a dark-field chest radiography setup*. PhD thesis, Technische Universität München, München, 2021.
- Deák, Z., Grimm, J. M., Treitl, M., Geyer, L. L., Linsenmaier, U., Körner, M., Reiser, M. F., and Wirth, S. Filtered back projection, adaptive statistical iterative reconstruction, and a model-based iterative reconstruction in abdominal CT: an experimental clinical study. *Radiology*, 266(1):197–206, 2013.
- Deng, K., Li, J., and Xie, W. Modeling the moiré fringe visibility of talbot-lau x-ray grating interferometry for single-frame multi-contrast imaging. *Opt. Express*, 28(18):27107–27122, 2020.

- Diemoz, P. C., Coan, P., Zanette, I., Bravin, a., Lang, S., Glaser, C., and Weitkamp, T. A simplified approach for computed tomography with an X-ray grating interferometer. *Opt. Express*, 19(3):1691–8, 2011.
- Faris, G. W. and Byer, R. L. Three-dimensional beam-deflection optical tomography of a supersonic jet. *Appl. Opt.*, 27(24):5202–5212, 1988.
- Feldkamp, I. A., Davis, L. C., and Kress, J. W. Practical cone-beam algorithm. *J. Opt. Soc. Am. A*, 1(6):612–619, 1984.
- Fessler, J. A. *Tomography handbook of medical imaging, volume 2. Medical image processing and analysis: Statistical image reconstruction methods for transmission*. SPIE, Bellingham, 2000.
- Frank, M., Gassert, F. T., Urban, T., Willer, K., Noichl, W., Schick, R., Schultheiss, M., Viermetz, M., Gleich, B., De Marco, F., Herzen, J., Koehler, T., Engel, K. J., Renger, B., Gassert, F. G., Sauter, A., Fingerle, A. A., Haller, B., Makowski, M. R., Pfeiffer, D., and Pfeiffer, F. Dark-field chest x-ray imaging for the assessment of covid-19-pneumonia. *Communications Medicine*, 2(1), 2022.
- Fu, J., Willner, M., Chen, L., Tan, R., Achterhold, K., Bech, M., Herzen, J., Kunka, D., Mohr, J., and Pfeiffer, F. Helical Differential X-ray Phase-Contrast Computed Tomography. *Eur. J. Med. Phys.*, 2014.
- Gassert, F. T. and Pfeiffer, F. X-ray dark-field chest radiography of lymphangiomyomatosis. *Radiology*, 2022.
- Gassert, F. T., Urban, T., Frank, M., Willer, K., Noichl, W., Buchberger, P., Schick, R., Koehler, T., von Berg, J., Fingerle, A. A., Sauter, A. P., Makowski, M. R., Pfeiffer, D., and Pfeiffer, F. X-ray dark-field chest imaging: Qualitative and quantitative results in healthy humans. *Radiology*, page 210963, 2021.
- Gassert, F. T., Frank, M., De Marco, F., Willer, K., Urban, T., Herzen, J., Fingerle, A. A., Sauter, A. P., Makowski, M. R., Kriner, F., Fischer, F., Braun, C., Pfeiffer, F., and Pfeiffer, D. Assessment of inflation in a human cadaveric lung with dark-field chest radiography. *Radiology: Cardiothoracic Imaging*, 4(6), 2022a.
- Gassert, F. T., Urban, T., Pfeiffer, D., and Pfeiffer, F. Dark-field chest radiography of combined pulmonary fibrosis and emphysema. *Radiology: Cardiothoracic Imaging*, 4(4), 2022b.

- Ge, Y., Li, K., Garrett, J., and Chen, G. Grating based x-ray differential phase contrast imaging without mechanical phase stepping. *Opt. Express*, 22(12):19268–19272, 2014.
- Grandl, S., Willner, M., Herzen, J., Sztrókay-Gaul, A., Mayr, D., Auweter, S. D., Hipp, A., Birnbacher, L., Marschner, M., Chabior, M., Reiser, M., Pfeiffer, F., Bamberg, F., Hellerhoff, K., Sztrókay-Gaul, A., Mayr, D., Auweter, S. D., Hipp, A., Birnbacher, L., Marschner, M., Chabior, M., Reiser, M., Pfeiffer, F., Bamberg, F., and Hellerhoff, K. Visualizing typical features of breast fibroadenomas using phase-contrast CT: An ex-vivo study. *PLOS ONE*, 9(5):1–12, 2014.
- Gromann, L. B., de Marco, F., Willer, K., Noël, P. B., Scherer, K., Renger, B., Gleich, B., Achterhold, K., Fingerle, A. A., Muenzel, D., Auweter, S., Hellbach, K., Reiser, M., Bähr, A., Dmochewitz, M., Schröter, T. J., Koch, F. J., Meyer, P., Kunka, D., Mohr, J., Yaroshenko, A., Maack, H.-I., Pralow, T., van der Heijden, H., Proksa, R., Köhler, T., Wieberneit, N., Rindt, K., Rummeny, E. J., Pfeiffer, F., and Herzen, J. In-vivo x-ray dark-field chest radiography of a pig. *Sci. Rep.*, 7(4807), 2017.
- Grünzweig, C., David, C., Bunk, O., Dierolf, M., Frei, G., Kühne, G., Kohlbrecher, J., Schäfer, R., Lejcek, P., Ronnow, H., and Pfeiffer, F. Neutron Decoherence Imaging for Visualizing Bulk Magnetic Domain Structures. *Phys. Rev. Lett.*, 101(2):025504, 2008a.
- Grünzweig, C., David, C., Bunk, O., Dierolf, M., Frei, G., Kühne, G., Schäfer, R., Pofahl, S., Ronnow, H. M. R., and Pfeiffer, F. Bulk magnetic domain structures visualized by neutron dark-field imaging. *Appl. Phys. Lett.*, 93(11):112504, 2008b.
- Grünzweig, C., Kopecek, J., Betz, B., Kaestner, A., Jefimovs, K., Kohlbrecher, J., Gasser, U., Bunk, O., David, C., Lehmann, E., Donath, T., and Pfeiffer, F. Quantification of the neutron dark-field imaging signal in grating interferometry. *Phys. Rev. B - Condens. Matter Mater. Phys.*, 88(12):1–6, 2013.
- Guigay, J. On Fresnel Diffraction by One-dimensional Periodic Objects, with Application to Structure Determination of Phase Objects. *Opt. Acta Int. J. Opt.*, 18(9): 677–682, 1971.
- Hahn, D. *Statistical Iterative Reconstruction for X-ray Phase-Contrast Computed Tomography*. PhD thesis, Technische Universität München, 2014.
- Hahn, D., Thibault, P., Fehring, A., Bech, M., Koehler, T., Pfeiffer, F., and Noël, P. B. Statistical iterative reconstruction algorithm for X-ray phase-contrast CT. *Sci. Rep.*, 5:10452, 2015.

- Hellbach, K., Yaroshenko, A., Meinel, F. G., Yildirim, A. O., Conlon, T. M., Bech, M., Mueller, M., Velroyen, A., Notohamiprodjo, M., Bamberg, F., Auweter, S., Reiser, M., Eickelberg, O., and Pfeiffer, F. In Vivo Dark-Field Radiography for Early Diagnosis and Staging of Pulmonary Emphysema. *Invest Radiol*, 50(7):1–6, 2015.
- Hellerhoff, K., Birnbacher, L., Sztrókay-Gaul, A., Grandl, S., Auweter, S., Willner, M., Marschner, M., Mayr, D., Reiser, M. F., Pfeiffer, F., and Herzen, J. Assessment of intraductal carcinoma in situ (dcis) using grating-based x-ray phase-contrast ct at conventional x-ray sources: An experimental ex-vivo study. *PLOS ONE*, 14(1): e0210291, 2019.
- Herzen, J., Karampinos, D. C., Foehr, P., Birnbacher, L., Viermetz, M., Burgkart, R., Baum, T., Lohoefer, F., Wildgruber, M., Schilling, F., Willner, M., Marschner, M., Noël, P. B., Rummeny, E. J., Pfeiffer, F., and Jungmann, P. M. 3d grating-based x-ray phase-contrast computed tomography for high-resolution quantitative assessment of cartilage: An experimental feasibility study with 3t mri, 7t mri and biomechanical correlation. *PLOS ONE*, 14(2):e0212106, 2019.
- Hetterich, H., Willner, M., Fill, S., Herzen, J., Bamberg, F., Hipp, A., Schüller, U., Adam-Neumair, S., Wirth, S., Reiser, M., Pfeiffer, F., and Saam, T. Phase-Contrast CT: Qualitative and Quantitative Evaluation of Atherosclerotic Carotid Artery Plaque. *Radiology*, 271(3):131554, 2014.
- Hetterich, H., Willner, M., Habbel, C., Herzen, J., Hoffmann, V. S., Fill, S., Hipp, A., Marschner, M., Schüller, U., Auweter, S., Massberg, S., Reiser, M. F., Pfeiffer, F., Saam, T., and Bamberg, F. X-ray Phase-Contrast Computed Tomography of Human Coronary Arteries. *Invest. Radiol.*, 00(00):1, 2015.
- Hetterich, H., Webber, N., Willner, M., Herzen, J., Birnbacher, L., Hipp, A., Marschner, M., Auweter, S. D., Habbel, C., Schüller, U., et al. Aha classification of coronary and carotid atherosclerotic plaques by grating-based phase-contrast computed tomography. *European radiology*, 26:3223–3233, 2016.
- Hetterich, H., Webber, N., Willner, M., Herzen, J., Birnbacher, L., Auweter, S., Schüller, U., Bamberg, F., Notohamiprodjo, S., Bartsch, H., Wolf, J., Marschner, M., Pfeiffer, F., Reiser, M., and Saam, T. Dark-field imaging in coronary atherosclerosis. *European Journal of Radiology*, 94:38–45, 2017.
- H.F. Talbot Esq. F.R.S. LXXVI. Facts relating to optical science. No. IV. *The London*,

- Edinburgh, and Dublin Philosophical Magazine and Journal of Science*, 9(56):401–407, 1836.
- Hilger, A., Kardjilov, N., Kandemir, T., Manke, I., Banhart, J., Penumadu, D., Manescu, A., and Strobl, M. Revealing microstructural inhomogeneities with dark-field neutron imaging. *J. Appl. Phys.*, 107(3), 2010.
- Hipp, A. *Highly sensitive grating interferometry using a polychromatic X-ray-source*. Diploma thesis, Technische Universität München, 2013.
- Hipp, A., Willner, M., Herzen, J., Auweter, S. D., Chabior, M., Meiser, J., Achterhold, K., Mohr, J., and Pfeiffer, F. Energy-resolved visibility analysis of grating interferometers operated at polychromatic X-ray sources. *Opt. Express*, 22(25):30394, 2014.
- Huber, P., Wiley, J., and InterScience, W. *Robust statistics*. Wiley New York, 1981.
- Jensen, T. H., Bech, M., Bunk, O., Donath, T., David, C., Feidenhans'l, R., and Pfeiffer, F. Directional x-ray dark-field imaging. *Phys. Med. Biol.*, 55(12):3317–3323, 2010a.
- Jensen, T. H., Bech, M., Zanette, I., Weitkamp, T., David, C., Deyhle, H., Rutishauser, S., Reznikova, E., Mohr, J., Feidenhans'l, R., and Pfeiffer, F. Directional x-ray dark-field imaging of strongly ordered systems. *Phys. Rev. B*, 82(21):214103, 2010b.
- Ji, X., Ge, Y., Zhang, R., Li, K., and Chen, G.-H. Studies of signal estimation bias in grating-based x-ray multicontrast imaging. *Medical physics*, 44(6):2453–2465, 2017.
- Kak, A. C. and Slaney, M. *Principles of Computerized Tomographic Imaging (Classics in Applied Mathematics)*. Society for Industrial and Applied Mathematics, 2001. ISBN 9780898714944.
- Kalender, W. Technical foundations of spiral CT. *Semin. Ultrasound. CT. MR*, 15(2):81–89, 1994.
- Klein, O. and Nishina, Y. Über die streuung von strahlung durch freie elektronen nach der neuen relativistischen quantendynamik von dirac. *Zeitschrift für Physik*, 52:853–868, 1929.
- Koehler, T., Brendel, B., and Roessl, E. Iterative reconstruction for differential phase contrast imaging using spherically symmetric basis functions. *Med. Phys.*, 38(8):4542, 2011a.

- Koehler, T., Juergen Engel, K., and Roessl, E. Noise properties of grating-based x-ray phase contrast computed tomography. *Med. Phys.*, 38(S1):S106, 2011b.
- Koehler, T., Daerr, H., Martens, G., Kuhn, N., Löscher, S., van Stevendaal, U., and Roessl, E. Slit-scanning differential x-ray phase-contrast mammography: Proof-of-concept experimental studies. *Med. Phys.*, 42(4):1959–1965, 2015.
- Koenig, T., Zuber, M., Trimborn, B., Farago, T., Meyer, P., Kunka, D., Albrecht, F., Kreuer, S., Volk, T., Fiederle, M., and Baumbach, T. On the origin and nature of the grating interferometric dark-field contrast obtained with low-brilliance x-ray sources. *Phys. Med. Biol.*, 61(9):3427–42, 2016.
- Kottler, C., Pfeiffer, F., Bunk, O., Grünzweig, C., Bruder, J., Kaufmann, R., Tlustos, L., Walt, H., Briod, I., Weitkamp, T., and David, C. Phase contrast X-ray imaging of large samples using an incoherent laboratory source. *Phys. Status Solidi*, 204(8): 2728–2733, 2007.
- Li, K., Bevins, N., Zambelli, J., and Chen, G.-H. Fundamental relationship between the noise properties of grating-based differential phase contrast CT and absorption CT: Theoretical framework using a cascaded system model and experimental validation. *Med. Phys.*, 40(2):021908, 2013.
- Li, P., Zhang, K., Bao, Y., Ren, Y., Ju, Z., Wang, Y., He, Q., Zhu, Z., Huang, W., Yuan, Q., and Zhu, P. Angular signal radiography. *Opt. Express*, 24(6):5829–5845, 2016.
- Lindsey, W. Error probabilities for Rician fading multichannel reception of binary and n-ary signals. *IEEE Trans. Inf. Theory*, 10(4):339–350, 1964.
- Lynch, S. K., Pai, V., Auxier, J., Stein, A. F., Bennett, E. E., Kemble, C. K., Xiao, X., Lee, W.-K., Morgan, N. Y., and Wen, H. H. Interpretation of dark-field contrast and particle-size selectivity in grating interferometers. *Appl. Opt.*, 50(22):4310–4319, 2011.
- Malecki, A., Potdevin, G., Biernath, T., Eggl, E., Willer, K., Lasser, T., Maisenbacher, J., Gibmeier, J., Wanner, A., and Pfeiffer, F. X-ray tensor tomography. *EPL*, 105(3):38002, 2014.
- Marschner, M. *Data processing in grating-based X-ray phase-contrast computed tomography: workflow automation and noise studies*. Diplomarbeit, Technische Universität München, 2013.

- Marschner, M., Birnbacher, L., Mechlem, K., Noichl, W., Fehringer, A., Willner, M., Scherer, K., Herzen, J., Noël, P. B., and Pfeiffer, F. Two-shot X-ray dark-field imaging. *Opt. Express*, 24(23):27032, 2016a.
- Marschner, M., Willner, M., Potdevin, G., Fehringer, A., Noël, P. B., Pfeiffer, F., and Herzen, J. Helical X-ray phase-contrast computed tomography without phase stepping. *Sci. Rep.*, 6:23953, 2016b.
- Marschner, M., Birnbacher, L., Willner, M., Chabior, M., Herzen, J., Noël, P. B., and Pfeiffer, F. Revising the lower statistical limit of X-ray grating-based phase-contrast computed tomography. *PLOS ONE*, 12(9):e0184217, 2017.
- Mechlem, K. *Advanced Statistical Iterative Reconstruction for X-ray Computed Tomography*. Master thesis, Technical University of Munich, 2015.
- Mechlem, K., Sellerer, T., Viermetz, M., Herzen, J., and Pfeiffer, F. Spectral differential phase contrast x-ray radiography. *IEEE Transactions on Medical Imaging*, 39(3):578–587, 2020.
- Miao, H., Chen, L., Bennett, E. E., Adamo, N. M., Gomella, A. a., DeLuca, A. M., Patel, A., Morgan, N. Y., and Wen, H. Motionless phase stepping in X-ray phase contrast imaging with a compact source. *Proc. Natl. Acad. Sci. U. S. A.*, 110:19268–72, 2013.
- Mohajerani, P., Hipp, A., Willner, M., Marschner, M., Trajkovic-arsic, M., Ma, X., Burton, N. C., Klemm, U., Radrich, K., Ermolayev, V., Tzoumas, S., Siveke, J. T., Bech, M., Pfeiffer, F., and Ntziachristos, V. FMT-PCCT : Hybrid Fluorescence Molecular Imaging of Mouse Models. *IEEE Trans. Med. Imaging*, 33(7):1434–1446, 2014.
- Mohr, J., Grund, T., Kunka, D., Kenntner, J., Leuthold, J., Meiser, J., Schulz, J., and Walter, M. High aspect ratio gratings for x-ray phase contrast imaging. In *AIP Conference Proceedings*, volume 1466, pages 41–50. American Institute of Physics, 2012.
- Momose, A. Phase-sensitive imaging and phase tomography using X-ray interferometers. *Opt. Express*, 11(19):2303–14, 2003.
- Momose, A. Recent Advances in X-ray Phase Imaging. *Jpn. J. Appl. Phys.*, 44(9A):6355–6367, 2005.

- Momose, A., Kawamoto, S., Koyama, I., Hamaishi, Y., Takai, K., and Suzuki, Y. Demonstration of X-Ray Talbot Interferometry. *Jpn. J. Appl. Phys.*, 42(Part 2, No. 7B):L866–L868, 2003.
- Momose, A., Yashiro, W., Maikusa, H., and Takeda, Y. High-speed X-ray phase imaging and X-ray phase tomography with Talbot interferometer and white synchrotron radiation. *Opt. Express*, 17(15):156–160, 2009.
- Notohamiprodjo, S., Webber, N., Birnbacher, L., Willner, M., Viermetz, M., Herzen, J., Marschner, M., Mayr, D., Bartsch, H., Saam, T., Auweter, S., Pfeiffer, F., Reiser, M. F., and Hetterich, H. Qualitative and quantitative evaluation of structural myocardial alterations by grating-based phase-contrast computed tomography. *Investigative Radiology*, 53(1):26–34, 2018.
- Noël, P. B., Fingerle, A. A., Renger, B., Münzel, D., Rummeny, E. J., and Dobritz, M. Initial Performance Characterization of a Clinical Noise-Suppressing Reconstruction Algorithm for MDCT. *Am. J. Roentgenol.*, 197(6):1404–1409, 2011.
- Noël, P. B., Herzen, J., Fingerle, A. a., Willner, M., Stockmar, M. K., Hahn, D., Settles, M., Drecoll, E., Zanette, I., Weitkamp, T., Rummeny, E. J., and Pfeiffer, F. Evaluation of the potential of phase-contrast computed tomography for improved visualization of cancerous human liver tissue. *Z. Med. Phys.*, 23(3):204–11, 2013a.
- Noël, P. B., Renger, B., Fiebich, M., Münzel, D., Fingerle, A. A., Rummeny, E. J., and Dobritz, M. Does iterative reconstruction lower CT radiation dose: Evaluation of 15,000 examinations. *PLOS ONE*, 8(11):1–7, 2013b.
- Olivo, A. and Speller, R. A coded-aperture technique allowing x-ray phase contrast imaging with conventional sources. *Appl. Phys. Lett.*, 91(7):074106, 2007.
- Paganin, D. M. *Coherent X-ray optics*. Oxford Science Publications, 2006.
- Pelliccia, D., Rigon, L., Arfelli, F., Menk, R.-H., Bukreeva, I., and Cedola, A. A three-image algorithm for hard x-ray grating interferometry. *Opt. Express*, 21(16):19401–11, 2013.
- Pfeiffer, F., Bunk, O., Schulze-Briese, C., Diaz, a., Weitkamp, T., David, C., van der Veen, J., Vartanyants, I., and Robinson, I. Shearing Interferometer for Quantifying the Coherence of Hard X-Ray Beams. *Phys. Rev. Lett.*, 94(16):164801, 2005.
- Pfeiffer, F., Grünzweig, C., Bunk, O., Frei, G., Lehmann, E., and David, C. Neutron Phase Imaging and Tomography. *Phys. Rev. Lett.*, 96(21):215505, 2006a.

- Pfeiffer, F., Weitkamp, T., Bunk, O., and David, C. Phase retrieval and differential phase-contrast imaging with low-brilliance X-ray sources. *Nat. Phys.*, 2(4):258–261, 2006b.
- Pfeiffer, F., Weitkamp, T., and David, C. X-ray phase contrast imaging using a grating interferometer. *Europhys. News*, 37(5):13–15, 2006c.
- Pfeiffer, F., Bunk, O., David, C., Bech, M., Le Duc, G., Bravin, A., and Cloetens, P. High-resolution brain tumor visualization using three-dimensional x-ray phase contrast tomography. *Phys. Med. Biol.*, 52(23):6923–30, 2007a.
- Pfeiffer, F., Bunk, O., Kottler, C., and David, C. Tomographic reconstruction of three-dimensional objects from hard X-ray differential phase contrast projection images. *Nucl. Instrum. Methods Phys. Res. A*, 580(2):925–928, 2007b.
- Pfeiffer, F., Kottler, C., Bunk, O., and David, C. Hard X-Ray Phase Tomography with Low-Brilliance Sources. *Phys. Rev. Lett.*, 98(10):108105, 2007c.
- Pfeiffer, F., Bech, M., Bunk, O., Kraft, P., Eikenberry, E. F., Brönnimann, C., Grünzweig, C., and David, C. Hard-X-ray dark-field imaging using a grating interferometer. *Nat. Mater.*, 7(2):134–137, 2008a.
- Pfeiffer, F., David, C., Bunk, O., Donath, T., Bech, M., Le Duc, G., Bravin, A., and Cloetens, P. Region-of-Interest Tomography for Grating-Based X-Ray Differential Phase-Contrast Imaging. *Phys. Rev. Lett.*, 101(16):168101, 2008b.
- Pfeiffer, F., Herzen, J., Willner, M., Chabior, M., Auweter, S., Reiser, M., and Bamberg, F. Grating-based X-ray phase contrast for biomedical imaging applications. *Z. Med. Phys.*, 23(3):176–85, 2013.
- Prade, F., Yaroshenko, A., Herzen, J., and Pfeiffer, F. Short-range order in mesoscale systems probed by X-ray grating interferometry. *EPL*, 112(6):68002, 2015.
- Press, W. H., Teukolsky, S. A., Vetterling, W. T., and Flannery, B. P. *Numerical recipes 3rd edition: The art of scientific computing*. Cambridge University Press, New York, NY, 3rd edition, 2007.
- Qi, Z. and Chen, G.-H. Direct fan-beam reconstruction algorithm via filtered backprojection for differential phase-contrast computed tomography. *X-Ray Opt. Instrum.*, 2008:835172, 2008.

- Qi, Z., Thériault-Lauzier, P., Bevins, N., Zambelli, J., Li, K., and Chen, G.-H. Helical x-ray differential phase contrast computed tomography. *Proc. SPIE*, 7961:79611Q, 2011.
- Raupach, R. and Flohr, T. G. Analytical evaluation of the signal and noise propagation in x-ray differential phase-contrast computed tomography. *Phys. Med. Biol.*, 56(7): 2219–44, 2011.
- Revol, V., Kottler, C., Kaufmann, R., Straumann, U., and Urban, C. Noise analysis of grating-based x-ray differential phase contrast imaging. *Rev. Sci. Instrum.*, 81(7):073709, 2010.
- Revol, V., Jerjen, I., Kottler, C., Schütz, P., Kaufmann, R., Lüthi, T., Sennhauser, U., Straumann, U., and Urban, C. Sub-pixel porosity revealed by x-ray scatter dark field imaging. *J. Appl. Phys.*, 110(4):44912, 2011a.
- Revol, V., Kottler, C., Kaufmann, R., Jerjen, I., Lüthi, T., Cardot, F., Niedermann, P., Straumann, U., Sennhauser, U., and Urban, C. X-ray interferometer with bent gratings: Towards larger fields of view. *Nucl. Instrum. Methods Phys. Res. A*, 648: 302–305, 2011b.
- Rice, S. O. Mathematical analysis of random noise. *Bell Syst. Tech. J.*, 23(3):282–332, 1944.
- Rice, S. O. Mathematical analysis of random noise. *Bell Syst. Tech. Journal.*, 24(1): 46–156, 1945.
- Richter, V., Willner, M. S., Henningsen, J., Birnbacher, L., Marschner, M., Herzen, J., Kimm, M. A., Noël, P. B., Rummeny, E. J., Pfeiffer, F., and Fingerle, A. A. Ex vivo characterization of pathologic fluids with quantitative phase-contrast computed tomography. *European Journal of Radiology*, 86:99–104, 2017.
- Rigon, L., Besch, H.-J., Arfelli, F., Menk, R.-H., Heitner, G., and Plathow-Besch, H. A new DEI algorithm capable of investigating sub-pixel structures. *J. Phys. D. Appl. Phys.*, 36(10A):A107–A112, 2003.
- Ritter, A., Anton, G., and Weber, T. Simultaneous maximum-likelihood reconstruction of absorption coefficient, refractive index and dark-field scattering coefficient in x-ray talbot-lau tomography. *PLOS ONE*, 11(10):1–15, 2016.
- Roessl, E., Daerr, H., Koehler, T., Martens, G., and van Stevendaal, U. Clinical boundary conditions for grating-based differential phase-contrast mammography. *PPhil. Trans. R. Soc.*, 372(2010), 2014.

- Röntgen, W. C. On a new kind of rays. *Science*, 3(59):227–231, 1896.
- Saleh, B. E. A. and Teich, M. C. *Fundamentals of photonics*. Wiley, Hoboken, NJ, 2nd edition, 2007.
- Scherer, K. *Grating-Based X-Ray Phase-Contrast Mammography*. PhD thesis, Technische Universität München, 2015.
- Scherer, K., Yaroshenko, A., Bölükbas, D. A., Gromann, L. B., Hellbach, K., Meinel, F. G., Braunagel, M., Berg, J. v., Eickelberg, O., Reiser, M. F., Pfeiffer, F., Meiners, S., and Herzen, J. X-ray dark-field radiography - in-vivo diagnosis of lung cancer in mice. *Scientific Reports*, 7(1), 2017.
- Schuhbaeck, A., Achenbach, S., Layritz, C., Eisentopf, J., Hecker, F., Pflederer, T., Gauss, S., Rixe, J., Kalender, W., Daniel, W. G., Lell, M., and Ropers, D. Image quality of ultra-low radiation exposure coronary CT angiography with an effective dose  $<0.1$  mSv using high-pitch spiral acquisition and raw data-based iterative reconstruction. *Eur. Radiol.*, 23(3):597–606, 2013.
- Sijbers, J., den Dekker, A. J., Raman, E., and Van Dyck, D. Parameter estimation from magnitude MR images. *Int. J. Imaging Syst. Technol.*, 10(2):109–114, 1999.
- Strobl, M. General solution for quantitative dark-field contrast imaging with grating interferometers. *Sci. Rep.*, 4:7243, 2014.
- Strobl, M., Grünzweig, C., Hilger, A., Manke, I., Kardjilov, N., David, C., and Pfeiffer, F. Neutron Dark-Field Tomography. *Phys. Rev. Lett.*, 101(12):123902, 2008.
- Suleski, T. J. Generation of Lohmann images from binary-phase Talbot array illuminators. *Appl. Opt.*, 36(20):4686, 1997.
- Sun, Y., Cong, W., Xi, Y., Wang, G., and Pang, S. Talbot interferometry with curved quasi-periodic gratings: towards large field of view X-ray phase-contrast imaging. *Opt. Express*, 23(20):26576–85, 2015.
- Tapfer, A., Bech, M., Velroyen, A., Meiser, J., Mohr, J., Walter, M., Schulz, J., Pauwels, B., Bruyndonckx, P., Liu, X., Sasov, A., and Pfeiffer, F. Experimental results from a preclinical X-ray phase-contrast CT scanner. *Proc. Natl. Acad. Sci. U. S. A.*, 109(39):15691–6, 2012.
- Tapfer, A., Braren, R., Bech, M., Willner, M., Zanette, I., Weitkamp, T., Trajkovic-Arsic, M., Siveke, J. T., Settles, M., Aichler, M., Walch, A., and Pfeiffer, F. X-ray

- phase-contrast CT of a pancreatic ductal adenocarcinoma mouse model. *PLOS ONE*, 8(3):e58439, 2013.
- Teuffenbach, M. v., Koehler, T., Fehringer, A., Viermetz, M., Brendel, B., Herzen, J., Proksa, R., Rummeny, E. J., Pfeiffer, F., and Noël, P. B. Grating-based phase-contrast and dark-field computed tomography: A single-shot method. *Sci. Rep.*, 7(7476), 2017.
- Thüring, T., Modregger, P., Pinzer, B. R., Wang, Z., Rutishauser, S., David, C., Grund, T., Kenntner, J., and Stampanoni, M. Towards X-ray differential phase contrast imaging on a compact setup. In *SPIE Med. Imaging*, page 79611G. International Society for Optics and Photonics, 2011.
- Urban, T., Gassert, F. T., Frank, M., Willer, K., Noichl, W., Buchberger, P., Schick, R. C., Koehler, T., Bodden, J. H., Fingerle, A. A., Sauter, A. P., Makowski, M. R., Pfeiffer, F., and Pfeiffer, D. Qualitative and quantitative assessment of emphysema using dark-field chest radiography. *Radiology*, 2022.
- van Gogh, S., Rawlik, M., Pereira, A., Spindler, S., Mukherjee, S., Zdora, M.-C., Stauber, M., Alaifari, R., Varga, Z., and Stampanoni, M. Towards clinical-dose grating interferometry breast ct with fused intensity-based iterative reconstruction. *Opt. Express*, 31(5):9052–9071, 2023.
- van Stevendaal, U., Wang, Z., Köhler, T., Martens, G., Stampanoni, M., and Roessl, E. Reconstruction method incorporating the object-position dependence of visibility loss in dark-field imaging. *Proc. SPIE*, 8668:86680Z, 2013.
- Velroyen, A. *X-ray Phase-Contrast and Dark-Field Imaging of Small Animals: Contrast Enhancement and in vivo Imaging*. PhD thesis, Technische Universität München, 2015.
- Velroyen, A., Yaroshenko, A., Hahn, D., Fehringer, A., Tapfer, A., Müller, M., Noël, P., Pauwels, B., Sasov, A., Yildirim, A., Eickelberg, O., Hellbach, K., Auweter, S., Meinel, F., Reiser, M., Bech, M., and Pfeiffer, F. Grating-based X-ray Dark-field Computed Tomography of Living Mice. *EBioMedicine*, 2015.
- Viermetz, M., Gustschin, N., Schmid, C., Haeusele, J., von Teuffenbach, M., Meyer, P., Bergner, F., Lasser, T., Proksa, R., Koehler, T., and Pfeiffer, F. Dark-field computed tomography reaches the human scale. *Proceedings of the National Academy of Sciences*, 119(8):e2118799119, 2022.

- Viermetz, M., Gustschin, N., Schmid, C., Haeusele, J., Gleich, B., Renger, B., Koehler, T., and Pfeiffer, F. Initial characterization of dark-field ct on a clinical gantry. *IEEE Transactions on Medical Imaging*, 42(4):1035–1045, 2023.
- Wang, Z. and Han, B. Advanced iterative algorithm for phase extraction of randomly phase-shifted interferograms. *Opt. Lett.*, 29(14):1671–1673, 2004.
- Wang, Z., Gao, K., and Wang, D. Phase retrieval with the reverse projection method in the presence of object’s scattering. *Radiat. Phys. Chem.*, 137:33–36, 2015.
- Wang, Z.-L., Gao, K., Chen, J., Ge, X., Zhu, P.-P., Tian, Y.-C., and Wu, Z.-Y. A new method for information retrieval in two-dimensional grating-based X-ray phase contrast imaging. *Chinese Phys. B*, 21(11):118703, 2012.
- Wang, Z. T., Kang, K. J., Huang, Z. F., and Chen, Z. Q. Quantitative grating-based x-ray dark-field computed tomography. *Appl. Phys. Lett.*, 95(9):10–13, 2009.
- Weber, T., Bartl, P., Bayer, F., Durst, J., Haas, W., Michel, T., Ritter, A., and Anton, G. Noise in x-ray grating-based phase-contrast imaging. *Med. Phys.*, 38(2011):4133–4140, 2011.
- Weitkamp, T., Diaz, A., David, C., Pfeiffer, F., Stampanoni, M., Cloetens, P., and Ziegler, E. X-ray phase imaging with a grating interferometer. *Opt. Express*, 13(16):6296–304, 2005.
- Weitkamp, T., David, C., Kottler, C., Bunk, O., and Pfeiffer, F. Tomography with grating interferometers at low-brilliance sources. *Proc. SPIE*, 6318:63180S, 2006.
- Wen, H., Bennett, E. E., Hegedus, M. M., and Rapacchi, S. Fourier X-ray scattering radiography yields bone structural information. *Radiology*, 251(3):910–8, 2009.
- Willer, K., Fingerle, A. A., Gromann, L. B., De Marco, F., Herzen, J., Achterhold, K., Gleich, B., Muenzel, D., Scherer, K., Renz, M., Renger, B., Kopp, F., Kriner, F., Fischer, F., Braun, C., Auweter, S., Hellbach, K., Reiser, M. F., Schroeter, T., Mohr, J., Yaroshenko, A., Maack, H.-I., Pralow, T., van der Heijden, H., Proksa, R., Koehler, T., Wieberneit, N., Rindt, K., Rummeny, E. J., Pfeiffer, F., and Noël, P. B. X-ray dark-field imaging of the human lung—a feasibility study on a deceased body. *PLOS ONE*, 13(9):e0204565, 2018.
- Willer, K., Fingerle, A. A., Noichl, W., De Marco, F., Frank, M., Urban, T., Schick, R., Gustschin, A., Gleich, B., Herzen, J., Koehler, T., Yaroshenko, A., Pralow, T., Zimmermann, G. S., Renger, B., Sauter, A. P., Pfeiffer, D., Makowski, M. R.,

- Rummeny, E. J., Grenier, P. A., and Pfeiffer, F. X-ray dark-field chest imaging for detection and quantification of emphysema in patients with chronic obstructive pulmonary disease: a diagnostic accuracy study. *The Lancet Digital Health*, 3(11): e733–e744, 2021.
- Willmott, P. *An Introduction to Synchrotron Radiation: Techniques and Applications*. John Wiley & Sons, 2011.
- Willner, M. *Development of a system for X-ray phase contrast imaging*. Diploma thesis, Technische Universität München, 2011.
- Willner, M. *Quantitative phase-contrast computed tomography for biomedical X-ray imaging at conventional sources*. PhD thesis, Technische Universität München, 2016.
- Willner, M., Herzen, J., Grandl, S., Auweter, S., Mayr, D., Hipp, A., Chabior, M., Sarapata, A., Achterhold, K., Zanette, I., Weitkamp, T., Sztrókay, A., Hellerhoff, K., Reiser, M., and Pfeiffer, F. Quantitative breast tissue characterization using grating-based x-ray phase-contrast imaging. *Phys. Med. Biol.*, 59(7):1557–71, 2014.
- Willner, M., Fior, G., Marschner, M., Birnbacher, L., Schock, J., Braun, C., Fingerle, A. a., Noël, P. B., Rummeny, E. J., Pfeiffer, F., and Herzen, J. Phase-Contrast Hounsfield Units of Fixated and Non-Fixated Soft-Tissue Samples. *PLOS ONE*, 10(8):e0137016, 2015.
- Winthrop, J. T. and Worthington, C. R. Theory of Fresnel images I. Plane periodic objects in monochromatic light. *J. Opt. Soc. Am.*, 55(4):373, 1965.
- Wu, Z., Gao, K., Wang, Z., Ge, X., Chen, J., Wang, D., Pan, Z., Zhang, K., Zhu, P., and Wu, Z. A new method to retrieve phase information for equiangular fan beam differential phase contrast computed tomography. *Med. Phys.*, 40(3):031911, 2013.
- Wu, Z., Wang, Z., Gao, K., Wang, D., Wang, S., Chen, J., Chen, H., Zhang, K., Zhu, P., and Wu, Z. Signal-to-noise ratio analysis of X-ray grating interferometry with the reverse projection extraction method. *J. Electron Spectros. Relat. Phenomena*, 196:75–79, 2014.
- Wu, Z., Gao, K., Chen, J., Wang, D., Wang, S., Chen, H., Bao, Y., Shao, Q., Zhang, K., Zhu, P., Wu, Z., Wu, Z., Gao, K., Chen, J., Wang, D., Wang, S., Chen, H., Bao, Y., and Zhang, K. High sensitivity phase retrieval method in grating-based x-ray phase contrast imaging. *Med. Phys.*, 42(2):741–49, 2015.

- Xu, J., Wang, Z., van Gogh, S., Rawlik, M., Spindler, S., and Stampanoni, M. Intensity-based iterative reconstruction for helical grating interferometry breast ct with static grating configuration. *Opt. Express*, 30(8):13847–13863, 2022.
- Xu, Q., Sidky, E. Y., Pan, X., Stampanoni, M., Modregger, P., and Anastasio, M. a. Investigation of discrete imaging models and iterative image reconstruction in differential X-ray phase-contrast tomography. *Opt. Express*, 20(10):10724, 2012.
- Yaroshenko, A., Bech, M., Potdevin, G., Malecki, A., Biernath, T., Wolf, J., Tapfer, A., Schüttler, M., Meiser, J., Kunka, D., Amberger, M., Mohr, J., and Pfeiffer, F. Non-binary phase gratings for x-ray imaging with a compact Talbot interferometer. *Opt. Express*, 22(1):547, 2014.
- Yashiro, W., Terui, Y., Kawabata, K., and Momose, A. On the origin of visibility contrast in x-ray Talbot interferometry. *Opt. Express*, 18(16):16890–16901, 2010.
- Zanette, I., Weitkamp, T., Lang, S., Langer, M., Mohr, J., David, C., and Baruchel, J. Quantitative phase and absorption tomography with an X-ray grating interferometer and synchrotron radiation. *Phys. Status Solidi*, 208(11):2526–2532, 2011.
- Zanette, I., Bech, M., Rack, A., Le Duc, G., Tafforeau, P., David, C., Mohr, J., Pfeiffer, F., and Weitkamp, T. Trimodal low-dose X-ray tomography. *Proc. Natl. Acad. Sci. U. S. A.*, 109(26):10199–204, 2012.
- Zhang, H., Zhang, S., Hu, D., Zeng, D., Bian, Z., Lu, L., Ma, J., and Huang, J. Threshold choices of Huber regularization using global- and local-edge-detecting operators for X-ray computed tomographic reconstruction. *2013 35th Annual International Conference of the IEEE Engineering in Medicine and Biology Society (EMBC)*, pages 2352–2355, 2013.
- Zhu, P., Zhang, K., Wang, Z., Liu, Y., Liu, X., Wu, Z., McDonald, S. A., Marone, F., and Stampanoni, M. Low-dose, simple, and fast grating-based X-ray phase-contrast imaging. *Proc. Natl. Acad. Sci. U. S. A.*, 107(31):13576–13581, 2010.
- Zimmermann, G. S., Fingerle, A. A., Renger, B., Laugwitz, K.-L., Hautmann, H., Sauter, A., Meurer, F., Gassert, F. T., Bodden, J., Müller-Leisse, C., Renz, M., Rummeny, E. J., Makowski, M. R., Willer, K., Noichl, W., De Marco, F., Frank, M., Urban, T., Schick, R. C., Herzen, J., Koehler, T., Haller, B., Pfeiffer, D., and Pfeiffer, F. Dark-field chest x-ray imaging: first experience in patients with alpha1-antitrypsin deficiency. *European Radiology Experimental*, 6(1), 2022.



# List of publications and scientific presentations

## First-authored publications

Marschner, M., Willner, M., Potdevin, G., Fehringer, A., Noël, P. B., Pfeiffer, F., and Herzen, J. Helical X-ray phase-contrast computed tomography without phase stepping. *Sci. Rep.* 6, 23953, 2016.

Marschner, M., Birnbacher, L., Mechlem, K., Noichl, W., Fehringer, A., Willner, M., Scherer, K., Herzen, J., Noël, P. B., and Pfeiffer, F. Two-shot X-ray dark-field imaging. *Opt. Express* 24(23), 27032, 2016.

Marschner, M., Birnbacher, L., Willner, M., Chabior, M., Herzen, J., Noël, P. B., and Pfeiffer, F. Revising the lower statistical limit of X-ray grating-based phase-contrast computed tomography. *PLoS One* 12(9), e0184217, 2017.

## Co-authored publications

Birnbacher, L., Willner, M., Velroyen, A., Marschner, M., Hipp, A., Meiser, J., Koch, F., Schröter, T., Kunka, D., Mohr, J., Pfeiffer, F., and Herzen, J. Experimental Realisation of High-sensitivity Laboratory X-ray Grating-based Phase-contrast Computed Tomography. *Sci. Rep.*, 6(1), 24022, 2016.

Birnbacher, L., Viermetz, M., Noichl, W., Allner, S., Fehringer, A., Marschner, M., Von Teuffenbach, M., Willner, M., Achterhold, K., Noël, P. B., Koehler, T., Herzen, J., and Pfeiffer, F. Tilted grating phase-contrast computed tomography using statistical iterative reconstruction. *Sci. Rep.*, 8(1), 6608, 2018.

Birnbacher, L., Willner, M., Marschner, M., Pfeiffer, D., Pfeiffer, F., and Herzen, J. Accurate effective atomic number determination with polychromatic grating-based phase-contrast computed tomography. *Opt. Express*, 26(12), 15153, 2018.

Birnbacher L., Braunagel M., Willner M., Marschner, M., De Marco F., Viermetz, M., Auweter, S., Notohamiprodjo, S., Hellbach, K., Notohamiprodjo, M., Staehler, M., Pfeiffer, D., Reiser, M., Pfeiffer, F., and Herzen, J. Quantitative differentiation of minimal-fat angiomyolipomas from renal cell carcinomas using grating-based x-ray

phase-contrast computed tomography: An ex vivo study. *PLoS One* 18(4), e0279323, 2023.

Braunagel, M., Birnbacher, L., Willner, M., Marschner, M., De Marco, F., Viermetz, M., Notohamiprodjo, S., Hellbach, K., Auweter, S., Link, V., Woischke, C., Reiser, M. F., Pfeiffer, F., Notohamiprodjo, M., and Herzen, J. Qualitative and Quantitative Imaging Evaluation of Renal Cell Carcinoma Subtypes with Grating-based X-ray Phase-contrast CT. *Sci. Rep.*, 7(1), 45400, 2017.

Burger, K., Koehler, T., Chabior, M., Allner, S., Marschner, M., Fehringner, A., Willner, M., Pfeiffer, F., and Noël, P. Regularized iterative integration combined with non-linear diffusion filtering for phase-contrast x-ray computed tomography. *Opt. Express*, 22(26), 32107, 2014.

De Marco, F., Marschner, M., Birnbacher, L., Noël, P., Herzen, J., and Pfeiffer, F. Analysis and correction of bias induced by phase stepping jitter in grating-based X-ray phase-contrast imaging. *Opt. Express*, 26(10), 12707, 2018.

De Marco, F., Marschner, M., Birnbacher, L., Viermetz, M., Noël, P., Herzen, J., and Pfeiffer, F. Improving image quality in laboratory x-ray phase-contrast imaging. *Proc. SPIE*, 10132, 2017.

Grandl, S., Willner, M., Herzen, J., Sztrókay-Gaul, A., Mayr, D., Auweter, S. D., Hipp, A., Birnbacher, L., Marschner, M., Chabior, M., Reiser, M., Pfeiffer, F., Bamberg, F., and Hellerhoff, K. Visualizing typical features of breast fibroadenomas using phase-contrast CT: An ex-vivo study. *PLoS One*, 9(5), 1–12, 2014.

Hellerhoff, K., Birnbacher, L., Sztrókay-Gaul, A., Grandl, S., Auweter, S., Willner, M., Marschner, M., Mayr, D., Reiser, M. F., Pfeiffer, F., and Herzen, J. Assessment of intraductal carcinoma in situ (DCIS) using grating-based X-ray phase-contrast CT at conventional X-ray sources: An experimental ex-vivo study. *PLoS One*, 14(1), e0210291, 2019.

Herzen, J., Karampinos, D. C., Foehr, P., Birnbacher, L., Viermetz, M., Burgkart, R., Baum, T., Lohoefer, F., Wildgruber, M., Schilling, F., Willner, M., Marschner, M., Noël, P. B., Rummeny, E. J., Pfeiffer, F., and Jungmann, P. M. 3D grating-based X-ray phase-contrast computed tomography for high-resolution quantitative assessment of cartilage: An experimental feasibility study with 3T MRI, 7T MRI and biomechanical correlation. *PLoS One*, 14(2), 2019.

Hetterich, H., Habbel, C., Willner, M., Herzen, J., Saam, T., Hipp, A., Marschner, M.,

Reiser, M., Pfeiffer, F., and Bamberg, F. Charakterisierung der koronaren Atherosklerose mittels röntgenbasierter Phasenkontrast-Computertomografie. *Fortschr. Röntgenstr.*, 186(S 01), 2014.

Hetterich, H., Willner, M., Habbel, C., Herzen, J., Hoffmann, V. S., Fill, S., Hipp, A., Marschner, M., Schüller, U., Auweter, S., Massberg, S., Reiser, M. F., Pfeiffer, F., Saam, T., and Bamberg, F. X-ray Phase-Contrast Computed Tomography of Human Coronary Arteries. *Investig. Radiol.*, 50(10), 686–694, 2015.

Hetterich, H., Webber, N., Willner, M., Herzen, J., Birnbacher, L., Hipp, A., Marschner, M., Auweter, S. D., Habbel, C., Schüller, U., Bamberg, F., Ertl-Wagner, B., Pfeiffer, F., and Saam, T. AHA classification of coronary and carotid atherosclerotic plaques by grating-based phase-contrast computed tomography. *Eur. Radiol.*, 1–11, 2016.

Hetterich, H., Webber, N., Willner, M., Herzen, J., Birnbacher, L., Auweter, S., Schüller, U., Bamberg, F., Notohamiprodjo, S., Bartsch, H., Wolf, J., Marschner, M., Pfeiffer, F., Reiser, M., and Saam, T. Dark-field imaging in coronary atherosclerosis. *Eur. J. Radiol.*, 94, 38–45, 2017.

Mohajerani, P., Hipp, A., Willner, M., Marschner, M., Trajkovic-Arsic, M., Ma, X., Burton, N. C., Klemm, U., Radrich, K., Ermolayev, V., Tzoumas, S., Siveke, J. T., Bech, M., Pfeiffer, F., and Ntziachristos, V. FMT-PCCT: Hybrid fluorescence molecular tomography - X-ray phase-contrast CT imaging of mouse models. *IEEE Trans. Med. Imaging*, 33(7), 1434–1446, 2014.

Notohamiprodjo, S., Webber, N., Birnbacher, L., Willner, M., Viermetz, M., Herzen, J., Marschner, M., Mayr, D., Bartsch, H., Saam, T., Auweter, S., Pfeiffer, F., Reiser, M. F., and Hetterich, H. Qualitative and Quantitative Evaluation of Structural Myocardial Alterations by Grating-Based Phase-Contrast Computed Tomography. *Investigative Radiology*, 53(1), 2018.

Richter, V., Willner, M. S., Henningsen, J., Birnbacher, L., Marschner, M., Herzen, J., Kimm, M. A., Noël, P. B., Rummeny, E. J., Pfeiffer, F., and Fingerle, A. A. Ex vivo characterization of pathologic fluids with quantitative phase-contrast computed tomography. *Eur. J. Radiol.*, 86, 99–104, 2017.

Ruiz-Yaniz, M., Zanette, I., Sarapata, A., Birnbacher, L., Marschner, M., Chabior, M., Olbinado, M., Pfeiffer, F., and Rack, A. Hard X-ray phase-contrast tomography of non-homogeneous specimens: grating interferometry versus propagation-based imaging. *J. Synchrotron Rad.*, 23(5), 1202–1209, 2016.

Willner, M., Viermetz, M., Marschner, M., Scherer, K., Braun, C., Fingerle, A., Noël, P., Rummeny, E., Pfeiffer, F., and Herzen, J. Quantitative three-dimensional imaging of lipid, protein, and water contents via X-ray phase-contrast tomography. *PLoS One*, 11(3), e0151889, 2016.

Willner, M., Fior, G., Marschner, M., Birnbacher, L., Schock, J., Braun, C., Fingerle, A. a., Noël, P. B., Rummeny, E. J., Pfeiffer, F., and Herzen, J. Phase-Contrast Hounsfield Units of Fixated and Non-Fixated Soft-Tissue Samples. *PLoS One*, 10(8), e0137016, 2015.

## Conference presentations

### Talks

Advanced signal extraction schemes for X-ray grating-based phase-contrast CT, *Frühjahrstagung der Deutschen Physikalischen Gesellschaft (DPG)*, Hamburg, Germany, March 2016.

Enabling low dose scans in X-ray phase-contrast CT, *Third Meeting on X-Ray and Neutron Phase Imaging with Gratings (XNPIG)*, Bethesda, MD, USA, September 2015.

Redefining the lower statistical limit in x-ray phase-contrast computed tomography, *SPIE Medical Imaging*, Orlando, FL, USA, February 2015.

X-ray phase-contrast computed tomography in helical mode without phase stepping, *The Third International Conference on Image Formation in X-ray Computed Tomography (CT Meeting)*, Salt Lake City, UT, USA, June 2014

Statistical Iterative Reconstruction for Phase-Contrast Computed Tomography, *Frühjahrstagung der Deutschen Physikalischen Gesellschaft (DPG)*, Mainz, Germany, March 2014.

Towards Lower Dose – Statistical Iterative Reconstruction for Phase-Contrast Computed Tomography, *XNPIG Workshop and 3rd International Symposium on Biomedical Applications of X-Ray Phase Contrast Imaging*, Garmisch-Partenkirchen, Germany, January 2014.

Influence of image processing on noise, sharpness and quantitiveness in grating-based

phase-contrast imaging, *Frühjahrstagung der Deutschen Physikalischen Gesellschaft (DPG)*, Regensburg, Germany, March 2013.

## Posters

Redefining the lower statistical limit in X-ray phase-contrast CT, *Radiological Society of North America (RNSA) Annual Meeting*, Chicago, IL, USA, November 2015.

Continuous helical X-ray phase-contrast computed tomography without phase-stepping, *4th International Symposium on Biomedical Applications of X-Ray Phase Contrast Imaging (IMXP)*, Garmisch-Partenkirchen, Germany, January 2015.

X-ray phase-contrast computed tomography using a helical scan approach without phase-stepping, *International Conference on X-Ray Microscopy (XRM)*, Melbourne, Australia, October 2014.

X-ray phase-contrast computed tomography in helical mode without phase stepping, *8th Zurich Summer School on Multiscale Biomedical Imaging (ETH Zurich, University of Zurich and University Hospital Zurich)*, Zurich, Switzerland, September 2014 (Best Student Poster Award)



# Acknowledgments

I would like to sincerely thank my supervising professor, Prof. Dr. Franz Pfeiffer, for his always competent and friendly support. He made it possible for me to conduct my doctoral research at this extraordinary chair that combines excellent research, interesting topics in physics and medicine and a very pleasant working atmosphere, while also allowing me to participate in numerous conferences and beamtime sessions.

Many thanks to Prof. Dr. Julia Herzen for your energetic support, countless pieces of advice, and the many legendary moments we shared together with the department team.

Thank you to Dr. Peter Noel for your insights into clinical imaging.

Thank you to Dr. Thomas Köhler for the insights into the industrial side of research and many practical tips.

Many thanks to Marian for your always uncomplicated, quick, and pragmatic help. Thanks to you, not only my diploma thesis but also my doctoral thesis was a success. Thank you also for proofreading this dissertation.

Special thanks to my long-time office partner Lorenz, who was always ready to help with all his knowledge and kind nature, especially concerning measurements. The years we spent at the department, including our travels, beamtimes, and many leisure activities, will always remain fond memories. Many thanks also for proofreading this thesis.

Thank you, Basti, for the always straightforward collaboration, your competent technical input, and the enjoyable time we spent together at the department, including shared travels and leisure activities.

Many thanks to Wolfgang for the extremely helpful proofreading of papers and the dissertation. It was always a pleasure to work with you, and I greatly appreciated your expertise.

Thank you, Max, for many interesting discussions and valuable input, as well as all the fun during the extracurricular activities.

Thanks to Nelly, Klaus, Martin, and Andreas for your invaluable support in the background.

Thank you to Kai, Maite, Andreas, Lorenz H., Korbinian, Fabio, Konsti, Eva, Marco, Regine, Pidassa, Karin, Florian, Christoph, Friedrich, Irene, and everyone else for your support. Whether through technical advice or by contributing to the unique atmosphere of the department, I will always fondly remember our time together.

I am grateful that during the time of my dissertation, some strong friendships have formed, which continue to this day.